REPORT No. 1877/PH

# Deep Inelastic Scattering at Small Values of the Bjorken Variable x

Habilitation thesis

Krzysztof Golec–Biernat

Kraków/Hamburg
2001

To Alina

# Contents

# Chapter 1

# Introduction

In this dissertation we present a description of interactions in deep inelastic scattering (DIS) of electrons and protons at small values of the Bjorken variable $x$. Such processes are currently studied experimentally at the DESY $ep$ collider HERA. DIS experiments established Quantum Chromodynamics (QCD) as the underlying theory of strong interactions. Quarks and gluons, the basic quanta of this theory, account for the revealed point-like structure of the proton down to distances of about $10^{-16}$ cm. The small-$x$ kinematic domain explored at HERA is particularly interesting from the point of view of QCD studies.

The basic feature of QCD interactions is *asymptotic freedom*. At distances much smaller than the typical hadronic size ($\sim 1$ fm) quarks and gluons behave as very weakly interacting free particles (partons). The manifestation of such a behaviour is *scaling* of the proton structure function $F_2$ with logarithmic violation explained by perturbative QCD (pQCD). With the rising distance, the interactions become stronger and eventually quarks and gluons are bound in directly observed hadrons. This phenomenon, called *confinement*, has been extensively studied since the advent of QCD. Despite these efforts, however, the full understanding of confinement is yet to be achieved. In the confinement region pQCD breaks down and new nonperturbative methods are necessary. The lattice formulation of QCD serves as an example.

The QCD studies of DIS at small $x$ ($\ll 1$) are located between the regions of asymptotic freedom and confinement. The physical picture of the proton which emerges from these studies suggests that the proton structure at small $x$ is dominated by dense gluonic systems with a large number of low momentum (wee) gluons. As a result, the proton structure function $F_2$ strongly increases with decreasing $x$. The strong rise, however, cannot go on indefinitely due to interactions between gluons in the dense systems. This effect, called *parton saturation*, tames the strong rise of $F_2$ in agreement with the condition of unitarity of the description. Thus, at small $x$ gluons in the proton form a strongly correlated system of interacting particles. Let us recall that the fixed target DIS experiments, performed for $x \sim 1$, revealed a dilute system of free partons. Thus in DIS at small $x$, a new (*semi-hard*) regime of QCD is studied in which the strong coupling constant is small but the interactions between partons cannot be neglected.

The question whether parton saturation is relevant in the kinematic range of HERA has intrigued physicists since the beginning of this experiment. Due to the large $ep$ center-of-mass energy, the Bjorken variable $x \sim 10^{-5}$ at scales for which pQCD is still applicable. The description which we are going to present strongly suggests the positive answer to this question.

The physical interpretation of DIS at small $x$ is provided in the proton rest frame. In this frame, the virtual photon $\gamma^*$ fluctuates into a quark-antiquark pair long time before the pair interacts with the proton. Thus, the pair formation and its subsequent interaction are clearly separated. In this interpretation, $\gamma^*$ is a linear superposition of partonic components, being the $q\bar{q}$ dipoles characterized by the transverse size $r$ (with respect to the $\gamma^* p$ collision axis) and longitudinal momentum $z$. The dipole–proton interaction does not mix these components, i.e. $r$ and $z$ are good quantum numbers conserved by the interaction. Therefore, DIS at small $x$ can be viewed as the sum over independent $q\bar{q}$ dipole scatterings on the proton target. In this sense, the DIS process is similar to hadron–hadron scattering, with the advantage that the structure of one of the projectiles is completely known.

The dipole–proton interaction depends on the dipole size. For small sizes ($r \ll 1$ fm), pQCD is applicable and the interaction is realized by a single gluon exchange accompanied by an additional gluon radiation. For large sizes ($r \sim 1$ fm), confinement forces are important, changing the interaction to a one resembling hadron–hadron interactions with a weak dependence on energy. This effect cannot be computed in pQCD and has to be modelled, but the onset of the transition between the QCD radiation at small sizes and hadronic interactions for large sizes is within the reach of pQCD means. In the intermediate range of the dipole sizes, multi-gluon exchanges with additional interactions between the gluons are important, leading to the picture of parton saturation.

The detailed QCD description of the above processes has not been achieved yet. We propose a phenomenological approach and postulate a parameterization of the dipole–proton interactions which incorporates the described features. With this parameterization we achieved a very good description of the DIS data at small $x$ (mainly from HERA), including the transition to low $Q^2$ values. The main ingredient of this model is a saturation radius $R_0(x)$, related to the size of a gluon system in the proton. $R_0(x)$ sets the scale for the dipole configurations. In particular, $r \sim R_0$ corresponds to the transition region where saturation effects are important. The saturation radius decreases when $x \to 0$, thus, for small enough $x$, saturation effects can be described by pQCD, making the approach consistent. We find that it happens in the HERA kinematic range since $R_0 \approx 0.2$ fm (which corresponds to the saturation scale $Q_s(x) = 1/R_0(x) \approx 1$ GeV) for $x \sim 10^{-4}$. Parton saturation allows to describe the transition of the $\gamma^* p$ cross section, $\sigma_{\gamma^* p} \sim F_2/Q^2$, to low $Q^2$ values. Namely, if the wavelength of the virtual probe is smaller than the saturation radius, $1/Q \ll R_0$, Bjorken scaling (with logarithmic violation) is found, $\sigma_{\gamma^* p} \sim 1/Q^2$. In the opposite case, when $1/Q \gg R_0$, the virtual probe cannot resolve the gluonic system and $\sigma_{\gamma^* p}$ saturates to a constant value.

A very stringent test of the postulated model of the dipole-proton interactions is provided by diffractive DIS at small $x$. In a first approximation, these

processes can be interpreted as elastic scattering of $q\bar{q}$ dipoles off the proton with the net colourless exchange. As a result, the proton stays intact, losing only a small fraction of its initial momentum. The most striking feature of DIS diffraction, measured at HERA, is a constant ratio ($\sim 10\%$) between the diffractive and total cross sections as a function of $x$ and $Q^2$. The understanding of this feature, as well as the entire process, is a great challenge for QCD.

The parameters of the dipole–proton interactions were determined in the analysis of inclusive DIS. With these parameters a good description of diffractive DIS is also obtained. In particular, the constant ratio $\sigma_{diff}/\sigma_{tot}$ is naturally explained. The key element for the success of this approach is incorporation of parton saturation effects with the intrinsic saturation scale $R_0(x)$. A distinctive feature of DIS diffraction is the suppression of the small size dipole configuration ($r \ll R_0$), making diffractive processes directly sensitive to the range of $r \sim R_0$ in which parton saturation effects dominate. The relative hardness of the saturation scale, $1/R_0 \sim 1$ GeV, suggests that DIS diffraction is a semi-hard rather than soft process as Regge theory (used traditionally in the description of hadron-hadron high energy scattering) would require.

In the following we describe inclusive and diffractive processes in DIS at small $x$ from the unified point of view imposed by the dipole picture presented above in which parton saturation plays the dominant role. An extensive comparison with the current data from HERA is also presented. The dissertation is based on the following original articles (in the chronological order).

I K. Golec–Biernat and J. Kwieciński, *QCD analysis of diffractive DIS at HERA*, Phys. Lett. **B353** (1995) 329, [117].

II K. Golec–Biernat, *Partonic structure of the pomeron*, Acta Phys. Polon. **B27** (1996) 134, [115].

III K. Golec–Biernat and J.P. Phillips, *QCD: Quantum chromodynamic diffraction*, J. Phys. **G22** (1996) 92, [114].

IV K. Golec–Biernat and J. Kwieciński, *Subleading reggeons in deep inelastic diffractive scattering at HERA*, Phys. Rev. **D55** (1997) 3209, [120].

V K. Golec–Biernat, J. Kwieciński and A. Szczurek, *Reggeon and pion contributions in semi–exclusive diffractive processes at HERA*, Phys. Rev. **D56** (1997) 3955, [121].

VI K. Golec–Biernat and M. Wüsthoff, *Saturation effect in deep inelastic scattering at low $Q^2$ and its implication on diffraction*, Phys. Rev. **D59** (1999) 014017, [94].

VII K. Golec–Biernat and M. Wüsthoff, *Saturation in diffractive deep inelastic scattering*, Phys. Rev. **D60** (1999) 114023 [95].

VIII J. Bartels, K. Golec–Biernat and K. Peters, *An estimate of higher twist at small x and low $Q^2$ based upon a saturation model*, Eur. Phys. J. **C17** (2000) 121, [99].

IX A. Staśto, K. Golec-Biernat and J. Kwieciński, *Geometric scaling for the total $\gamma^* p$ cross section in the low $x$ region*, Phys. Rev. Lett., **86** (2001) 596, [98].

X K. Golec–Biernat and M. Wüsthoff, *Diffractive parton distributions from the saturation model*, Eur. Phys. J. **C20** (2001) 313 , [155].

The outline of the presentation is the following. In Chapter 2 we provide basic elements of the QCD description of deep inelastic processes, mainly for pedagogical reason, following the literature on this subject in the past 30 years. A particular attention is paid to the description of DIS at small $x$. From the point of view of Regge theory, used traditionally in the description of high energy hadronic scattering, the small $x$ limit corresponds to Regge limit in which a pomeron exchange with soft dependence on energy dominates. The analysis of this limit in pQCD leads to the concept of a hard pomeron with much stronger dependence on energy. The hard pomeron calls for unitarization corrections. They are realized in terms of parton saturation effects which lead to nonlinear modifications of the standard evolution equations.

In Chapter 3, based on the results from Refs. [VI,VIII,IX], we present a description of inclusive DIS in the dipole picture. In this picture, the parameterization of the dipole–proton interactions incorporates in a phenomenological way both the hard pomeron concept and its unitarization done with the help of the idea of parton saturation [VI]. We determine few parameters of this model from a fit to all available data at small $x$. As a result, a very good description of inclusive DIS data at small $x$ is obtained, including the transition region to small $Q^2$ values. In addition, a new scaling law at small $x$ is predicted and confronted with the data [IX]. We discuss also heavy flavour production and analyze more formal aspect related to the twist expansion in DIS at small $x$ [VIII]. We finish this part by presenting two conceptually different approaches to the description of the transition to small $Q^2$ values in DIS.

In Chapter 4 we describe diffractive DIS following the results obtained in Refs. [I-V,VII,X]. In the first part, these processes are described using Regge theory, modified to allow for a partonic structure of the diffractive system [I-V]. This is necessary in order to account for the measured leading twist character of the diffractive structure function. In the second part, we present an alternative description in which the diffractive system and its interaction with the proton are modelled starting from perturbative QCD [VII]. The dipole–proton cross section found in the inclusive DIS analysis is naturally applied in this approach. In DIS diffraction, the idea of saturation is even more important, allowing for explanation of the most striking experimental fact from HERA of the constant ratio between the diffractive and inclusive cross sections. We discuss in detail various aspects of the description, presenting an extensive comparison with the data The relation between the two approaches to DIS diffraction is discussed in the part on diffractive parton distributions [X]. We point out that many features of these processes which are postulated in the Regge-like approach find an explanation in the pQCD description combined with the idea of saturation.

Conclusions and outlook are presented in Chapter 5. The derivation of some crucial relations for the main stream presentation is moved to Appendices.

# Chapter 2

# Basics

## 2.1 DIS cross section and structure functions

In the electron-proton deep inelastic scattering (DIS), shown schematically in Fig. 2.1, the incoming electron couples to the electroweak current which probes the structure of the proton. In the following we will concentrate on the kinematic range in which electromagnetic part of the current dominates. In such a case a virtual photon is exchanged with virtuality[1]

$$Q^2 \;=\; -q^2 \;=\; -(e-e')^2 > 0\,, \tag{2.1}$$

where $e$ and $e'$ are incoming and scattered electron momenta. $Q^2$ determines the resolution power with which the proton is probed by the photon. The other important quantity is the dimensionless Bjorken variable

$$x = \frac{Q^2}{2p\cdot q} \;=\; \frac{Q^2}{Q^2+W^2}\,, \tag{2.2}$$

where $p$ is the incoming proton momentum and $W^2$ is the square of center-of-mass energy of the virtual photon–proton ($\gamma^* p$) system,

$$W^2 \;\equiv\; (p+q)^2 \;=\; Q^2\left(\frac{1}{x}-1\right)\,. \tag{2.3}$$

In proton's rest frame $2p\cdot q = 2M\nu$, with $\nu = E - E'$ being the energy transfer from the electron to the proton. Both quantities, $x$ and $Q^2$, can be determined by measuring energy $E'$ and scattering angle $\theta'$ of the scattered electron. Other complementary methods involve the final hadronic state $X$. From the conceptual point of view, however, the observation of the scattered electron suffices to reveal the proton structure. The defined kinematic variables, $x$ and $Q^2$, are particularly useful for a physical interpretation of DIS.

The differential cross section for unpolarized $ep$ DIS in one photon exchange approximation reads

$$\frac{d\sigma}{dx\,dQ^2} \;=\; \frac{2\pi\,\alpha_{em}^2}{x^2 s^2 Q^2}\; L^{\mu\nu}\; W_{\mu\nu}\,, \tag{2.4}$$

[1] It is convenient to change the sign of the space–like photon virtuality.

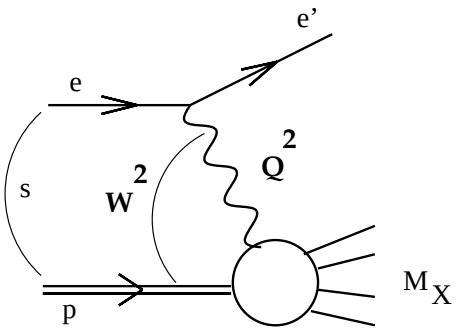


Figure 2.1: *Kinematic invariants in DIS.*

where $\alpha_{em} \approx 1/137$ and $s = (p+e)^2$ is the $ep$ system center-of-mass energy squared. The neglected $W$ and $Z$ boson exchanges are important for $Q^2 \approx M^2_{W,Z}$, corresponding to much larger values of $x$ than those we consider.

$L^{\mu\nu}$ is the leptonic tensor, fully determined from QED coupling of the virtual photon to the electron,

$$L^{\mu\nu} \;=\; \frac{1}{2}\,\mathrm{Tr}\{\not{e}'\gamma^\mu \not{e}\gamma^\nu\} \;=\; 2\,\{e'^\mu e^\nu + e'^\nu e^\mu - g^{\mu\nu} e'\cdot e\}\,. \tag{2.5}$$

$W^{\mu\nu}$ is the hadronic tensor, related to the electromagnetic current $J^\mu$, which gives the hadronic part of unpolarized DIS [2],

$$\begin{aligned} W_{\mu\nu}(p,q) \;&=\; \frac{1}{4\pi}\int d^4z\, e^{iq\cdot z} <p\,|J_\nu(z)J_\mu(0)|\,p> \qquad (2.6)\\ &=\; \frac{1}{4\pi}\sum_X <p\,|\,J_\nu(0)\,|\,X><X\,|\,J_\mu(0)\,|\,p>\;(2\pi)^4\,\delta^4(p+q-p_X)\,. \end{aligned}$$

The second line is obtained after inserting the complete set of final states between the two electromagnetic currents, and using the translation invariance property of the current. The Lorentz structure of $W_{\mu\nu}$ is found from the conservation of the electromagnetic current, $q^\mu W_{\mu\nu} = 0$, and the symmetry $W_{\mu\nu} = W_{\nu\mu}$ due to parity conservation,

$$W_{\mu\nu}(p,q) \;=\; \left(-g_{\mu\nu} + \frac{q_\mu q_\nu}{q^2}\right) F_1 \;+\; \frac{1}{p\cdot q}\left(p_\mu - q_\mu\frac{p\cdot q}{q^2}\right)\left(p_\nu - q_\nu\frac{p\cdot q}{q^2}\right) F_2\,, \tag{2.7}$$

The unknown scalar *structure functions* $F_1(x,Q^2)$ and $F_2(x,Q^2)$, characterize the hadron structure revealed in unpolarized DIS with $Z$ and $W$ boson exchanges neglected.

The hadronic tensor $W_{\mu\nu}$ is related to the imaginary part of the forward

[2] We use the notation $<p\,|...|\,p> = 1/2\sum_\lambda <p\,\lambda\,|...|\,p\,\lambda>$ where the summation is performed over the proton polarization, and $p$ is the proton momentum.

$\gamma^* p$ scattering amplitude $T_{\mu\nu}$,

$$W_{\mu\nu} = \frac{1}{2\pi} \operatorname{Im} T_{\mu\nu} \,, \tag{2.8}$$

where

$$T_{\mu\nu} = i \int d^4 z \, e^{iq\cdot z} \, <p \,|\, \mathrm{T}(J_\nu(z) J_\mu(0)) \,|\, p> \;\; . \tag{2.9}$$

With some care with respect to the definition of the virtual photon flux and using the optical theorem, the structure functions can be related to the $\gamma^* p$ cross sections for the transverse and longitudinal polarized virtual photon, $\sigma_T$ and $\sigma_L$, respectively,

$$2xF_1 \;\; = \;\; \frac{Q^2}{4\pi^2 \alpha_{em}} \, \sigma_T \;\equiv\; F_T \,, \tag{2.10}$$

$$F_2 - 2xF_1 \;\; = \;\; \frac{Q^2}{4\pi^2 \alpha_{em}} \, \sigma_L \;\equiv\; F_L \,. \tag{2.11}$$

Thus, the newly defined transverse and longitudinal structure functions obey

$$F_2 \;=\; F_T \;+\; F_L \,. \tag{2.12}$$

The final form of the DIS cross section (2.4) is obtained after contracting the tensors (2.5) and (2.7),

$$\frac{d\sigma}{dx\, dQ^2} \;\; = \;\; \frac{2\pi \, \alpha_{em}^2}{x \, Q^4} \;\; \left[ (1 + (1-y)^2) \; F_2(x, Q^2) \;\; - \;\; y^2 \, F_L(x, Q^2) \right] \tag{2.13}$$

where

$$y \;\equiv\; \frac{p \cdot q}{p \cdot e} \;\; = \;\; \frac{Q^2}{x \, s} \tag{2.14}$$

is another useful variable used in the DIS description. In the proton rest frame $y$ is a fraction of incoming electron energy transfered into the hadronic system. Both $x$ and $y$ obey: $0 < x, y < 1$.

The structure functions describe the proton structure as measured in inclusive DIS. From the theoretical point of view the major task is to provide an explanation or prediction for their form.

## 2.2 Partons and their distributions

In the key experiment, performed at SLAC, $ep$ DIS was studied in the *Bjorken limit*: $Q^2, 2p \cdot q \to \infty$ and $x$ fixed. In this limit, the structure functions exhibit *Bjorken scaling* [1], i.e. they approximately depend only on the dimensionless variable $x$,

$$F_i(x, Q^2) \;\approx\; F_i(x) \,, \qquad\qquad i = 1, 2 \,. \tag{2.15}$$

To a good approximation the Callan-Gross relation is fulfilled, $F_2 - 2xF_1 = F_L \approx 0$. As we will see, this relation has a physical meaning.

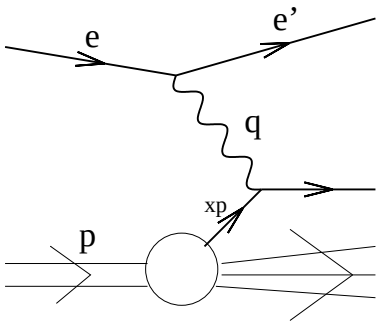


Figure 2.2: *Deep inelastic scattering in the parton model.*

The interpretation of scaling is due to Feynman [2, 3]. He envisaged the proton as a collection of point-like, non-interacting among themselves particles, called *partons*. In the infinite-momentum frame in which the proton moves very fast, the relativistic time dilation slows down the rate at which partons interact. As a result, the virtual photon interacts with an individual parton without disturbing the rest of the system. The total cross section is a sum over *incoherent* $\gamma^*$-parton interactions, weighted by the probability $f(\xi)$ to find a parton in a fast moving proton with a fraction $\xi$ of the proton momentum,

$$\frac{d\sigma}{dx\,dQ^2} \;=\; \int_0^1 d\xi\; f(\xi)\;\frac{d\tilde{\sigma}(\xi)}{dx\,dQ^2}\,. \tag{2.16}$$

In this way the distribution of partons in a proton, $f(\xi)$, is introduced. The above formula reflects factorization of the DIS cross section into a short distance interaction, described by the partonic cross section $d\tilde{\sigma}(\xi)$, and a long distance structure, described by the parton distribution $f(\xi)$.

Assuming that partons are Dirac fermions with spin 1/2 carrying the fraction $\xi$ of the proton's momentum, the following result is found in the parton model [4]

$$F_2(x) \;=\; 2xF_1(x) \;=\; \sum_i e_i^2 \int_0^1 d\xi\;\delta(x-\xi)\;\xi f_i(\xi) \;=\; \sum_i e_i^2\; x\, f_i(x)\,. \tag{2.17}$$

where $e_i$ is the electric charge. Additionally, the parton transverse momenta with respect to the proton direction are neglected. The Callan-Gross relation results from the spin 1/2 assumption.

Scaling is explained by the parton model. Moreover, Bjorken-$x$ is equal to the momentum fraction of the struck parton since from the momentum conservation at the $\gamma^*$-parton vertex, see Fig. 2.2, we have

$$(\xi\, p+q)^2 \;=\; 0 \qquad\Rightarrow\qquad \xi \;=\; -q^2/2p\cdot q \;=\; x\,. \tag{2.18}$$

Thus, the structure function $F_2(x)$ "measures" the parton distributions of the proton. Let us emphasize that partonic interpretation is inherent to the infinite-momentum frame in which DIS is viewed.

## 2.3 Parton model justification

The justification of the parton model comes from Quantum Chromodynamics (QCD) [5, 6]. QCD is the unbroken SU(3) gauge theory of strong interactions with fermionic quark fields and bosonic gluon fields. Both types of fields carry quantum number related to local gauge group, called *colour*.

The most important property of QCD is *asymptotic freedom* [6]. The effective coupling constant $\alpha_s(Q^2)$, describing the strength of interactions between quarks and gluons, vanishes when the scale $Q^2 \to \infty$. The $Q^2$-dependence is governed by the renormalization group equation. In the lowest order

$$\alpha_s(Q^2) \;=\; \frac{1}{b_0 \ln(Q^2/\Lambda^2)}\,, \tag{2.19}$$

where $b_0 = (33 - 2N_f)/12\pi$ is positive (for a reasonable number $N_f$ of quark flavours) and $\Lambda$ is the basic mass parameter of QCD (of the order 200 MeV) introduced by the renormalization procedure. The above formula is valid for $Q^2 \gg \Lambda^2$, when $\alpha_s(Q^2) \ll 1$ and perturbative description in terms of interacting weakly quarks and gluons makes sense. For $Q^2 \to \Lambda^2$ the strong coupling constant becomes large and perturbative methods break down. It means that the region of *confinement* is reached in which quarks and gluons form strongly bound colourless systems, observed as asymptotic hadronic states.

It is natural to interpret partons as the quarks and gluons. Asymptotic freedom means that QCD is asymptotically free, i.e. it approaches free-field theory at short distances with logarithmic modifications. This leads to the observed experimentally *logarithmic violation* of Bjorken scaling for matrix elements of electromagnetic currents between on-mass-shell states [7]. In contrast to the naive parton model, in QCD the struck quark can acquire large transverse momentum by emitting a gluon which effect gives scaling violation.

There are two approaches to describe DIS in the Bjorken limit using QCD. The first approach is based on the operator product expansion (OPE) of the product of two electromagnetic currents. The second one relies on direct calculations using Feynman diagrams, combined with a factorization theorem which allows to separate the short and long distance structure.

### 2.3.1 Operator product expansion for DIS

Historically, the first justification of the parton model came through the operator product expansion (OPE) of the electromagnetic currents in the hadronic tensor $W_{\mu\nu}$, eq. (2.6). In the Bjorken limit, the dominant contribution to $W_{\mu\nu}$ comes from the region of integration close to the light cone, see e.g. [8],

$$0 \le z^2 \le \mathrm{const}/Q^2\,, \tag{2.20}$$

Thus, the OPE around the light cone is relevant when $Q^2 \to \infty$. Ignoring, for simplicity, the vector character of the current, we have [9]

$$J(z)J(0) \;=\; \sum_{n=0}^{\infty} \sum_{A} C_n^A(z^2)\; z^{\mu_1} \cdots z^{\mu_n}\, \mathcal{O}^A_{\{\mu_1 \cdots \mu_n\}}(0)\,. \tag{2.21}$$

The expansion is singular at $z^2 = 0$, and $W_{\mu\nu}$ is determined from the singularity structure, contained entirely in the *coefficient functions* $C_n^A$ called also *Wilson coefficients*. The operators $\mathcal{O}^{\mathcal{A}}$ are well behaved local *composite operators*, symmetric and traceless in Lorentz indices (which is indicated by the curly brackets). In this case $n$ is the value of *spin* of the composite operator, and $A$ distinguishes operators with the same spin.

From naive dimensional counting in the units of mass, the Wilson coefficients behave in the following way in the limit $z \to 0$

$$C_n^A(z^2) \;\sim\; \left(\frac{1}{z^2}\right)^{d_J-(d_{\mathcal{O}}-n)/2}\,, \tag{2.22}$$

where $d_J(=3)$ and $d_{\mathcal{O}}$ are canonical dimensions of the current $J$ and the composite operator $\mathcal{O}^{\mathcal{A}}$, respectively. Relation (2.22) is true for free field theory while in QCD it obtains logarithmic modifications. The difference

$$\tau \equiv d_{\mathcal{O}} - n \tag{2.23}$$

is called *twist* of the composite operator, and its value determines the singularity structure of the coefficient functions. The most singular (dominant) term in (2.21) is given by the lowest twist operators. These are the operators with $\tau = 2$, which give Bjorken scaling in free field theory. The higher twist terms are suppressed by additional powers of $1/Q^2$.

From now on we limit our discussion to the leading twist-2 operators. The relevant QCD operators are: the quark flavour nonsinglet $\mathcal{O}_n^{NS,i}$, quark singlet $\mathcal{O}_n^S$, and gluon $\mathcal{O}_n^G$ operators,

$$\mathcal{O}^{NS,i}_{\{\mu_1\cdots\mu_n\}} \;=\; \bar\psi\,\lambda^f\,\gamma_{\{\mu_1}\,\mathrm{i}\overleftrightarrow{\mathcal{D}}_{\mu_2}\cdots\mathrm{i}\overleftrightarrow{\mathcal{D}}_{\mu_n\}}\,\psi\,, \tag{2.24}$$

$$\mathcal{O}^{S}_{\{\mu_1\cdots\mu_n\}} \;=\; \bar\psi\,\gamma_{\{\mu_1}\,\mathrm{i}\overleftrightarrow{\mathcal{D}}_{\mu_2}\cdots\mathrm{i}\overleftrightarrow{\mathcal{D}}_{\mu_n\}}\,\psi\,, \tag{2.25}$$

$$\mathcal{O}^{G}_{\{\mu_1\cdots\mu_n\}} \;=\; F_{\{\mu_1\alpha}\,\mathrm{i}\overleftrightarrow{\mathcal{D}}_{\mu_2}\cdots\mathrm{i}\overleftrightarrow{\mathcal{D}}_{\mu_{n-1}}F^{\alpha}_{\mu_n\}}\,, \tag{2.26}$$

where $i = 1, 2, \cdots, N_f^2 - 1$, $\lambda^f$ are the generators of the flavour group $SU(N_f)$ and the covariant derivative $\overleftrightarrow{\mathcal{D}} = (\overrightarrow{\mathcal{D}} - \overleftarrow{\mathcal{D}})/2$. The trace over colour indices in the above is implicit. There is an infinite tower of the twist-2 operators enumerated by spin $n$.

Plugging (2.21) (with the tensor structure modifications for vector currents) into the forward Compton scattering tensor $T_{\mu\nu}$, eq. (2.9), we obtain the analytic expansion in the unphysical region of $\omega = 1/x < 1$ in the Bjorken limit. Schematically, $T_{\mu\nu}(\omega) = \sum_n a_{\mu\nu,n}\,\omega^n$, where $a_{\mu\nu,n}$ involve products of the Wilson coefficients $C^A$ and matrix elements of the composite operators $< p|\mathcal{O}^A|p >$. The analytical structure of $T_{\mu\nu}(\omega)$ in the complex $\omega$-plane is given by cuts along $(-\infty, -1)$ and $(1, \infty)$ on the real axis. Therefore, using analyticity we can rewrite $a_{\mu\nu,n}$ in the form of the integrals over discontinuities of $T_{\mu\nu}(\omega)$ along the cuts, i.e. in the physical region of $|\omega = 1/x| > 1$. These discontinuities, in turn, are related to the hadronic tensor $W_{\mu\nu}$, eq. (2.8), and hence to the DIS

structure functions $F_i$. Finally, the following relation is found for the Mellin moments of the structure functions [10]

$$\int_0^1 dx\; x^{n-2}\; F_i(x,Q^2) \;=\; \sum_A C_{n,i}^A(Q^2)\; M_n^A\,, \tag{2.27}$$

where $i = 2, L$ and the Wilson coefficient $C_{n,i}^A(Q^2)$ are the Fourier transforms of the $z^2$-dependent coefficient functions in eq. (2.21), see [10]. The coefficients $M_n^A$ parameterize the *diagonal* matrix elements of the composite operators between nucleon states

$$<p\,|\,\mathcal{O}^A_{(\mu_1\cdots\mu_n)}\,|\,p> \;=\; M_n^A\; p_{(\mu_1}\cdots p_{\mu_n)}\,. \tag{2.28}$$

Notice that the tensor structure on the r.h.s of (2.28) is unique since we only have the nucleon momentum $p_\mu$ at our disposal.

Up to now, we have neglected the necessity of renormalization. The matrix elements of the operators appearing in the OPE are divergent and need to be renormalized. This procedure introduces a renormalization scale $\mu$ into the problem. The change of $\mu$ can be absorbed by the change of parameters of a theory, that leads to the renormalization group (RG) equation for the running parameters and matrix elements of the considered operators. Applying this method to the OPE (2.21) for a massless theory, we find as a consistency condition

$$\sum_A \left[\left(\mu^2\frac{\partial}{\partial\mu^2} \;+\; \beta(\alpha_s)\frac{\partial}{\partial\alpha_s}\right)\,\delta_{AB} \;+\; (\gamma_n(\alpha_s))_{AB}\right]\; C_{n,i}^A(Q^2/\mu^2,\alpha_s) \;=\; 0\,, \tag{2.29}$$

where we indicated the presence of the renormalization scale $\mu$ in the Wilson coefficient. $\beta(\alpha_s)$ is the Gell-Mann-Low function, and $\gamma_n(\alpha_s)$ is the matrix of *anomalous dimensions* of the composite operators $\mathcal{O}^A$ with spin $n$. They mix under renormalization if they have the same quantum numbers. The quark singlet and gluon operators (2.25) and (2.26) are examples of such operators.

Both $\beta(\alpha_s)$ and $\gamma_n(\alpha_s)$ are computed in pQCD as a series in powers of $\alpha_s$:

$$\beta(\alpha_s) \;=\; -\alpha_s^2\; b_0 \;+\; \alpha_s^3\; b_1 \;+\; \cdots\,, \tag{2.30}$$

$$\gamma_n(\alpha_s) \;=\; \left(\frac{\alpha_s}{2\pi}\right)\,\gamma_n^{(0)} \;+\; \left(\frac{\alpha_s}{2\pi}\right)^2\,\gamma_n^{(1)} \;+\; \cdots\,, \tag{2.31}$$

where $b_0$ is defined in eq. (2.19), and $\gamma_n^{(0)}$ were found for the operators (2.24)-(2.26) in Ref. [7]. The famous minus sign in the expansion of the $\beta$ function leads to asymptotic freedom of QCD. The running coupling constant (2.19) is a solution of the equation

$$Q^2\,\frac{d\alpha_s(Q^2)}{dQ^2} \;=\; \beta(\alpha_s(Q^2))\,, \tag{2.32}$$

with $\beta(\alpha_s)$ in the lowest order approximation.

The solution to the RG equation (2.29) is given in terms of the running coupling constant. In the lowest order approximation for $\beta$ and $\gamma_n$, we find

$$C_{n,i}(Q^2/\mu^2, \alpha_s(\mu^2)) \;=\; C_{n,i}(1, \alpha_s(Q^2)) \left[\frac{\alpha_s(\mu^2)}{\alpha_s(Q^2)}\right]^{\frac{\gamma_n^{(0)}}{2\pi b_0}}, \tag{2.33}$$

where the matrix notation is assumed, and $\alpha_s$ is given by (2.19).

When the renormalization procedure is performed, the coefficients $C_{n,i}^A$ and $M_n^A$ in eq. (2.27) acquire the $\mu$-dependence. Now, we have

$$\int_0^1 dx\; x^{n-2}\; F_i(x, Q^2) \;=\; C_{n,i}(Q^2/\mu^2, \alpha_s(\mu^2))\, M_n(\mu^2)\,, \tag{2.34}$$

where the solution (2.33) is substituted. The l.h.s in the above is a measured quantity and obviously does not depend on a renormalization point $\mu$. Therefore, differentiating both sides with respect to $\mu$, we find the following RG equation for the coefficients $M_n^A$

$$\mu^2\, \frac{dM_n^A(\mu^2)}{d\mu^2} \;=\; \frac{\alpha_s(\mu^2)}{2\pi} \sum_B \left(\gamma_n^{(0)}\right)_{AB} M_n^B(\mu^2)\,. \tag{2.35}$$

The renormalization scale $\mu$ is arbitrary, thus, we are free to choose $\mu = Q \gg \Lambda$. In such a case (2.34) becomes

$$\int_0^1 dx\; x^{n-2}\; F_i(x, Q^2) \;=\; \sum_A C_{n,i}^A(1, \alpha_s(Q^2))\; M_n^A(Q^2)\,, \tag{2.36}$$

where $i = 2, L$. In this way the *logarithmic scaling violation* for the structure functions is found [7] due to the running coupling constant $\alpha_s$, and the evolution governed by the anomalous dimensions of the twist-2 operators (2.24)-(2.26).

We have to keep in mind that our discussion concerns the leading behaviour of the structure functions, therefore, it applies to large $Q^2$, when QCD is asymptotically free. In general, the OPE leads to the following expansion in powers of $1/Q^2$ in the Bjorken limit[3]

$$F_{2,L}(x, Q^2) \;=\; F_{2,L}^{(\tau=2)}(x, Q^2) \;+\; F_{2,L}^{(\tau=4)}(x, Q^2)\, \frac{\Lambda^2}{Q^2} + \cdots\,, \tag{2.37}$$

where the twist-2 part is found by inverting the Mellin moments (2.36). The twist-4 (and higher) contribution has to be analyzed independently by considering twist-4 operators and their logarithmic in $Q^2$ evolution [11].

In summary, QCD predicts the breakdown of Bjorken scaling, described by eq. (2.36). The Wilson coefficients $C_{n,i}^A$ are computed in pQCD. The coefficients $M_n^A(Q^2)$, however, are not determined until initial conditions at some scale $Q_0^2 \gg \Lambda^2$ are provided for eqs. (2.35). Thus, despite the evolution is driven by the perturbatively computed anomalous dimensions, the nonperturbative aspect is encoded in the initial conditions for the evolution. This is a manifestation of the short- and long-distance factorization present in the OPE.

[3]Other sources of $1/Q^2$ corrections are provided by target mass corrections, relevant at large $x$, or resummation effects like renormalons.

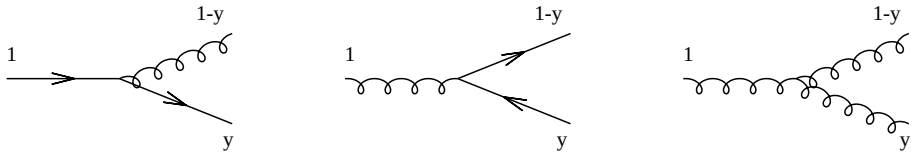


Figure 2.3: *The elementary processes described by the splitting functions $P_{qq}(y)$, $P_{qG}(y)$ and $P_{GG}(y)$ from the left to the right, respectively. Additionally, $P_{Gq}(y) = P_{qG}(1-y)$.*

### 2.3.2 The Altarelli-Parisi formulation

In [12] Altarelli and Parisi reinterpreted the main results of the previous section on the scaling violation in terms of parton distributions and basic interactions between partons being quarks and gluons.

They identified the Mellin moments of the *parton distributions* $f_A(x,Q^2)$ with the coefficients $M_n^A(Q^2)$ from eq. (2.28),

$$\int_0^1 dx\, x^{n-1}\, f^A(x,Q^2) \;=\; M_n^A(Q^2)\,, \tag{2.38}$$

where we denote collectively $f^A = (q_{NS},\ q_S,\ g)$, the quark flavour nonsinglet, singlet and gluon distributions, respectively. Let us recall that $M_n^A$ characterize matrix elements of the twist-2 QCD operators $\mathcal{O}^A$, see eq. (2.28). Choosing an additional light-like vector $\hat{n}_\mu$ such that $\hat{n}\cdot p = 1$, we find the following relation

$$\int_0^1 dx\, x^{n-1}\, f^A(x,Q^2) \;=\; \hat{n}^{\mu_1}\cdots\hat{n}^{\mu_n}\; <p\,|\,\mathcal{O}^A_{(\mu_1\cdots\mu_n)}\,|\,p>_{\mu=Q}\,, \tag{2.39}$$

The matrix elements in the above cannot be computed in pQCD, only their change with $Q$ is governed by the RG equation. Thus, the parton distributions are of nonperturbative nature, and their determination can be attempted in lattice formulation of QCD or, indirectly, with the help of experimental data.

The next step is the identification of the anomalous dimension $(\gamma_n^{(0)})_{AB}$, eq. (2.31), with the moments of the *splitting functions* $P_{AB}(y)$

$$\int_0^1 dy\, y^{n-1}\, P_{AB}(y) \;=\; (\gamma_n^{(0)})_{AB}\,. \tag{2.40}$$

The splitting functions were computed in [12] from basic vertices of QCD, using the generalization of equivalent photon method. They describe the elementary processes, shown in Fig. 2.3, independent of the quark flavour.

Relation (2.38) can be inverted, and after that the evolution equations (2.35) are rewritten in the following form[4]

$$Q^2\,\frac{\partial f^A(x,Q^2)}{\partial Q^2} \;=\; \frac{\alpha_s(Q^2)}{2\pi}\int_x^1 \frac{dy}{y}\, P_{AB}(y)\; f^B\big(x/y,Q^2\big)\;, \tag{2.41}$$

[4]Using the property of the Mellin moments: $A_n B_n \leftrightarrow (A\otimes B)(x) = \int_x^1 dy/y\, A(y)\, B(x/y)$

where the summation over $B$ is implicit and the splitting function matrix equals

$$P_{AB} \;=\; \begin{pmatrix} P_{qq} & 0 & 0 \\ 0 & P_{qq} & P_{qG} \\ 0 & P_{Gq} & P_{GG} \end{pmatrix} .$$

These are the Altarelli-Parisi evolution equations, derived for abelian theories before the advent of QCD by Gribov and Lipatov [13] and independently, following the method of [13], by Dokshitzer for QCD [14]. Notice that the quark nonsinglet distribution evolves independently of the quark singlet and gluon distributions. This occurs because the corresponding partonic operator $\mathcal{O}^f$ does not mix under renormalization with the operators $\mathcal{O}^S$ and $\mathcal{O}^G$.

The Altarelli-Parisi (DGLAP) equations have probabilistic interpretation. In the infinite momentum frame, the parton distributions $f^A(x, Q^2)$ describe probability to find quark or gluon in a hadron, carrying a fraction $x$ of hadron's momentum, as seen by the probe with a virtuality $Q^2$. The evolution equations describe the change of this probability with the resolution power $Q^2$, due to the emission of partons described by the splitting functions.

Relation (2.36) for the moments of the structure functions can also be inverted. After that we find the following formula for the structure functions

$$F_i(x, Q^2) \;=\; \sum_A \int_x^1 \frac{dy}{y}\, C_i^A(y, \alpha_s(Q^2))\; x f^A\left(x/y, Q^2\right) , \tag{2.42}$$

where $i = 2, L$ and *coefficient functions* $C_i^A(y)$ are related to the the Wilson coefficients $C_{n,i}^A$ from the previous section through the Mellin transformation. Formula (2.42) reflects the short- and long-distance factorization, called *collinear factorization*, in which the coefficient functions are computed in perturbative QCD while the parton distributions contain information about nonperturbative structure of the nucleon. In the lowest order in $\alpha_s$ for the coefficient functions $F_L = 0$ and

$$F_2(x, Q^2) \;=\; \sum_f e_f^2\, \{x q_f(x, Q^2) \;+\; x\bar{q}_f(x, Q^2)\} . \tag{2.43}$$

where the sum over quark flavours is performed. In order to find the parton distributions, we have to specify initial conditions for the DGLAP evolution equations at some scale $Q_0^2 \gg \Lambda^2$. In practice, an analytical form in $x$ of the initial conditions is given in terms of several parameters. Then, the parameters are determined from a fit to DIS data.

### 2.3.3 Evolution in diagrams

By summation over a class of infinitely many diagrams the DGLAP equations can be directly obtained from perturbative QCD [14]. This method serves as a starting point for the computations beyond the leading order.

In brief, the DIS structure functions is computed using the optical theorem (2.8). The relevant class of diagrams are ladder diagrams, with the cut states being on mass-shell, see Fig. 2.4. We treat for a moment the lowest lying

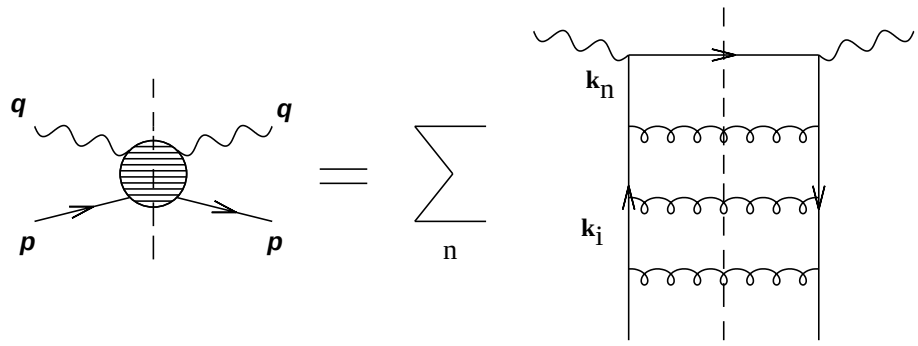


Figure 2.4: *QCD ladder diagrams contribution to DIS structure functions.*

incoming parton as a hadron with a small virtuality $-m^2$, which serves as a regulator in the calculation. The diagrams with $n$ cells amount the contribution $\alpha_s^n \log^n(Q^2/m^2) \sim 1$. Thus, the large logarithms $\log(Q^2/m^2)$ compensate for the smallness of $\alpha_s$ in each order $n$ and have to be resummed. The key element for the dominance of the ladder diagrams is the choice of the planar gauge for the gluon field. As shown in [15], other diagrams, including non-planar ones, are suppressed by additional powers of $\alpha_s$ without accompanying logarithms, and are neglected. Such an approximation is called *leading-logarithmic approximation* (LLA).

The leading-logarithmic expression for the structure functions is obtained after the integration over exchanged parton momenta [15],

$$k_i \;=\; \alpha_i\, p' \;+\; \beta_i\, q' \;+\; k_{\perp i}\,, \tag{2.44}$$

in the configuration strongly *ordered* in the transverse momenta

$$m^2 \;\ll\; |k_{\perp 1}^2| \;\ll\; |k_{\perp 2}^2| \;\ll \cdots \ll |k_{\perp n}^2| \;\ll\; Q^2\,. \tag{2.45}$$

Here the Sudakov decomposition of momenta is adopted with the null base vectors defined by $q' = q + x_B p$ and $p' = p + (m^2/s)q'$, where $p^2 = -m^2$ and $2p' \cdot q' \equiv s \sim Q^2$. The longitudinal momentum fractions are also ordered due to mass-shell condition imposed on the emitted gluons (cut in Fig. 2.4),

$$1 \;>\; \alpha_1 \;>\; \alpha_2 \;> \cdots > \alpha_n \;\approx\; x\,. \tag{2.46}$$

The $\beta_i$ variables are small ($\sim m^2/s$) and can be integrated out. Thus, the successive parton emissions are in the proton momentum direction $p \approx p'$.

Condition (2.45) leads to the improved parton picture. From the point of view of the quark $(i-1)$, the upward quark $(i)$ looks as a probing (bare) particle, with much larger virtuality. As we move upwards, the quark $(i)$ becomes "dressed" (in cloud of partons with smaller virtualities) for the quark $(i+1)$, which now acts as a highly virtual probe. Therefore, increasing virtuality, the number of decays increases, and the cloud of virtual particles is penetrated more deeply (at shorter transverse distances). This is a physical picture behind the scaling violation in the LLA.

The large logarithms come from the integration over the ordered transverse momenta. Each cell contributes one power of $\alpha_s$ and logarithmic integral. Thus, the integration over $n$ cells gives

$$\alpha_s^n \int_{m^2}^{Q^2} \frac{d|k^2_{\perp n}|}{|k^2_{\perp n}|} \int_{m^2}^{|k^2_{\perp n}|} \frac{d|k^2_{\perp n-1}|}{|k^2_{\perp n-1}|} \cdots \int_{m^2}^{|k^2_{\perp 2}|} \frac{d|k^2_{\perp 1}|}{|k^2_{\perp 1}|} \;=\; \frac{\alpha_s^n}{n!} \log^n \frac{Q^2}{m^2}\,. \qquad (2.47)$$

The integration over the longitudinal variables $\alpha_i$ leads to a convolution of $n$ splitting functions $P_{qq}$. After the transformation into the Mellin space a simple factor with anomalous dimension is obtained: $(\gamma_N^{(0)}/2\pi)^n$. Thus, we find for the Mellin moments of the structure function $F_2$

$$F_{2\,N-1}(Q^2) \;=\; \sum_{n=0}^{\infty} \frac{\alpha_s^n}{n!} \log^n \frac{Q^2}{m^2} \left(\frac{\gamma_N^{(0)}}{2\pi}\right)^n \;=\; \left(\frac{Q^2}{m^2}\right)^{\frac{\alpha_s\,\gamma_N^{(0)}}{2\pi}}\,. \qquad (2.48)$$

The small virtuality $-m^2$ of the incoming parton cannot be set to zero due to *collinear singularity* which appears when a massless parton decays into two collinear massless partons. The remedy is to assume that there exists a sufficiently hard *factorization scale*[5] $\mu_F \gg \Lambda$. With this scale, the *short-distance* part, given by the integration over the transverse momenta $\mu_F < |k_\perp| < Q$, is safe from the point of view of perturbative calculations. The *long-distance* part, $m < |k_\perp| < \mu_F$, can be factored out and absorbed into the unknown bare distribution of the parent parton in a nucleon $q^0$. Thus, we have

$$F_{2\,N-1}(Q^2) \;=\; \left(\frac{Q^2}{\mu_F^2}\right)^{\frac{\alpha_s\,\gamma_N^{(0)}}{2\pi}} \underbrace{\left(\frac{\mu_F^2}{m^2}\right)^{\frac{\alpha_s\,\gamma_N^{(0)}}{2\pi}} q_N^0}_{q_N(\mu_F)}\,. \qquad (2.49)$$

As a measured quantity, $F_{2\,N-1}(Q^2)$ does not depend on the factorization scale. Thus we can write the RG equations for $q_N(\mu_F)$ by differentiation of both sides of (2.49) with respect to $\mu_F$. Choosing $\mu_F = Q$, the evolution equation for the Mellin moments of the parton distribution is found

$$Q^2\,\frac{dq_N(Q^2)}{dQ^2} \;=\; \frac{\alpha_s}{2\pi}\,\gamma_N^{(0)}\; q_N(Q^2)\,. \qquad (2.50)$$

In the presentation, the coupling constant was fixed, but the running $\alpha_s$ can be consistently included by considering the next-to-leading logarithmic approximation (NLLA), in which the terms proportional to $\alpha_s(\alpha_s \log(Q^2/m^2))^n$ are summed up. In this case, the splitting functions $P(\alpha_s, x)$ and coefficient functions $C(\alpha_s, x)$ are computed to a higher order in $\alpha_s$ [16]. In general

$$P(\alpha_s, x) = \left(\frac{\alpha_s}{2\pi}\right) P^{(0)}(x) \;+\; \left(\frac{\alpha_s}{2\pi}\right)^2 P^{(1)}(x) \;+\; \left(\frac{\alpha_s}{2\pi}\right)^3 P^{(2)}(x) \;+\; \cdots \qquad (2.51)$$

$$C(\alpha_s, x) = C^{(0)}(x) \;+\; \alpha_s\; C^{(1)}(x) \;+\; \alpha_s^2\; C^{(2)}(x) \;+\; \cdots\,, \qquad (2.52)$$

[5] In most calculations $\mu_F = \mu$, the renormalization scale related to ultraviolet divergences.

where (0) refers to LLA, (1) to NLLA, (2) to NNLLA and so on. The running coupling constant also has to be computed to the appropriate order.

The parton distributions are universal for a given hadron in a sense that the same distributions can be used in the cross sections for which collinear factorization holds. Usually, it is a matter of nontrivial proofs in which infrared structure of pQCD is carefully examined, see Collins *et al.* in Ref. [17].

## 2.4 DIS in Regge limit

Expansions (2.51) truncated at some order are good approximations away from $x = 0$. In the limit $x \to 0$, however, large logarithms $\log(1/x)$ appear in all orders except the lowest one [6]. Thus, the perturbative expansion (2.51) becomes slowly (or badly) convergent because of the presence of large logarithmic corrections. A systematic method of resummation of these corrections is necessary in order to restore the reliability of QCD in the small $x$ domain.

In the standard DGLAP approach, the following hierarchy of scales is assumed to assure that $x \sim 1$

$$W^2 \sim Q^2 \gg \Lambda^2 , \tag{2.53}$$

where $W$ is the $\gamma^* p$ center-of-mass energy (2.3). The second condition justifies the use of perturbative QCD. For the fixed target DIS experiments condition (2.53) holds true. With the advent of the $ep$ collider HERA, however, the study of a new limit of DIS has started in which $W$ is much bigger than any other scale involved. In particular,

$$W^2 \gg Q^2 \gg \Lambda^2 . \tag{2.54}$$

This condition corresponds to the *Regge limit* of DIS. In such a case $x \ll 1$, and the fixed order DGLAP approach is incomplete. The DIS processes in the limit (2.54) are called *semi-hard*. They are similar to soft hadronic processes in the sense that energy is much bigger than the 'mass' of the projectile $Q$. On the other hand these processes are hard since $\alpha_s(Q^2) \ll 1$ and pQCD is applicable.

In the leading twist description of DIS at small $x$, the resummation of large $\log(1/x)$ terms is necessary in the singlet and gluon splitting functions (2.51), and in the coefficient functions (2.52). The systematic method corresponds to the resummation of terms proportional to $\alpha_s^k \log^k(1/x)$ in the leading logarithmic approximation and subleading terms proportional to $\alpha_s^{n+k} \log^k(1/x)$ in the higher order approximations. In general

$$x\,P(\alpha_s, x) = \sum_{n=0}^{\infty} (\alpha_s)^n \left[ \sum_{k=1}^{n} p_k^{(n)} \log^k(1/x) \right] + \text{regular part} \tag{2.55}$$

$$C(\alpha_s, x) = \sum_{n=0}^{\infty} (\alpha_s)^n \left[ \sum_{k=1}^{n} c_k^{(n)} \log^k(1/x) \right] + \text{regular part} . \tag{2.56}$$

[6] There are also large logarithms $\log(1-x)$ when $x \to 1$. We are not discussing them here.

In the above, $k = n$ corresponds to the leading contribution whereas $k < n$ gives subleading corrections. In this way an improved perturbative expansion for (2.51) and (2.52) is obtained. In practice, the leading contribution is obtained using the $k_\perp$-factorization formula [33], discussed in section 2.4.3, in the collinear limit. This formula can be extended beyond the leading order in agreement with collinear factorization (2.42) by a careful examination of the region of low transverse momenta for parton emissions [34].

The large $\log(1/x)$ terms, however, are present in all twist contributions to the structure functions, making them as important as the leading twist contribution. The $k_\perp$-factorization formula also includes these corrections by keeping the $Q^2$-dependence exact. Thus, the new way of computation is a nontrivial extension of the leading twist formalism. Moreover, using the $k_\perp$-factorization, it was shown [18] that for fixed $Q^2 \gg \Lambda^2$ the operator product expansion breaks below some value of $x$ due to nonperturbative effects. A problem which arises in the new approach is unitarity of the computed cross sections. This is the main theoretical challenge in QCD of semi-hard processes, which we address phenomenologically in Chapter 3.

Before discussing the small-$x$ limit in QCD in detail, we describe the high energy limit of scattering processes using Regge theory which dominated in the pre-QCD era. This introduces the concept of a pomeron in terms of which the semi-hard processes are usually discussed.

### 2.4.1 Soft pomeron

Regge theory [19] allows to study the high energy limit of scattering reactions, based on general assumptions about the scattering matrix $S = 1 + iA$, like Lorentz invariance, crossing, unitarity and causality. From the last assumption follows the property of analyticity of the scattering matrix as a function of Lorentz invariants regarded as complex variables. The only singularities allowed are those imposed by unitarity conditions.

For the two-to-two scattering of spinless and massless particles the scattering amplitude $A(s,t)$ is an analytic function of the Mandelstam variables[7]. $A(s,t)$ describes three different reactions, depending on the domain of the kinematic invariants. We are interested in the *Regge limit* of the scattering amplitude,

$$s \to \infty, \qquad t = \text{const} \tag{2.57}$$

for the *s-channel* reaction, $a + b \to c + d$, with $s = (p_a + p_b)^2 > 0$ and $t = (p_a - p_c)^2 < 0$. For this purpose we consider scattering in the crossed *t−channel*, $a + \bar{c} \to \bar{b} + d$, with $t = (p_a + p_{\bar{c}})^2 > 0$ and $s = (p_a - p_{\bar{b}})^2 < 0$. The standard partial wave decomposition for this process reads

$$A(s,t) \;=\; \sum_{l=0}^{\infty} (2l+1)\, a_l(t)\, P_l(\cos\theta_t)\,. \tag{2.58}$$

The above expression is convergent for $|\cos\theta_t| = |1 + 2s/t| < 1$, i.e. throughout the $t-$channel physical region, $t > 0$ and $-t < s < 0$, but it quickly breaks

[7] The third Mandelstam variable $u = -s - t$.

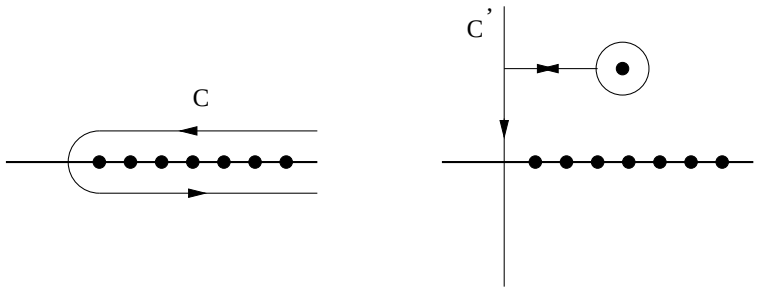


Figure 2.5: *Integration contour $C$ and its distortion in the complex angular momentum plane*

down when continued into the $s-$channel region $s > 0$ and $t < 0$. The appropriate analytic continuation of (2.58) is provided through the complex angular momentum plane $l$ [20],

$$A(s,t) \;=\; \frac{1}{2i}\oint_C dl\,\frac{2l+1}{\sin\pi l}\,\left\{\xi_l^{(+)}\,a_l^{(+)}(t)\;+\;\xi_l^{(-)}\,a_l^{(-)}(t)\right\}\,P_l\!\left(1+\frac{2s}{t}\right), \quad (2.59)$$

where $a_l^{(\pm)}$ are partial wave amplitudes with *signature* $\eta = \pm 1$, and $P_l$ is the Legendre polynomial, analytically continued in $l$. The functions $\xi_l^{(\pm)} = 1/2\,(\eta + \exp(-i\pi l))$ are called *signature factors*. The contour $C$ encircles the pole singularities at $l = 0, 1, 2, ...$, due to the denominator $\sin\pi l$, see Fig. 2.5. By computing residues of the poles encircled by $C$, we check that (2.59) provides analytic continuation of (2.58). The two signatured partial wave amplitudes in (2.59) are necessary for uniqueness of the analytic continuation. In this case, $a_l^{(+)}(t)$ is an analytic continuation of $a_l(t)$ for even $l$ and $a_l^{(-)}(t)$ for odd $l$. The signature factors allow to obtain (2.58) when the residues in (2.59) are computed.

With the representation (2.59), the Regge limit can be achieved by distorting the integration contour $C$ as shown in Fig. 2.5. On the way to the new contour $C'$, singularities of the partial wave amplitude $a_l^{(\eta)}(t)$ appear (cuts or poles), which have to be circumvented by winding the contour around. The usefulness of Regge theory is based on the assumption that there are only isolated singularities, cuts or poles. In the simplest nontrivial case, one simple pole, called *Regge pole*, is assumed,

$$a_l^{(\eta)}(t) \sim \frac{\beta(t)}{l-\alpha(t)}\,, \quad (2.60)$$

where the pole position $\alpha(t)$ is called *Regge trajectory* (with a definite signature), and $\beta(t)$ is a residue. In this case we find

$$A(s,t) \;=\; \frac{2\alpha(t)+1}{\sin\pi\alpha(t)}\;\xi^{(\eta)}_{\alpha(t)}\;\beta(t)\;P_{\alpha(t)}\!\left(1+\frac{2s}{t}\right)\;+\;A_{C'}(s,t)\,, \quad (2.61)$$

where $A_{C'}$ is the contribution given by the integration along the contour $C'$.

## A. Regge trajectory

When the Regge pole occurs for an integer value of $l_i = \alpha(t_i)$, then (2.61) has a pole at $t = t_i$, because of the denominator $\sin \pi\alpha(t_i)$. This corresponds to a physical meson bound state (or a resonance if Im $\alpha(t_i) \neq 0$), produced in the $t-$channel with mass $m_i = \sqrt{t_i}$ and spin $l_i$. It appears that most of the known mesons form families with the same quantum numbers but spin which lie on the straight line Regge trajectories

$$\alpha(t) \;=\; \alpha(0) \;+\; \alpha'\, t\,, \tag{2.62}$$

where $\alpha(0)$ is the *intercept*, and $\alpha'$ is the *slope* of the Regge trajectory. The signature factor ensures that particles lying on a Regge trajectory differ by two units of angular momentum.

The Regge trajectory continued to negative values of $t$ describes the scattering in the $s-$channel. In the Regge limit, $A_{C'} = 0$ in (2.61) and only the Regge pole contributes. We find [8] for large $s$

$$A(s,t) \;\sim\; \tilde{\beta}(t)\, s^{\alpha(t)}\,, \tag{2.63}$$

where the residue $\beta(t)$ and the signature factor $\xi^\eta$, were absorbed in $\tilde{\beta}(t)$. Therefore, the production of particles in the $t-$channel can be 'detected' in the $s-$channel from the asymptotic behaviour of the corresponding amplitude. It is usually said that the Regge trajectory (reggeon) is exchanged.

From the optical theorem, we have for large $s$

$$\sigma_{tot} \;=\; s^{-1}\, \mathrm{Im}A(s,0) \sim s^{\,\alpha(0)-1}\,. \tag{2.64}$$

Thus, the intercept of the Regge trajectory $\alpha(0)$ determines the asymptotic behaviour of the total cross section for the $s$-channel reaction. If many reggeons are exchanged, we add amplitudes with different trajectories. The dominant contribution is given by the trajectory with the highest intercept (the rightmost singularity in the $l$-plane).

The slope of the Regge trajectory $\alpha'$ is found from the $t$-dependence of elastic scattering amplitude [21].

## B. Pomeron

How useful are the presented concepts ? Donnachie and Landshoff performed a very economical fit to the total cross section data for various hadronic reactions, assuming the form (2.64) with two powers of $s$ [22]. As a result, they found

$$\sigma_{tot} \;=\; A\,(s/s_0)^{-0.45} \;+\; B\,(s/s_0)^{\,0.08}\,, \tag{2.65}$$

where $s_0 = 1$ GeV. The two powers are universal, but the coefficients $A$ and $B$ depend on a hadronic reaction. The first term corresponds to the exchange of the $(\rho, \omega, f, a)$-meson Regge trajectory

$$\alpha_R(t) \;=\; 0.55 \;+\; 0.86\ \mathrm{GeV}^{-2} \cdot t\,. \tag{2.66}$$

[8] Using the asymptotic formula $P_l(z) \propto \frac{\Gamma(2l+1)}{\Gamma^2(l+1)}\,(z/2)^l$ for large $z$.

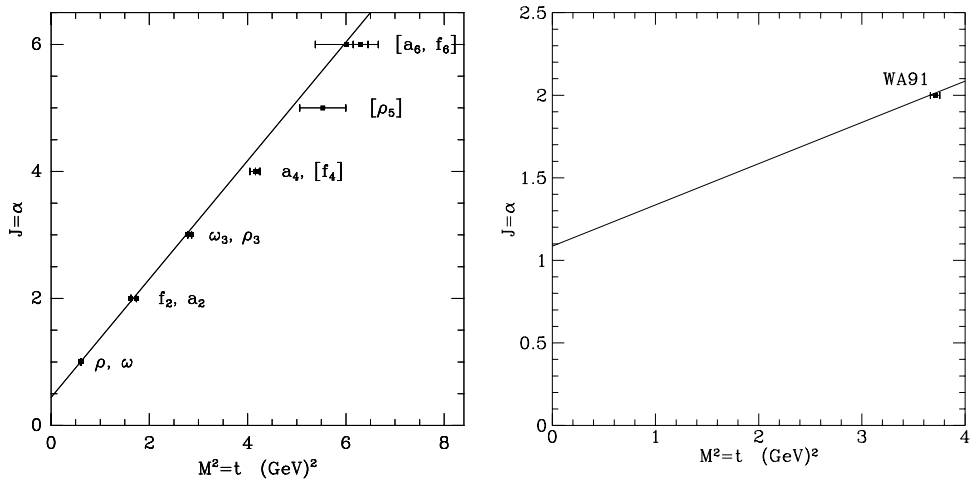


Figure 2.6: $(\rho, \omega, f, a)$-*meson and soft pomeron trajectories*

see Fig. 2.6. The second term in (2.65), responsible for the rise of the cross sections for large $s$, is attributed to the *pomeron* exchange.

By definition, the *pomeron trajectory* is the even signature ($\eta = 1$) Regge trajectory with the intercept $\alpha(0) \geq 1$ corresponding to the exchange of the vacuum quantum numbers[9]. In the Donnachie and Landshoff analysis the *soft pomeron* ($I\!P$) trajectory has the intercept slightly above one

$$\alpha_{I\!P}(t) \;=\; 1.08 \;+\; 0.25 \text{ GeV}^{-2} \cdot t\,. \tag{2.67}$$

Notice that the pomeron slope $\alpha'_{I\!P} = 0.25$ GeV$^{-2}$ is much smaller than the reggeon slope. Thus, if there is a real particle (with spin $l = 2$) lying on the soft pomeron trajectory, it has mass around 2 GeV, see Fig. 2.6. A glueball is a candidate, see [23] for a recent review.

However, there is a problem with the soft pomeron. If the energy dependence $s^{0.08}$ continues as $s \to \infty$, it will eventually come into conflict with the Froissart-Martin bound [24], reflecting unitarity

$$\sigma^{tot} \;\leq\; C \,\log^2 (s/s_0)\;, \tag{2.68}$$

where $C = \pi/m_\pi^2 \approx 60$ mb. Thus, the description with the help of the pomeron trajectory with $\alpha(0) > 1$ is inconsistent and more complicated singularities like cuts have to be considered. In the DL parameterization $s_0 = 1$ GeV$^2$, and the total cross sections lie much below the unitarity bound for present energies. Nevertheless, for diffractive processes the problem of unitarity is more acute.

## C. Application to DIS

Let us apply the concept of Regge trajectory exchanges to DIS at small $x$. Considering $\gamma^* p$ scattering, we may write the Donnachie-Landshoff parameter-

[9] i.e. parities $P = +1$, $C = +1$, $G = +1$ and isospin $I = 0$.

ization of the nucleon structure function $F_2 \sim Q^2\,\sigma_{\gamma^* p}$ as

$$F_2(x,Q^2) \;=\; A(Q^2)\,x^{1-\alpha_{I\!P}(0)} \;+\; B(Q^2)\,x^{1-\alpha_R(0)}\,. \tag{2.69}$$

Having in mind partonic interpretation, we expect the pomeron contribution to be given by flavour singlet sea quarks, while the reggeon term is determined by flavour nonsinglet valence quarks. Thus, we find for the proton and neutron structure functions

$$F_2^p \;\sim\; x^{-0.08} \qquad\qquad F_2^p \;-\; F_2^n \;\sim\; x^{0.5} \tag{2.70}$$

in the small $x$ limit. However, the measured at HERA proton structure function, $F_2 \sim x^{-\lambda(Q)}$, has a bigger effective power $\lambda(Q)$ than the soft pomeron value which additionally rises with $Q^2$. Such a behaviour can be accounted for by the DGLAP evolution equations due to flexibility in choosing initial conditions for the evolution. In particular, the dependence (2.70) can be incoporated in initial distributions at the scale $Q_0^2 \sim 1$ GeV$^2$ where nonperturbative Regge theory may be applicable. The strong rise of $F_2$ is also predicted by the analysis of the Regge limit of perturbative QCD.

### 2.4.2 Hard pomeron

In this section we present the main results on the Regge limit in QCD, based on a seminal work of the BFKL group [25]. The largest contribution to the scattering amplitude in this limit comes from leading logarithms in the center-of-mass energy $s$ in the kinematic region where

$$\alpha_s \ll 1, \qquad\qquad \alpha_s \log s \sim 1. \tag{2.71}$$

The approximation in which terms proportional to $(\alpha_s \log s)^n$ are summed is called the leading logarithmic approximation (LLA(s)).

Let us consider for illustration the elastic scattering of two quarks, see Fig. 2.7. In the Regge limit, exchanges of the highest spin elementary quanta (gluons) dominate. The imaginary part of the $qq \to qq$ amplitude is computed from the unitarity condition,

$$Im_s A^R(s,t) \;=\; \frac{P^R}{2} \sum_n \int d\Phi_{n+2}\; A(p_1,p_2;n+2)\,A^*(p_1',p_2';n+2)\,. \tag{2.72}$$

In such a case, two production amplitudes for the process $qq \to (ng)qq$ have to be squared and integrated over the final state particle momenta. $P^R$ is the colour projector on a representation $R$ of the gauge group. For the pomeron exchange, the projector on a singlet representation is relevant. The full amplitude can be reconstructed from the imaginary part using dispersion relations. In the LLA(s), which we consider from now on, the amplitude is purely imaginary.

There are three key elements in the computation of the r.h.s of eq. (2.72): the phase space, reggeized gluon and new effective vertices.

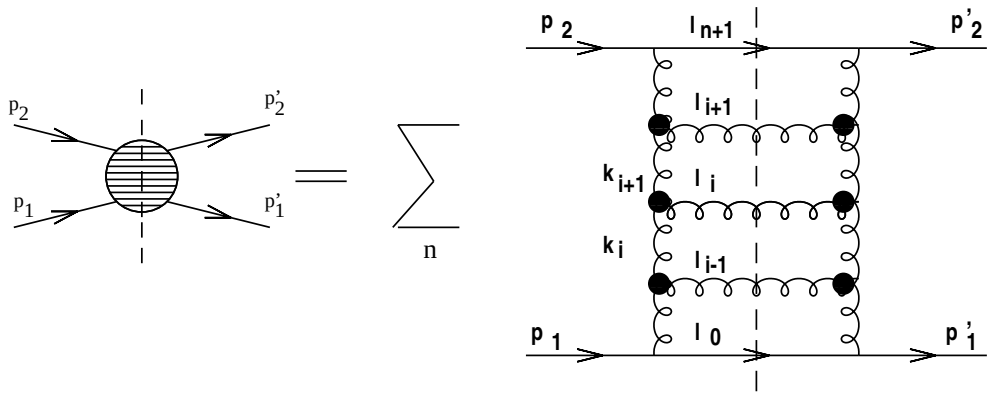


Figure 2.7: *Pomeron exchange in QCD.*

- The large logarithms of energy are obtained in the LLA(s) assuming multi-Regge kinematics for phase space of the final state particles. Parameterizing their momenta with the help of the Sudakov variables,

$$l_i \;=\; \alpha_i\, p_1 \;+\; \beta_i\, p_2 \;+\; l_{\perp i}\,, \tag{2.73}$$

where $p_1^2 = p_2^2 = 0$ and $2p_1 \cdot p_2 = s$, the multi-Regge kinematics is defined by the conditions

$$\alpha_i \gg \alpha_{i+1}\,, \qquad\qquad l_{\perp i} \sim s_0\,, \tag{2.74}$$

In contrast to the DGLAP condition (2.45), the transverse momenta are not ordered but limited to the region around $s_0$ which does not increase with energy $\sqrt{s}$. The scale $s_0$ cannot be determined in the LLA(s). Strong ordering in $\alpha$'s leads to similar ordering in rapidity

$$y_i \gg y_{i+1}\,, \tag{2.75}$$

since $y_i - y_{i+1} \simeq \log(\alpha_i/\alpha_{i+1})$ in the collinear frame for the incident quarks.

- The *exchanged* gluons in the ladder in Fig. 2.7 are reggeized. This is a nontrivial property of nonabelian gauge theories, obtained in the LLA(s) as a result of summation of virtual corrections to the colour octet exchange in the high energy limit [26]. Gluon reggeization means that the standard propagator is replaced by

$$\frac{1}{t_i} \;\longrightarrow\; \frac{1}{t_i}\left(\frac{s_i}{s_0}\right)^{\omega(t_i)}\,, \tag{2.76}$$

where $t_i = k_i^2 \simeq -\mathbf{k}_{\perp i}^2$ and $s_i = (l_{i-1} + l_i)^2$. The function[10]

$$\omega(t) \;=\; \alpha_s N_c\, t \int \frac{d^2k'_\perp}{(2\pi)^2}\, \frac{1}{k'^2_\perp (k-k')^2_\perp} \tag{2.77}$$

[10] The integral is divergent and should be regularized, e.g. by introducing infrared cutoff $\mu$.

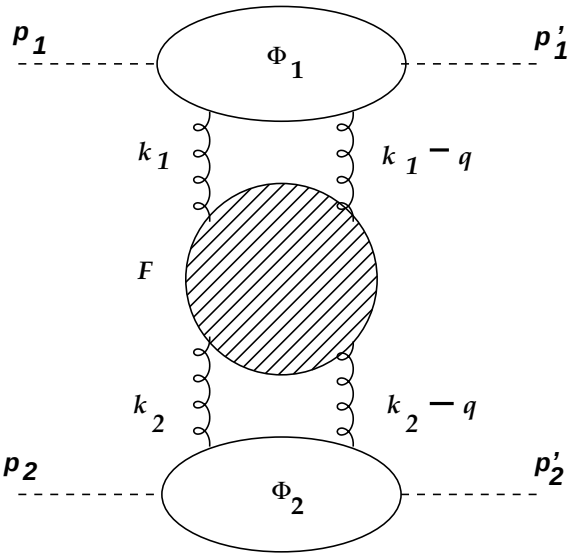


Figure 2.8: *The structure of the amplitude $A(\omega, t)$ in the high energy limit.*

defines the negative signature Regge trajectory of the reggeized gluon $\alpha(t) = 1 + \omega(t)$. Notice that the trajectory passes through 1 at $t = 0$, as expected for spin-1 gluon.

- There are two types of effective vertices. The gauge invariant reggeon-reggeon-particle vertex $\Gamma(k_i, k_{i+1})$, denoted by a blob in Fig. 2.7, replaces the standard triple gluon coupling. Its explicit form can be found e.g in [20]. The coupling of the $t$-channel gluons into the external quarks is given by the eikonal vertex

$$2\, p_{1,2}^{\mu}\, \delta_{\lambda\lambda'}\,, \tag{2.78}$$

where the colour structure has to be additionally supplied. The delta function reflects helicity conservation in the high energy limit. In the LLA(s), the momentum structure of eikonal vertex is also valid for gluons as external particles, which could illustrate our considerations.

## A. BFKL equation

Using the presented elements, the total cross section for the scattering of two quarks in the Regge limit is derived from (2.72)

$$\sigma^{tot} = \frac{Im_s A^{\mathbb{I}}(s,0)}{s}\,. \tag{2.79}$$

The reader may consult original articles [25] as well as excellent reviews [20, 27, 29] for details of the derivation. The final result looks as follows [20].

Let us introduce the Mellin transform of the $s$-channel discontinuity (2.72)

$$A(\omega, t) = \int_1^{\infty} d\left(\frac{s}{s_0}\right)\left(\frac{s}{s_0}\right)^{-\omega-1} \frac{Im_s A^{\mathbb{I}}(s,t)}{s}\,. \tag{2.80}$$

The structure of the amplitude $A(\omega,t)$ is shown in Fig. 2.8. It is a convolution of the impact factors $\Phi_i(\mathbf{k}_i,\mathbf{q})$ and the function $F(\omega,\mathbf{k}_1,\mathbf{k}_2,\mathbf{q})$ describing QCD pomeron exchange

$$A(\omega,t) \;=\; \frac{\mathcal{G}}{(2\pi)^4}\int \frac{d^2\mathbf{k}_1\; d^2\mathbf{k}_2}{\mathbf{k}_2^2\;(\mathbf{k}_1-\mathbf{q})^2}\;\Phi_1(\mathbf{k}_1,\mathbf{q})\;\Phi_2(\mathbf{k}_2,\mathbf{q})\;F(\omega,\mathbf{k}_1,\mathbf{k}_2,\mathbf{q})\,, \quad (2.81)$$

where $t=-\mathbf{q}^2$. For the quark-quark scattering, $\mathcal{G}=(N_c^2-1)/4N_c^2$ and the impact factors for slightly off-shell quarks to regulate infrared divergence are given by $\Phi_i=\alpha_s\;\delta_{\lambda\lambda'}$.

The function $F$ obeys the BFKL equation. In the forward limit $t=0$,

$$\omega F(\omega,\mathbf{k}_1,\mathbf{k}_2,0) \;=\; \delta^2(\mathbf{k}_1-\mathbf{k}_2)\;+\;\frac{\overline{\alpha}_s}{\pi}\int\frac{d^2\mathbf{k}'}{(\mathbf{k}_1-\mathbf{k}')^2} \quad (2.82)$$

$$\left[F(\omega,\mathbf{k}',\mathbf{k}_2,0)\;-\;\frac{\mathbf{k}_1^2}{\mathbf{k}'^2+(\mathbf{k}_1-\mathbf{k}')^2}F(\omega,\mathbf{k}_1,\mathbf{k}_2,0)\right]\,,$$

where $\overline{\alpha}_s=N_c\alpha_s/\pi$. The first term in the square brackets is related to real gluon emission while the second one corresponds to virtual corrections leading to reggeization of the exchanged gluons. Notice that the latter term cancels infrared divergence at $\mathbf{k}'=\mathbf{k}_1$ in the real emission part.

Relation (2.80) can be inverted using the inverse Mellin transform. After that the total cross section (2.79) reads

$$\sigma^{tot} \;=\; \frac{\mathcal{G}}{(2\pi)^4}\int\frac{d^2\mathbf{k}_1}{\mathbf{k}_1^2}\frac{d^2\mathbf{k}_2}{\mathbf{k}_2^2}\;\Phi_1(\mathbf{k}_1,0)\;\Phi_2(\mathbf{k}_2,0)\;\mathcal{F}(s,\mathbf{k}_1,\mathbf{k}_2,0)\,, \quad (2.83)$$

where $\mathcal{F}(s,\cdot)$ is the inverse Mellin transform of $F(\omega,\cdot)$ given by eq. (A.12) in Appendix A.

The energy dependence of $\sigma^{tot}$ is predicted by the solution of the BFKL equation. In Appendix A we present details of the computations leading to the following spherically symmetric solution

$$\mathcal{F}(s,k_1,k_2,0) \;=\; \frac{1}{\pi k_1^2}\;\int_C\frac{d\gamma}{2\pi i}\;\left(\frac{k_1^2}{k_2^2}\right)^{\gamma}\int_{C'}\frac{d\omega}{2\pi i}\;\left(\frac{s}{s_0}\right)^{\omega}\frac{1}{\omega-\overline{\alpha}_s\mathcal{K}(\gamma)}\,, \quad (2.84)$$

where the integration is done in the complex $\gamma$- and $\omega$-planes, related to the Mellin transformations in the variables $k_1^2$ and $s$, respectively. $\mathcal{K}(\gamma)$ is the Lipatov kernel, defined in Appendix A.

### B. Asymptotic form of the solution

The asymptotic form of solution of the BFKL equation for $s\to\infty$ is found after the saddle point integration around $\gamma=1/2$ at which point $\mathcal{K}'(1/2)=0$. In this case, the integration contour $C$ is given by: $\gamma=1/2+i\nu$. The singularity structure of the integrand in (2.84) is fully determined by its denominator, i.e. the equation

$$\omega \;=\; \overline{\alpha}_s\,\mathcal{K}(1/2+i\nu)\,. \quad (2.85)$$

$K(1/2+i\nu)$ is a real function, and when $\nu$ runs from $-\infty$ to $\infty$, $\omega$ goes from $-\infty$ to $\omega_0 = 4\overline{\alpha}_s \ln 2$ (for $\nu = 0$) and then back to $-\infty$. Thus we obtain a cut from $-\infty$ to $\omega_0$ in the complex $\omega$-plane. This should be contrasted with the situation which is usually assumed in Regge theory where we deal with poles in the complex angular momentum plane $l = \omega + 1$, see Section 2.4.1.

Now, the integration contour $C'$ in the $\omega$-plane is chosen to the right of the tip of the cut $\omega_0$, and is closed in the left half-plane encircling the cut singularity. The integral over $\omega$ in (2.84) is given in terms of the discontinuity of its integrand across the cut. After computing this discontinuity, we find

$$\mathcal{F}(s,k_1,k_2,0) \;=\; \frac{1}{\pi k_1^2}\;\int_{-\infty}^{\infty}\frac{d\nu}{2\pi}\;\left(\frac{k_1^2}{k_2^2}\right)^{1/2+i\nu}\left(\frac{s}{s_0}\right)^{\overline{\alpha}_s K(1/2+i\nu)}\;.$$

After expanding the integrand around the saddle point $\nu = 0$ and performing the $\nu$-integration, we find[11] the asymptotic solution

$$\mathcal{F}(s,k_1,k_2,0) \;=\; \frac{1}{\pi\sqrt{k_1^2 k_2^2}}\;\left(\frac{s}{s_0}\right)^{\overline{\alpha}_s K(1/2)}\;\frac{\exp\left\{\frac{-\ln^2(k_1^2/k_2^2)}{2\overline{\alpha}_s K''(1/2)\ln(s/s_0)}\right\}}{\sqrt{2\pi\overline{\alpha}_s K''(1/2)\ln(s/s_0)}}\,. \qquad (2.86)$$

The above formula has several interesting features.

1. Strong rise with energy $s$, determined by

$$\omega_0 \;=\; \overline{\alpha}_s K(1/2) \;=\; 4\overline{\alpha}_s \ln 2\,. \qquad (2.87)$$

   Substituting $\overline{\alpha}_s \approx 0.2$ we find: $\mathcal{F} \sim s^{\,0.5}$. Because of much stronger dependence on energy than for the soft pomeron, the presented vacuum quantum number exchange is termed *hard* (or BFKL) pomeron,

2. Diffusion pattern in $\ln(k_\perp)$ with a rate determined by the second derivative of the Lipatov kernel $\overline{\alpha}_s \mathcal{K}''(1/2) = 28\,\overline{\alpha}_s\,\zeta(3)$ and $\ln(s)$. The lack of strong ordering in gluon transverse momenta is the origin of diffusion.

The strong coupling constant is fixed in the leading $\log(s)$ summation. Its dependence on a hard scale is introduced in the next-to-leading approximation.

The strong rise of $\mathcal{F}$ is the source of problems. It leads to the same leading behaviour of the total cross section (2.83) in the high energy limit

$$\sigma^{tot} \;\sim\; s^{\,\alpha_{I\!P}-1} \;=\; s^{\,4\overline{\alpha}_s \ln 2}, \qquad (2.88)$$

which ultimately violates unitarity bound (2.68).

The lack of unitarity is related to the problem of diffusion into the nonperturbative region of small transverse momenta for large enough $s$, making the BFKL approach doubtful. One way to save this approach is to apply it only to the situation in which large scales of the same order in $k_\perp$ exist at the begining and at the end of the evolution. In this case diffusion into the low $k_\perp$-region

[11] With the help of the relation $\int_{-\infty}^{\infty} d\nu/2\pi\,\exp(-A\nu^2/2 + iB\nu) = \exp(-B^2/(2A))/\sqrt{2\pi A}$

is minimized. Solving the unitarity problem, however, allows to avoid small $k_\perp$ diffusion due to the existence of a saturation scale [28].

**C. NLO corrections to the BFKL equation**

The next-to-leading logarithmic approximation (NLLA) to the BFKL equation is found by the resummation of terms proportional to $\alpha_s(\alpha_s \log s)^n$ [29]. In this approximation the linear structure of the BFKL equation is retained. The BFKL integral kernel, however, obtains corrections proportional to $\alpha_s$.

The first source of the NLL corrections are virtual contributions to the reggeized gluon trajectory $\omega(t)$, eq. (2.77), and to the reggeon-reggeon-particle vertex $\Gamma$. The most important corrections come from the relaxation of the strong ordering condition (2.75) for the multi-Regge kinematics of the final state particles. In the NLLA, two final state gluons can be close to each other. In addition, a final state $q\bar{q}$ pair can also be emitted.

The first analysis of the next-to-leading order BFKL equation revealed that the found corrections are very large [30]. The value of the hard pomeron intercept, $\alpha_{I\!P} = 1 + \omega^{NLO}$, decreases significantly,

$$\omega^{NLO} \,=\, \omega_0 \,(1 \,-\, 6.47\,\overline{\alpha}_s)\,, \tag{2.89}$$

where $\omega_0$ is the leading order value (2.87). Therefore, for a reasonable value of $\overline{\alpha}_s \approx 0.2$ we have $\omega^{NLO} < 0$, and the intercept becomes smaller than 1. The cure of this problem is to additionally resum collinear corrections to the BFKL equation to all orders. In such a case the BFKL equation correctly reproduce the collinear limit, see [31] and references therein. At the same time, the value of $\omega^{NLO}$ is stable with respect to the change of $\alpha_s$, e.g. for $\alpha_s = 0.2$, $\omega^{NLO} = 0.27$ [31]. This value is significantly lower than the LO value. The unitarity bound, however, remains violated.

### 2.4.3 $k_\perp$-factorization

In the application of the BFKL approach to DIS at small $x$, the gluon ladder couples to the proton on one side and to the $q\bar{q}$ pair produced by the virtual photon on the other side, see Fig. 2.9. Thus, formula (2.83) takes the following form

$$\sigma_\lambda \,=\, \frac{\mathcal{G}}{(2\pi)^4} \int \frac{d^2\mathbf{k}_1}{\mathbf{k}_1^2} \frac{d^2\mathbf{k}_2}{\mathbf{k}_2^2}\; \Phi_\lambda(\mathbf{k}_1, 0)\; \Phi_p(\mathbf{k}_2, 0)\; \mathcal{F}(x, \mathbf{k}_1, \mathbf{k}_2, 0)\,, \tag{2.90}$$

where $\lambda = T, L$ denotes the virtual photon polarization and we replace $s$ by $x \simeq Q^2/s$ . $\Phi_\lambda$ and $\Phi_p$ are the virtual photon and proton impact factors, respectively. From gauge invariance, $\Phi_\lambda(\mathbf{k}_1 = 0, 0) = \Phi_p(\mathbf{k}_2 = 0, 0) = 0$, which are the necessary conditions for the infrared finiteness of the cross sections.

The photon impact factor is the high-energy hard cross section for the subprocess: $\gamma^* + g(k) \to q + \bar{q}$, computed in pQCD to the lowest order in $\alpha_s$ as a function of the transverse momentum $\mathbf{k}$ of the incoming *off-shell* gluon with $k \simeq xp + k_\perp$ and $k^2 = -\mathbf{k}^2$. The two relevant diagrams are are shown in Fig. 2.9. In the NLLA, the diagrams contain additional gluon in the final state

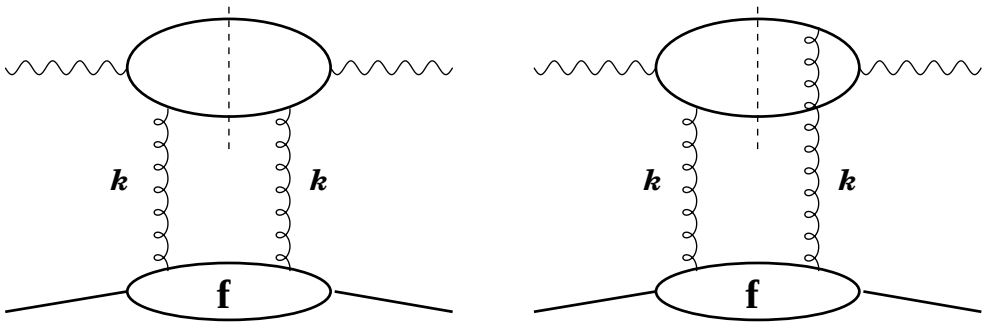


Figure 2.9: *The photon impact factor graphs.*

or they are modified by virtual corrections. The calculations of the photon impact factor in the NLLA are being pursued [32].

The proton impact factor is of a nonperturbative origin and can only be modelled. We rewrite relation (2.90) in a different way, by hiding the proton form factor in the *unintegrated gluon distribution*

$$f(x,\mathbf{k}) \;=\; \frac{1}{(2\pi)^3}\int \frac{d^2\mathbf{k}_2}{\mathbf{k}_2^2}\;\Phi_p(\mathbf{k}_2,0)\;\mathbf{k}^2\mathcal{F}(x,\mathbf{k},\mathbf{k}_2,0)\,. \tag{2.91}$$

In such a case eq. (2.90) becomes

$$\sigma_{T,L}(x,Q^2) \;=\; \int \frac{d^2\mathbf{k}}{\mathbf{k}^4}\;\Phi_{T,L}(Q^2,\mathbf{k})\;f(x,\mathbf{k})\,, \tag{2.92}$$

where we absorbed the factor $\mathcal{G}/(2\pi)$ in the definition of the photon impact factor $\Phi_{T,L}$ and indicated that it depends on the photon virtuality.

Relation (2.92) is called $k_\perp$*-factorization* formula [33]. In the small $x$ limit the DIS cross sections are computed by the convolution of the photon impact factors and unintegrated gluon distribution, done over all values of the gluon transverse momentum $\mathbf{k}^2$. This reflects the lack of the ordering in gluon transverse momenta in the BFKL ladder in contrast to the DGLAP approach. For large $Q^2$, in the leading twist approach, formula (2.92) resums leading in $\log(1/x)$ corrections to the splitting function $P_{gg}$ and next-to-leading corrections to the function $P_{qg}$ [34, 35, 72].

As discussed in the previous section, diffusion to the low $k_\perp$ region is a source of problems. There is the danger that in the application to the description of $F_2$ at small $x$, dominant contribution will come from the nonperturbative region. Extracting, however, the leading twist part for high $Q^2$, the nonperturbative part factorizes from the perturbative part, allowing for meaningful perturbative calculations in the spirit of collinear factorization [34, 35, 72, 20].

By considering the collinear limit in eq. (2.92), the following relation between the unintegrated gluon distribution and the gluon distribution $g(x,Q^2)$

from the DGLAP approach is found for large $Q^2$

$$xg(x,Q^2) \;=\; \int_0^{Q^2} \frac{dk^2}{k^2} f(x,k)\,, \tag{2.93}$$

where we assume spherical symmetry for $\mathbf{k}$. The derivation of this relation is presented in Section 3.2.6.

In the leading $\log(1/x)$ approximation, the unintegrated gluon distribution $f(x,k)$ obeys the BFKL equation which can easily be found from eq. (2.82) after the angular integration (see Appendix A for details)

$$\omega \bar{f}(\omega,k) = \bar{f}_0(k) + \overline{\alpha}_s \int_0^\infty \frac{dk'^2}{k'^2} k^2 \left\{ \frac{\bar{f}(\omega,k') - \bar{f}(\omega,k)}{|k'^2 - k^2|} + \frac{\bar{f}(\omega,k)}{\sqrt{4k'^4 + k^4}} \right\}, \tag{2.94}$$

where the relation between the $x$-space representation and the Mellin moments is given by

$$f(x,k) \;=\; \int_C \frac{d\omega}{2\pi i}\, x^{-\omega}\, \bar{f}(\omega,k)\,. \tag{2.95}$$

The nonhomogeneous term $f_0(k)$ corresponds to the exchange of two perturbative gluons between the $q\bar{q}$ pair and the proton. The higher order corrections to this process, described by the second term, lead to the BFKL gluon ladder. In the $x$-space, the BFKL equation takes the form of the evolution equation in the rapidity $Y = \log(1/x)$.

The calculations of the photon impact factor can be found in [25] or [20]. They are organized in such a way that only the leading order contribution (the $q\bar{q}$ pair Fock component) to the photon impact factor is considered. The higher order corrections are included in the unintegrated gluon distribution. In an alternative way of calculations, performed in [36, 37, 38] in the dipole representation, the BFKL effects are located in the photon wave function. The parent $q\bar{q}$ pair is dressed in the soft gluon contribution, and the interaction with the proton is realized by the exchange of two perturbative gluons. The explicit form of the photon impact factor can be read off from formulae (3.1) and (3.4), presented in Section 3.1.

Following the presented method of constructing the solution of the BFKL equation (2.94), we find the strong increase of the proton structure functions when $x \to 0$,

$$F_2(x,Q^2) \;\sim\; x^{-4\overline{\alpha}_s \ln 2}\,. \tag{2.96}$$

Thus, unitarization corrections are necessary which would tame the rise in $x$. It is not clear whether an analogue of the Froissard-Martin bound (2.68) exists for the $\gamma^* p$ scattering,

$$F_2 \;\le\; c\,\log^2(1/x)\,. \tag{2.97}$$

Although this condition has not been proven a logarithmic bound in $x$ is widely expected.

In order to fulfil unitarity in the description of DIS different methods have been proposed. The literature on this subject was initiated by the seminal work of Gribov, Levin and Ryskin (GLR) [39] and continued over the years in [40]-[64]. The overall picture which emerges from these studies is related to saturation in dense partonic systems.

### 2.4.4 Parton saturation

In the DGLAP approach in the double leading logarithmic approximation (DLLA), when $x \to 0$ and $Q^2 \to \infty$, the number of gluons strongly rises [65],

$$xg(x,Q^2) \sim \exp 2\sqrt{\overline{\alpha}_s \log(Q^2/Q_0^2)\log(1/x)}\,, \tag{2.98}$$

where the fixed coupling constant $\overline{\alpha}_s = N_c\alpha_s/\pi$ is assumed for simplicity. This follows from the singular behavior of the splitting function $P_{gg}(z) \approx 2N_c/z$ which dominates in the evolution equation for the gluon distribution at small $x$. The solution (2.98) corresponds to a flat input distribution. For a singular input, $xg \sim x^{-\lambda}$, the power-like rise in $x$ is conserved by the evolution in $Q^2$. Through the coupling to the sea quarks, $g \to q\bar{q}$, the strong rise of the gluon distribution leads to a similar behaviour of the proton structure function $F_2$. As we have seen in the previous section, the same result is obtained in the leading- and next-to-leading BFKL approach.

The gluon distribution increase cannot continue indefinitely with decreasing $x$. If the density of gluons becomes too large anihilation or recombination of gluons become important, taming the strong increase. This effect is called *parton saturation*. A simple geometric estimation shows when these effects may become significant [40]. In a frame in which the proton momentum is large, $xg(x,Q^2)$ gives the number of gluons per unit of rapidity of transverse size of the order of $1/Q$. The transverse area occupied by gluons is given by the gluon-gluon cross section $\sigma_{gg} \sim \alpha_s(Q^2)/Q^2$ times the number of gluons. If this area is comparable to transverse proton size,

$$\frac{\alpha_s(Q^2)}{Q^2}\, xg(x,Q^2) \sim \pi R^2\,, \tag{2.99}$$

the gluons in the proton overlap and recombination occurs [39].

Condition (2.99) defines *critical line* (or better transition region) in the $(x,Q^2)$-plane where parton saturation is important, see Fig. 2.10. With this line, the saturation scale $Q_s(x)$ is also defined. The saturation scale increases with decreasing $x$, thus we expect that for small enough $x$, the region around the critical line corresponds to *semi-hard* QCD when $\alpha_s$ is small and the partonic system is dense. Below the critical line the linear evolution equations hold, above this line recombination effects cannot be neglected and the evolution equations obtain non-linear modifications, called *shadowing* or *screening* corrections. Much above the critical line the approach based on pQCD breaks down. Thus, with decreasing $x$ and fixed $Q^2$, the following transition is studied:

*perturbative QCD* $\longrightarrow$ *high density QCD* $\longrightarrow$ *nonperturbative QCD*

Gribov, Levin and Ryskin found the following approximate modification of the DGLAP evolution equation for the gluon distribution in the DLLA [39],

$$\frac{\partial^2\, xg(x,Q^2)}{\partial \ln(1/x)\,\partial \ln(Q^2/\Lambda^2)} = \overline{\alpha}_s\, xg(x,Q^2) - \frac{\alpha_s^2}{R^2Q^2}\left[xg(x,Q^2)\right]^2\,. \tag{2.100}$$

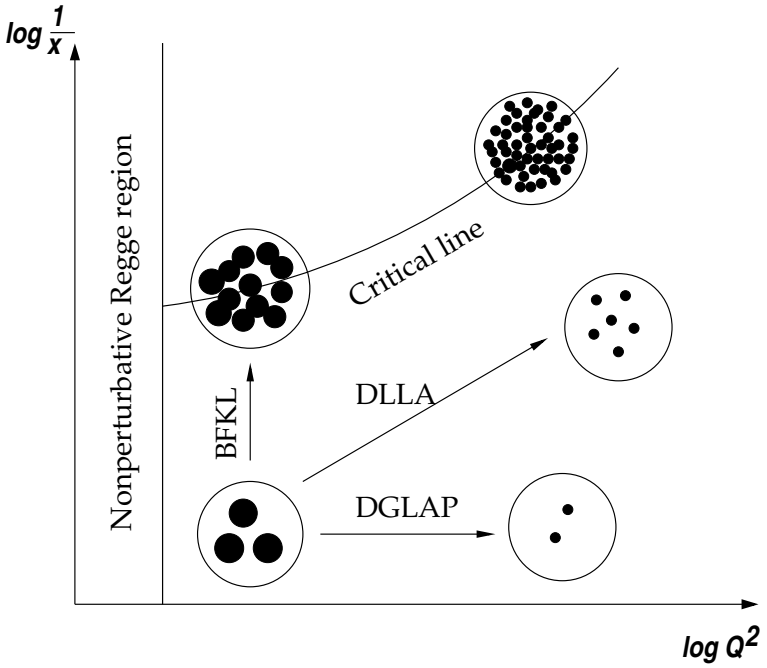


Figure 2.10: *Parton distributions and critical line .*

Notice the factor $1/Q^2$ which in general suppresses the nonlinear term. The nonlinearity, however, becomes important close to the critical line where the ratio between the nonlinear and linear terms is of the order of $\alpha_s$. With such a modification, the gluon distribution saturates with decreasing $x$, and so does the structure function. A more refined analysis of Mueller and Qiu [40] extends the GLR result by including nonlinear modifications for the DGLAP equations for the sea quark distributions.

The GLR equation effectively resums 'fan' diagrams where one gluon ladder, corresponding to QCD pomeron in the DLLA, splits into two gluon ladders. The nonlinear term in (2.100) describes the basic one-to-two ladder splitting. In fact, the nonlinear term contains the two-gluon distribution $G^{(2)}$, approximated by the square of the gluon distribution [40]

$$G^{(2)}(x, x, Q^2, Q^2) \;=\; \frac{1}{\pi R^2}\left[xg(x, Q^2)\right]^2 , \tag{2.101}$$

where $R$ is related to the correlation length between gluons from different ladders. If the two ladders couple to different quarks, the proton size is relevant, and $R \approx 5$ GeV$^{-1}$. If the ladders couple to the same quark, the constituent quark radius $R \approx 2$ GeV$^{-1}$ is more appropriate [43]. In this case, the strength of the nonlinear term in eq. (2.100) is significantly bigger.

The GLR equation generated a lot of interest [40]-[53]. Phenomenological studies were concentrated on estimation of the numerical significance of the nonlinear corrections [41, 42, 45], especially for the DIS experiments at HERA [43, 44, 47]. The analysis performed with the help of the nonlinear evolution equations of Mueller and Qiu showed that the effect of nonlinearity may be

hidden in the initial distributions for the linear DGLAP evolution equations, at least for not too small $Q^2$ ($\geq 2$ GeV$^2$) [49]. On the theoretical side, the study of the four-gluon operator revealed that the evolution of the four gluon state in the DLLA is not simply the product of two independent gluon ladders, but proceeds through the pairwise interactions of all four gluon lines [52]. The effect is not large but in order to estimate to what extent the GLR equation is a good approximation, more complicated $n$-gluon operators should be analyzed [50, 51]. The corresponding equations for them form the so-called BKP hierarchy.

A systematic program to study such operators beyond the DLLA, with the aim to find unitary description of DIS, was formulated by Bartels in [50] and developed in [52, 53]. The idea is to identify and resum a minimal set of nonleading corrections to the leading BFKL summation which leads to a unitary amplitude. This set comprises contributions with $n$ gluons in the $t$-channel and in order to fulfil unitarity conditions in all subchannels any $n$ is allowed. The program was pursued up to $n = 6$. An interesting pattern, based on gluon reggeization and conformal symmetry, was revealed which gives hope that the whole set of unitarity corrections to the BFKL equation could be formulated as an effective conformal field theory in 2+1 dimensions [53]. Lipatov with his collaborators were also trying to construct an effective field theory for high energy QCD [54]. Independently, the problem of unitarization was studied in the dipole picture of Mueller in [56, 57] and in [58]. A similar approach was presented by Levin with coworkers [59]. Unitarization has also been studied using renormalization group methods [60].

A different approach to unitary generalization of the BFKL equation was proposed by Balitsky [61]. By using the operator product expansion for high energy scattering in QCD, he derived an infinite set (hierarchy) of coupled equations for $n$-point Wilson-line operators. Recently, Weigert managed to simplify the form of these equations by writing them as a functional evolution equation for the generating functional of the Wilson-line operators [62]. The connection between the effective theory for the Colour Glass Condensate [63] and the evolution equation found by Weigert has been established in [64].

The Balitsky's equations decouple in the large $N_c$ limit. In this limit, the equation for the 2-point function was independently derived by Kovchegov [66] in the dipole picture. The equation generalizes the BFKL equation by including a quadratic term, and reduces to the GLR equation in the DLA. The properties of this equation were investigated in [66, 66, 68], supporting the picture of parton saturation. The equation introduces an internal saturation scale $Q_s(x)$ below which the nonlinear effects lead to saturation of the gluon density.

The current status of the theoretical investigations of unitarization suggests further studies in order to obtain results which could be directly applied to the description of high energy DIS. In Chapter 3 we describe a semi-phenomenological approach to unitarization where we propose an effective parameterization of the DIS interactions containing essential features of parton saturation, in particular the saturation scale. As the main result of this analysis, the idea of saturation turned out to be very successful in the description of the data from HERA.

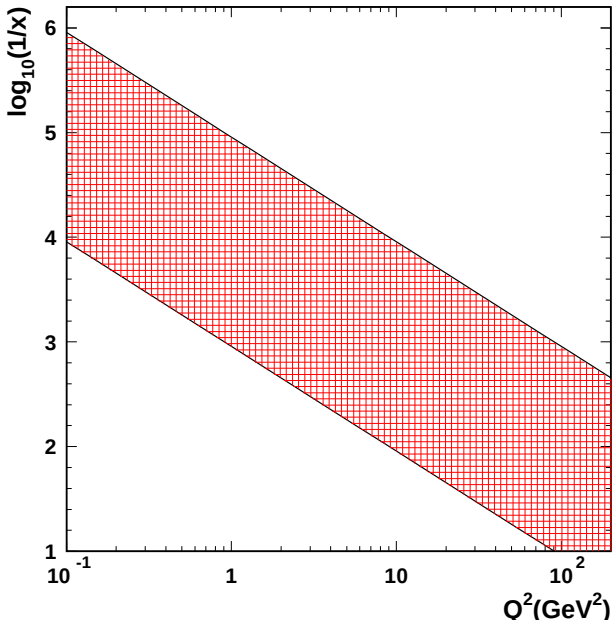


Figure 2.11: *Acceptance region at HERA. Additional constraint comes from the angular cut on measured scattered electron. The maximal* $Q^2 \simeq 10^5$ GeV$^2$.

### 2.4.5 Small $x$ limit at HERA

An excellent review of experimental results obtained at HERA is presented in [69]. Here we briefly describe the small $x$ results. At this collider, 27 GeV electrons are brought into collision with 820 GeV protons. Due to the large center-of-mass energy $\sqrt{s} \approx 300$ GeV, the range in the Bjorken variable $x$ is extended by three orders of magnitude from $10^{-2}$ for fixed target experiments down to $10^{-5}$ at HERA (for $Q^2 = 1$ GeV$^2$). A part of the kinematic range of HERA in the $(x, Q^2)$-plane is shown in Fig. 2.11.

The general situation concerning the applicability of pQCD techniques to the description of DIS processes is shown in Fig. 2.10. The DGLAP equations evolve a known proton structure at a scale $Q_0^2$ up to a large $Q^2$ at moderate values of $x$ by the summation of strongly ordered in $k_T$ parton emissions. At small $x$ and moderate $Q^2$, the BFKL equation evolves to smaller values of $x$, summing strongly ordered in rapidity gluon emissions. The two equations have a common limit (DLLA) at high $Q^2$ and small $x$. At very small $x$, saturation effects come into the game, restoring unitarity through nonlinear evolution equations (e.g. the GLR equation). From this perspective, the main problem at HERA is how to locate the general scheme from Fig. 2.10 in Fig. 2.11. In particular, the following questions have been addressed.

1. For how low $x$ is the DGLAP summation still a viable approximation?

2. Are the values of $x$ small enough for the BFKL approach to be applied?

3. Has the region of parton saturation already been reached?

These problems are intimately connected to the interplay between perturbative and nonperturbative aspects of QCD. Thus, the studies at HERA are not simple tests of perturbative QCD but, by pushing perturbative techniques to the limit of applicability, they extend our knowledge about nonperturbative structure of the proton and eventually about confinement.

### A. BFKL searches

In comparison to the fixed target experiments, the first most striking result at HERA is the strong rise of the proton structure function $F_2 \sim x^{-\lambda(Q^2)}$ with decreasing $x < 10^{-2}$ at fixed $Q^2$, see Fig. 3.6. The measured values of $\lambda$ are much bigger than for the soft pomeron exchange [70]. The strong rise in $x$ is predicted by the BFKL summation, and the question arises if the observed behaviour is a genuine signature of this approach. The analyses based on the BFKL equation and $k_\perp$-factorization are successful in the explanation of $F_2$ [71]. A particular attention in these analyses was paid to the infrared region of small transverse momenta since the integration in (2.92) is carried over all values of $l$. In the most elaborate analysis [72], a unified description is constructed which incorporates both the BFKL and DGLAP resummations and takes into account a significant part of the next-to-leading corrections to the BFKL equation. Other unified approaches like CCFM scheme [73], which includes coherence effects in gluon emission, were also extensively studied [74].

However, the standard method based on the fit of initial distributions for the DGLAP evolution equations is also successful in the description of $F_2$. The reason is explained by the strong rise of the gluon distribution in the DLLA, see eq. (2.98), which induces a similar behaviour of $F_2$. Based on the double-logarithmic asymptotics, a scaling low for $F_2$ was proposed [75]. The relation between the BFKL and DGLAP approaches was extensively studied in [76]. The practical conclusion drawn from these studies was that in the kinematic range of HERA, the inclusive measurement of $F_2$ is not able to discriminate between the two approaches. For this purpose, exclusive processes which directly probe the kinematic structure of gluon emission would be more appropriate.

The processes that have been suggested are shown in Fig. 2.12. In the forward jet production in DIS at small $x$ [77], see Fig. 2.12(a), the jet transverse momentum $k_{Tj}^2 \approx Q^2$ in order to minimize the DGLAP evolution and the BFKL diffusion into the region of small transverse momenta of the gluons in the ladder. The longitudinal momentum of the jet $x_j \gg x$ to enhance the role of the BFKL summation and isolate the $(x/x_j)^{-\lambda}$ behaviour. In such kinematics the jet is produced close to the proton remnants making the measurement a challenge. The measurement was performed, however, and the experimental results favour the descriptions with non-ordered in $k_T$ gluon emissions [78, 79].

A hadronic variant of this process is shown in Fig. 2.12(c) where two hard jets in hadron-hadron collision are strongly separated in rapidity. If the BFKL mechanism populating the rapidity interval $\Delta y$ with no ordered in $k_T$ gluons is used, the cross section is proportional to $\exp(\lambda \Delta y)$ [80]. This idea is not feasible, however, at fixed energy colliders. Instead, it is better to look at the angular correlation of the dijets which at leading (fixed) order are back-to-

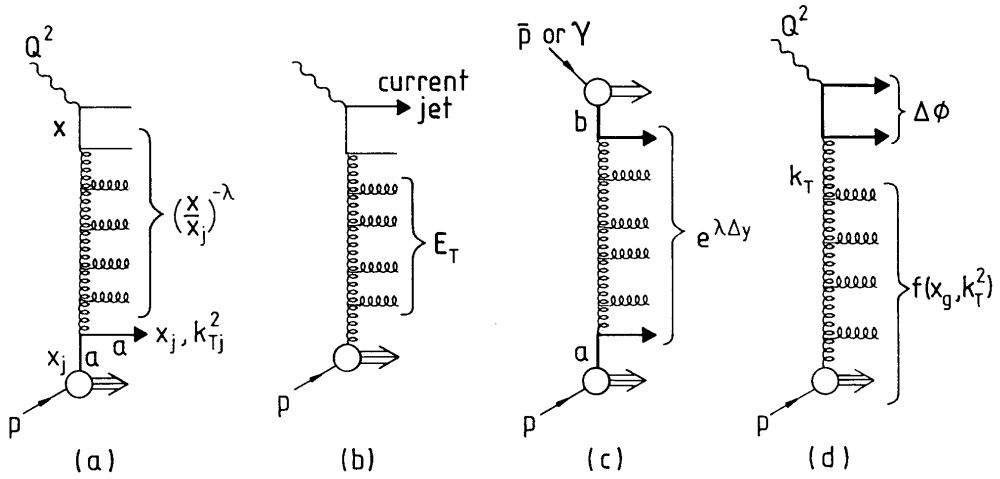


Figure 2.12: *BFKL footprints*

back, but gluon radiation introduces decorrelation [81]. In DIS a similar effect is observed in the process shown in Fig. 2.12(d) [82]. The first experimental results were reported in [83].

Due to the relaxation of strong ordering of the gluon $k_T$'s in the BFKL approach, more transverse energy $E_T$ should be emitted between the current jet and the proton remnants than would result from the DGLAP approach [84], especially in the central and forward region, see Fig. 2.12(b). Such an effect was indeed observed at HERA [78, 85]. The comparison of the predictions with the data, however, is plagued by hadronization effects. The BFKL-based calculation [84] accounts for $E_T$ at the partonic level, assuming an additional constant contribution due to hadronization. Other models, formulated with the help of Monte Carlo techniques, include hadronization and after some fine-tunning are able to describe the observed $E_T$.

In conclusion, although none of these processes can be treated as proof of BFKL effects, the measurements show that higher order QCD effects represented by BFKL (or CCFM) configuration for gluon emission are important in the data description.

## B. DIS diffraction

Kinematically, small $x$ opens the possibility to observe DIS events with large rapidity gap in the final state between the photon and the proton fragmentation regions. In fact, in most cases the scattered proton stays intact losing only a small fraction of its initial energy, see Fig. 2.13. In the pQCD approach based on DGLAP emissions, the probability of such processes are exponentially suppressed due to the fragmentation process driven by parton radiation. However, the observed fraction of these events in DIS at HERA is of the order of 10%, with the distribution fairly independent of $Q^2$ and $x$ [86, 87]. This is a second striking result in the small $x$ region at HERA. Large rapidity gap is a characteristic feature of diffractive processes in which the pomeron exchange is

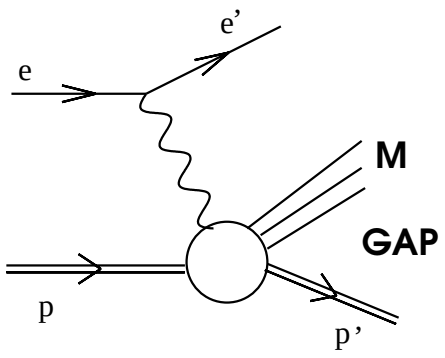


Figure 2.13: *DIS diffraction.*

responsible for the scattered proton being intact. With this interpretation, the natural question is whether the BFKL pomeron is responsible for DIS diffraction.

The most compelling picture of diffraction is obtained in the proton rest frame. In this frame, the virtual photon dissociates into a $q\bar{q}$ pair long before the interaction with the proton. Then the pair is elastically scattered forming diffractive system[12] with the invariant mass $M$. The configurations which dominate diffractive cross section are the ones with *large* (hadronic) transverse sizes of the $q\bar{q}$ pair (aligned jet configuration). *Small* (perturbative) transverse sizes, giving e.g. diffractively produced large $p_T$ jets, are not precluded but are suppressed as higher twist. A significant part of the dominant contribution is given by *intermediate* (semi-hard) sizes. This region of the transverse sizes is bound to effects which are at the border between perturbative and nonperturbative phases of QCD. In particular, by suppressing pure perturbative component, DIS diffraction is especially sensitive to parton saturation since a large part of unitarization corrections contributes to diffractive dissociation. Of course, by studying exclusive diffractive processes like high-$p_T$ jet or $J/\psi$ vector meson production, one can isolate the perturbative component, and suppress semi-hard and large configurations. In this case a single BFKL pomeron exchange would dominate.

The presented picture is confirmed in the studies of diffractive dissociation based on the BFKL approach [88]. In inclusive diffractive DIS almost the whole phase space covered by the BFKL evolution is located in the infrared domain of transverse gluon momenta where pQCD is not applicable. This finding confirms the dominance of aligned jet configuration. However, in the diffractive $J/\psi$ production at large $t$, where small size component dominates, the BFKL pomeron provides a good description [89].

The observed features of DIS diffraction are intimately related to the problem of unitarization corrections (with the intuitive picture of parton saturation). In the following presentation we explore this problem in detail. The main idea behind the presentation is that unitarization effects are already important in

[12]The system can be generalized to $q\bar{q} + n$ gluon final state.

the HERA kinematic range. In particular, we suggest that the transition region or critical line from Fig. 2.10 is located at $Q_s^2 = 1 - 2$ GeV$^2$ and $x \sim 10^{-4}$. Thus for inclusive DIS, saturation effects manifest themselves in the transition of $F_2$ to low $Q^2$ values. Since $Q_s$ is in the perturbative region, the onset of saturation can be described by means of perturbative QCD. In Chapter 3 we present details of the unitary description of inclusive DIS at small $x$.

In diffractive DIS, saturation is crucial even for higher values of $Q^2$, due to suppression of the perturbative component. The constant ratio of the DIS cross sections $\sigma_{diff}/\sigma_{tot}$ as a function of $x$ and $Q^2$ is a direct manifestation of this effect. Using the parameterization of the $\gamma^* p$ interactions found in the inclusive data analysis, we obtain a good description of diffractive data. This and related issues on DIS diffraction are discussed in Chapter 4.

# Chapter 3

# Inclusive DIS at small $x$

In this chapter we present the description of inclusive deep inelastic scattering at small $x$, based on the analysis [94]. We start from presenting the $k_T$-factorization formulae for the $\gamma^* p$ cross sections (2.92). We switch then to the dipole representation in which a simple physical interpretation of the scattering exists in the proton rest frame. In this interpretation, the virtual photon splits into a $q\bar{q}$ dipole long before the interaction with the proton takes place. The dipole-proton interaction is parameterized in the way which leads to unitarity by using the idea of parton saturation. In particular, an internal scale related to a dense partonic system in the proton is introduced. We discuss qualitatively the results of such a model of the interaction, emphasizing the transition to low $Q^2$ region of DIS. The other aspects like the photoproduction limit and heavy quark production are also analyzed. The presented model predicts a new scaling of the $\gamma^* p$ cross sections at low values of $x$, confirmed by the analysis of the existing data [98]. More formal aspects of the description are discussed in the section on the twist expansion. This problem could be studied in more detail, and interesting results on the cancellation of the transverse and longitudinal twist-4 components of the proton structure function $F_2$ are presented, following [94, 99]. We finish with the discussion of the relation between the dipole formulation and the conventional DGLAP description.

## 3.1 Small $x$ cross sections

The cross section for the $\gamma^* p$ scattering from transverse and longitudinal polarized photons are computed from the imaginary part of the forward Compton scattering amplitude in the high energy limit, see Fig. 2.9 with $\mathbf{k}$ replaced by $\mathbf{l}$. The virtual photon splits into a quark-antiquark pair that interacts elastically with the proton through the exchange of two gluons in the colour singlet state. This interaction is described by the unintegrated gluon distribution $f(x, l^2)$, which introduces the dependence on energy of the $\gamma^* p$ system. Strictly speaking, if only two perturbative gluons are exchanged which directly couple to quarks in the proton, the process is energy independent and $f(x, l^2) = f_0(l^2)$. If two reggeized gluons interact with themselves, forming the compound system (hard pomeron), $f(x, l^2)$ is a solution of the BFKL equation (2.94). The

interaction can also involve many gluon exchanges, like in the semiclassical approximation [91] in which the basic $k_\perp$-factorization structure (2.92) is retained.

For the transverse photons we have [90]

$$\sigma_T = \frac{\alpha_{em}}{\pi} \sum_f e_f^2 \int \frac{d^2\mathbf{l}}{l^4}\, \alpha_s f(x,l^2) \int d^2\mathbf{k} \int_0^1 dz$$
$$\left\{ [z^2 + (1-z)^2] \left\{ \frac{\mathbf{k}}{D(\mathbf{k})} - \frac{\mathbf{k}+\mathbf{l}}{D(\mathbf{k}+\mathbf{l})} \right\}^2 + m_f^2 \left\{ \frac{1}{D(\mathbf{k})} - \frac{1}{D(\mathbf{k}+\mathbf{l})} \right\}^2 \right\}, \quad (3.1)$$

where $m_f$ is a mass of the quark of flavour $f$ to which the virtual photon couples,

$$D(\mathbf{k}) = \mathbf{k}^2 + \overline{Q}^2 \quad (3.2)$$

and

$$\overline{Q}^2 = z(1-z)Q^2 + m_f^2 . \quad (3.3)$$

In the $\gamma^* p$ collinear frame, $\pm\mathbf{k}$ are two-dimensional vectors of transverse momentum of the quarks and $z, (1-z)$ are the fractions of the light-cone momentum of the photon carried by the quarks. The transverse momentum of the exchanged gluon $\mathbf{l}$ determines its virtuality, $l^2 = -\mathbf{l}^2$.

The cross section for longitudinally polarized virtual photon takes the form

$$\sigma_L = \frac{\alpha_{em}}{\pi} \sum_f e_f^2 \int \frac{d^2\mathbf{l}}{l^4}\, \alpha_s f(x,l^2) \int d^2\mathbf{k} \int_0^1 dz$$
$$4\, Q^2 z^2 (1-z)^2 \left\{ \frac{1}{D(\mathbf{k})} - \frac{1}{D(\mathbf{k}+\mathbf{l})} \right\}^2 . \quad (3.4)$$

The relation between the structure functions $F_{T,L}$ and $\sigma_{T,L}$ is given by eq. (2.10).

The photon impact factors, introduced in Section 2.4.3, can be found by comparison of the above expressions with eq. (2.90) where $\mathbf{k}$ is replaced by $\mathbf{l}$. The colour neutrality enforces the conditions $\Phi_{T,L}(Q^2, \mathbf{l}=0) = 0$, important for the infrared finiteness of the cross sections.

In the following we present an effective parameterization of the interactions between the $q\bar{q}$ pair and the proton, leading to unitary cross sections. The parameterization contains essential features of parton saturation. The discussion will be presented in a dipole representation which is particularly suitable for a discussion of unitarity issues.

### 3.1.1 Dipole representation

The dipole representation of the inclusive cross sections is obtained after substitution relations (B.1) and (B.3) from Appendix B into (3.1) and (3.4), and integration over $\mathbf{k}$. In this representation the transverse quark momentum $\mathbf{k}$ is traded for the Fourier conjugate variable, the $q\bar{q}$ transverse separation $\mathbf{r}$. The crucial element of the calculation is the observation that the $\mathbf{k}$-integration gives the delta function $\delta^2(\mathbf{r}_1 - \mathbf{r}_2)$ which allows to perform one of the two integrations over $\mathbf{r}_{1,2}$ .

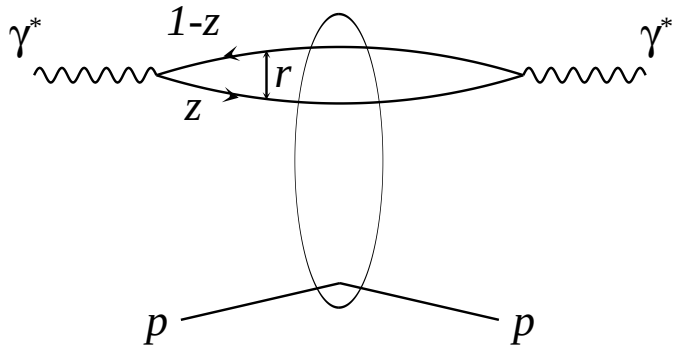


Figure 3.1: *Schematic representation of the basic factorization in inclusive DIS at small $x$.*

We obtain for the transverse cross section

$$\sigma_T = \frac{\alpha_{em}}{\pi} \sum_f e_f^2 \int d^2\mathbf{r} \int_0^1 dz \left\{ [z^2 + (1-z)^2] \, \overline{Q}^2 K_1^2(\overline{Q}r) + m_f^2 K_0^2(\overline{Q}r) \right\}$$
$$\times \int \frac{d^2\mathbf{l}}{l^4} \, \alpha_s f(x, l^2) \, (1 - e^{-i\mathbf{l}\cdot\mathbf{r}}) \, (1 - e^{i\mathbf{l}\cdot\mathbf{r}}) \,, \tag{3.5}$$

and similarly for the longitudinal cross section

$$\sigma_L = \frac{\alpha_{em}}{\pi} \sum_f e_f^2 \int d^2\mathbf{r} \int_0^1 dz \; 4 \; Q^2 \; z^2(1-z)^2 \; K_0^2(\overline{Q}r)$$
$$\times \int \frac{d^2\mathbf{l}}{l^4} \, \alpha_s f(x, l^2) \, (1 - e^{-i\mathbf{l}\cdot\mathbf{r}}) \, (1 - e^{i\mathbf{l}\cdot\mathbf{r}}) \,, \tag{3.6}$$

were $K_{0,1}$ are the Bessel–Mc Donald functions. Both cross sections can be written in the following compact form [90, 36], shown schematically in Fig. 3.1,

$$\sigma_{T,L}(x, Q^2) = \int d^2\mathbf{r} \int_0^1 dz \; \sum_f \; |\Psi_{T,L}^f(\mathbf{r}, z, Q^2)|^2 \; \hat{\sigma}(x, \mathbf{r}) \,. \tag{3.7}$$

where the *photon wave functions* $\Psi_{T,L}^f$ describe the splitting of the virtual photon into the $q\bar{q}$ pair [92],

$$|\Psi_T^f(\mathbf{r}, z, Q^2)|^2 = \frac{3\,\alpha_{em}}{2\pi^2} \; e_f^2 \left\{ [z^2 + (1-z)^2] \; \overline{Q}^2 \; K_1^2(\overline{Q}r) + m_f^2 K_0^2(\overline{Q}r) \right\}, \tag{3.8}$$

$$|\Psi_L^f(\mathbf{r}, z, Q^2)|^2 = \frac{3\,\alpha_{em}}{2\pi^2} \; e_f^2 \left\{ 4 \; Q^2 z^2 (1-z)^2 K_0^2(\overline{Q}r) \right\}, \tag{3.9}$$

and $\overline{Q}$ is defined in eq. (3.3). Formula (3.7) forms the basis of the following analysis.

The *dipole cross* $\hat{\sigma}(x, \mathbf{r})$ in eq. (3.7) characterizes the interaction of the $q\bar{q}$ pair with the proton, and is connected to the unintegrated gluon distribution $f(x, l^2)$,

$$\begin{aligned} \hat{\sigma}(x, \mathbf{r}) &= \frac{2\pi}{3} \int \frac{d^2\mathbf{l}}{l^4}\, \alpha_s f(x, l^2)\, (1 - e^{-i\mathbf{l}\cdot\mathbf{r}})\, (1 - e^{i\mathbf{l}\cdot\mathbf{r}}) \\ &= \frac{4\pi^2}{3} \int_0^\infty \frac{dl^2}{l^4}\, \alpha_s f(x, l^2)\, (1 - J_0(lr))\,. \end{aligned} \tag{3.10}$$

where in the last equation the angular integration was performed and $J_0$ is the Bessel function. The two terms in brackets in (3.10) are related to the way the two exchanged gluons couple to the quarks. 1 comes from the diagrams with the gluons coupled to the same quark while the exponents $\exp(\pm i\mathbf{l}\cdot\mathbf{r})$ are given by the coupling to different quarks, see Fig. 2.9. Notice that due to this structure the dipole cross section vanishes for $r \to 0$. This phenomenon, called *colour transparency*, is a characteristic feature of perturbative QCD.

Formula (3.7) reflects the $k_\perp$-factorization theorem. The physical interpretation of this theorem is provided in the proton rest frame. The formation time (called Ioffe time [93]) of the $q\bar{q}$ pair is related to the uncertainty of energy of the pair, $\tau_{q\bar{q}} \sim 1/\Delta E$. In the small-$x$ limit $\Delta E \approx xM_P$ in the proton rest frame, see e.g. [20]. Thus the formation time $\tau_{q\bar{q}}$ is much larger than the interaction time of the pair with the proton, $\tau_{int} \sim 1/M_P$,

$$\tau_{q\bar{q}} \gg \tau_{int}\,. \tag{3.11}$$

In summary, for a small enough $x$, the $q\bar{q}$ pair is formed far upstream of the proton. This process is described by the photon wave function $\Psi(\mathbf{r}, z)$. Then, the pair scatters off the proton with the characteristics $(\mathbf{r}, z)$ frozen over the time of the interaction. Consequently, $\hat{\sigma}(x, r)$ can be interpreted as the cross section for a scattering of a $q\bar{q}$ pair with transverse size $r$ off the proton.

### 3.1.2 Approximate relations

The dipole representation (3.7) is particularly suitable for a qualitative analysis since the physical interpretation is transparent in this representation. In this section we derive approximate relations which allow to perform such an analysis. For simplicity we set $m_f = 0$.

We start from the cross section (3.7) for transversely polarized photons

$$\sigma_T \sim \int_0^\infty dr^2 \int_0^1 dz\, [z^2 + (1-z)^2]\, z(1-z)Q^2\, K_1^2\Big(\sqrt{z(1-z)}Qr\Big)\, \hat{\sigma}(x, r)\,. \tag{3.12}$$

Its properties are determined by the behaviour of the Bessel function $K_1$:

$$K_1(x) = \begin{cases} 1/x & \text{for} \quad x \ll 1 \\ \sqrt{\pi/2x}\, \exp(-x) & \text{for} \quad x \gg 1\,. \end{cases} \tag{3.13}$$

Thus the main contribution to $\sigma_T$ comes from the arguments of $K_1$ smaller than 1,

$$\sigma_T \sim \int_0^\infty dr^2 \int_0^1 dz \, [z^2 + (1-z)^2] \, \frac{\hat{\sigma}(x,r)}{r^2} \, \Theta\left[z(1-z)\, Q^2 r^2 < 1\right] , \quad (3.14)$$

where the function $\Theta(x<1)$ equals 1, if $x<1$, or 0, otherwise.

If $0 \leq r \leq 2/Q$, the theta function does not impose any restriction on the values of $z$. In this case the $z$-integration factorizes and gives the factor $2/3$. For such a configuration the distribution of $z$ is rather uniform with the mean value $< z >= 1/2$. This is why we call this configuration *symmetric*.

A different configuration occurs for large transverse separations $r \gg 2/Q$. Now, the theta function heavily restricts $z$ to small values: $z < 1/(Q^2 r^2)$. The $z$-integration is performed before the $r$-integration, giving the leading result $2/(Q^2 r^2)$, where the factor 2 arises from the symmetry $z \leftrightarrow (1-z)$. In this configuration, called *aligned jet*, $z \approx 0$ or $(1-z) \approx 0$. Thus, one of the quarks follows the photon direction while the other stays with the proton. Notice that such a configuration occurs for large values of the transverse separation, probing nonperturbative region.

Summarizing, we obtain the following approximate form

$$\sigma_T \sim \underbrace{\int_0^{4/Q^2} \frac{dr^2}{r^2} \, \hat{\sigma}(x,r)}_{symmetric} + \underbrace{\int_{4/Q^2}^\infty \frac{dr^2}{r^2} \left(\frac{1}{Q^2 r^2}\right) \hat{\sigma}(x,r)}_{aligned\ jet} , \quad (3.15)$$

where we have neglected multiplicative numerical factors, unimportant for the qualitative analysis. For convenience, we have defined aligned jet configuration starting from $r = 2/Q$ when $z = 1/2$. Thus, we should have in mind that the aligned jet integral also contains an intermediate region of $r$. Notice the factor $1/Q^2 r^2$ which suppresses the integrand for $r \gg 1/Q$. Its significance will be discussed in detail in the following chapters.

A similar analysis[1] performed for the longitudinal cross section gives

$$\sigma_L \sim \underbrace{\int_0^{4/Q^2} dr^2 \; Q^2 \; \hat{\sigma}(x,r)}_{symmetric} + \underbrace{\int_{4/Q^2}^\infty dr^2 \; Q^2 \left(\frac{1}{Q^2 r^2}\right)^3 \hat{\sigma}(x,r)}_{aligned\ jet} . \quad (3.16)$$

In order to find the leading $Q^2$ behaviour of the above formulae we have to provide a form of the dipole cross section. We do this in the next section specifying a model which takes into account unitarity requirements.

## 3.2 Saturation model

The saturation model was formulated and compared at length to DIS data in [94]. Here we describe this model, discussing some details which were not presented in the original formulation. For related approaches see [96].

[1] The behaviour $K_0(x) \approx \log(1/x)$ for $x \ll 1$ is important in this case.

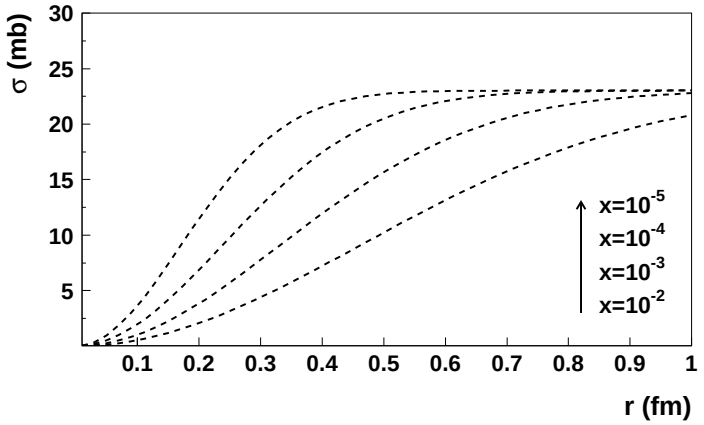


Figure 3.2: *Dipole cross section for different values of $x$.*

The interaction of the $q\bar{q}$ pair with the proton is described by the dipole cross section $\sigma(x, r)$ which is modelled in our analysis. The most crucial element is the adoption of the $x$-dependent *saturation radius*

$$R_0(x) \;=\; \frac{1}{Q_0}\left(\frac{x}{x_0}\right)^{\lambda/2}\;, \tag{3.17}$$

which scales the quark-antiquark separation $r$ in the dipole cross section

$$\hat{\sigma}(x, r) \;=\; \sigma_0\; g\left(\hat{r} = \frac{r}{R_0(x)}\right)\;. \tag{3.18}$$

$Q_0 = 1$ GeV in eq. (3.17) sets the scale. The function $g$ in eq. (3.18) is not completely constrained. Important is, however, the quadratic rise at small $\hat{r}$ and the constant value at large $\hat{r}$. The form which we choose

$$g(\hat{r}) \;=\; 1 - \exp\left(-\hat{r}^2/4\right) \tag{3.19}$$

obeys these conditions and turns out to be very successful in the data description. In our analysis we fit the three parameters of the model $\sigma_0$, $\lambda$ and $x_0$ to all available inclusive DIS data with $x < 0.01$. For a detailed fit description see [94]; here we only quote the values of these parameters for orientation: $\sigma_0 = 23$ mb, $\lambda = 0.29$ and $x_0 = 3 \cdot 10^{-4}$ in the fit without the charm contribution. We additionally assumed a common mass of 140 MeV for the three light flavour quarks, which leads to a reasonable prediction in the photoproduction region, see section 3.2.2.

The main assumption about the form (3.19) concerns saturation property of the dipole cross section. For $\hat{r} \to \infty$ we have $g \to 1$ so that $\hat{\sigma} \to \sigma_0$. The fact that the dipole cross section is limited by the energy independent cross section $\sigma_0$ may be regarded as a unitarity bound. It leads to the behaviour of the total cross section, $\sigma_{\gamma^* p} \sim \log(1/x)$, which obeys the unitarity condition (2.97). In the opposite limit, when $\hat{r} \to 0$, the function $g \sim \hat{r}^2$ and the dipole cross section has the pQCD property of colour transparency, discussed in Section 3.1.1.

The saturation radius $R_0(x)$ distinguishes between the regions of colour transparency and saturation for the dipole cross section. The transition between them is $x$-dependent, and occurs for smaller dipole sizes $r$ as $x \to 0$, see Fig. 3.2. This is an essential feature of the model which agrees with the picture of parton saturation. In particular, $R_0(x)$ can be related to the saturation scale $Q_s(x) \sim 1/R_0(x)$, discussed in Section 2.4.4. For the dipoles with the sizes below $R_0$, the standard single ladder exchange dominates, close to $R_0$ multiple interactions (saturation effects) become important while for $r \gg R_0$ nonperturbative effects dominate. This picture has been qualitatively confirmed by the QCD analysis with the help of nonlinear evolution equations [66], done after the presented model was proposed, see also [55].

It is instructive to contrast (3.18) with the dipole cross section obtained from the BFKL equation. Neglecting the exponential in (2.86) and using relation (3.10), we find for small $r$

$$\hat{\sigma}(x,r) \;\sim\; x^{-\overline{\alpha}_s 4\ln 2}\, r\,. \tag{3.20}$$

The linear increase in $r$ is finally tamed, but nothing prevents $\hat{\sigma}$ from violating unitarity due to the power-like rise in $x$ when $x \to 0$. We solve this problem by the $x$-dependent transition to saturation.

### 3.2.1 Qualitative analysis

Now, we are ready now to conclude our qualitative analysis based on eqs. (3.15) and (3.16). In order to obtain the leading $Q^2$ behaviour, we approximate the dipole cross section (3.18) by

$$\hat{\sigma}(x,r) \;=\; \begin{cases} \sigma_0\, r^2/4R_0^2(x) & \text{for} \quad r \le 2R_0(x) \\ \\ \sigma_0 & \text{for} \quad r > 2R_0(x)\,. \end{cases} \tag{3.21}$$

This form contains all essential features of the exact formula for the leading $Q^2$ analysis.

In addition to the scale $R_0$, which we interpret as the *mean distance* in the transverse plane between partons in the proton, there is another scale $1/Q$, the *characteristic size* of the $q\bar{q}$ pair. The $Q^2$-behaviour of $\sigma_{T,L}$ depends on the relation between the two scales.

If the characteristic size of the $q\bar{q}$ pair is much smaller than the mean distance between partons,

$$\frac{1}{Q} \ll R_0(x)\,, \tag{3.22}$$

the transverse cross section (3.15) becomes

$$\sigma_T \;\sim\; \underbrace{\int_0^{4/Q^2} \frac{dr^2}{r^2}\left(\frac{\sigma_0\, r^2}{4R_0^2}\right)}_{symmetric} + \underbrace{\int_{4/Q^2}^{4R_0^2} \frac{dr^2}{r^2}\left(\frac{1}{Q^2 r^2}\right)\left(\frac{\sigma_0\, r^2}{4R_0^2}\right)}_{aligned\ jet} + \underbrace{\int_{4R_0^2}^{\infty} \frac{dr^2}{r^2}\left(\frac{1}{Q^2 r^2}\right)\sigma_0}_{aligned\ jet}\,.$$

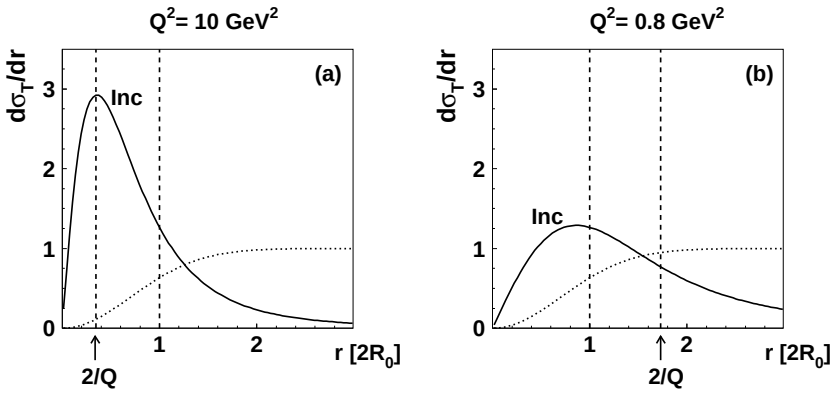


Figure 3.3: *The distribution $d\sigma_T/dr$ as a function of the dipole size $r$ (solid lines) for two values of $Q^2$ and $W = 245$ GeV. The dipole cross section (3.18) is shown as the dotted lines. The $r$-axis is in units of $2R_0(x) = 0.37$ fm for (a), and $2R_0(x) = 0.26$ fm for (b).*

After computing the relevant integrals, we obtain *scaling* behaviour of the structure function $F_T \sim Q^2\,\sigma_T$ with logarithmic violation

$$\sigma_T \;\sim\; \underbrace{\frac{\sigma_0}{Q^2R_0^2}}_{r<2/Q} \;+\; \underbrace{\frac{\sigma_0}{Q^2R_0^2}\,\log(Q^2R_0^2)}_{2/Q<r<2R_0} \;+\; \underbrace{\frac{\sigma_0}{Q^2R_0^2}}_{r>2R_0} \tag{3.23}$$

where we have suppressed similar numerical coefficients (of the order of $\alpha_{em}/\pi$) for each contribution[2].

Notice that both symmetric and aligned jet configurations contribute to the leading twist result. The intermediate contribution, $2/Q < r < 2R_0$, is especially enhanced due to the large logarithm. An important contribution comes also from the region $r > 2R_0$ which is dominated by nonperturbative sizes with a large hadronic cross section $\sigma_0$. The smallness of the suppression factor $1/Q^2r^2$, however, compensates this effect leading to the scaling contribution. This is a realization of the observation made by Bjorken and Kogut in [97]. The qualitative results are illustrated in Fig. 3.3a, where $d\sigma_T/dr$ as a function of $r$, computed from (3.7), is shown by the solid lines. The dipole cross section (3.18) is plotted as the dotted lines.

The presented analysis of $\sigma_T$ provides an additional motivation for the power-like form of $R_0(x)$. In such a case

$$F_T \;\sim\; x^{-\lambda}, \tag{3.24}$$

which reflects the small-$x$ increase of the DIS cross section, similar to that obtained from the BFKL equation. The precise value of $\lambda$ is not predicted in our approach but it is fitted to the data. Thus, it can phenomenologically take into account the next-to-leading logarithmic corrections to the BFKL equation which are known to be important for the value of $\lambda$.

[2]This analysis shows that $2/Q$ and $2R_0$ are better characteristic scales.

The opposite relation, valid when the $q\bar{q}$ pair size is much larger than the mean distance between partons,

$$\frac{1}{Q} \gg R_0(x)\,, \tag{3.25}$$

leads to a different behaviour from the point of view of the leading powers of $Q^2$. The transverse cross section (3.15) takes now the form

$$\sigma_T \;\sim\; \underbrace{\int_0^{4R_0^2} \frac{dr^2}{r^2}\,\left(\frac{\sigma_0\, r^2}{4R_0^2}\right)}_{symmetric} \;+\; \underbrace{\int_{4R_0^2}^{4/Q^2} \frac{dr^2}{r^2}\,\sigma_0}_{symmetric} \;+\; \underbrace{\int_{4/Q^2}^{\infty} \frac{dr^2}{r^2}\left(\frac{1}{Q^2 r^2}\right)\sigma_0}_{aligned\ jet}$$

which leads to

$$\sigma_T \;\sim\; \underbrace{\sigma_0}_{r<2R_0} \;+\; \underbrace{\sigma_0\,\log\left(\frac{1}{Q^2R_0^2}\right)}_{2R_0<r<2/Q} \;+\; \underbrace{\sigma_0}_{r>2/Q}\,. \tag{3.26}$$

Notice that even the region of small $r$, where the dipole cross section features colour transparency, leads to $\sigma_T \sim \sigma_0$. The energy dependence of $\sigma_T$ is also different, now it comes through the logarithmic term with the $x$-dependent $R_0$. Thus we expect a smooth change from the behaviour given by (3.24) to a milder dependence

$$F_T \;\sim\; Q^2\sigma_0\,\log(1/x)\,, \tag{3.27}$$

being in agreement with the unitarity bound (2.97).

The discussed case is illustrated in Fig. 3.3b by showing $d\sigma_T/dr$ as a function of $r$. Notice that $d\sigma_T/dr$ does no longer peak around $r = 2/Q$, as it does in the scaling case. In our interpretation, the limit $1/Q \gg R_0$ corresponds to the situation in which the $q\bar{q}$ pair cannot resolve individual partons, and the partonic system becomes dense for the probe. As a result, the dipole cross section becomes large and multiple interactions are important.

The transition from scaling to the saturated behaviour is marked by the *critical line* in the $(x, Q^2)$-plane for which the characteristic $q\bar{q}$ size equals the mean separation between partons,

$$\frac{1}{Q_s} = R_0(x_s)\,. \tag{3.28}$$

In reality, the line may become a strip marking the transition region. What matters is the relation between $Q_s$ and $x_s$. Since $R_0^2(x) \sim x^\lambda$, the saturation scale $Q_s$ becomes higher when $x_s \to 0$, see Fig. 3.4. Therefore, with decreasing Bjorken-$x$ one has to go to smaller distances (larger $Q^2$) to resolve a dense parton structure of the proton. This makes the process of the transition from scaling to saturated form perturbative and gives a hope that this process can be described by perturbative QCD. The role of the critical line is discussed from a different point of view in Section (3.2.5).

The same analysis can be performed for the longitudinal cross section. In the scaling region, $Q^2R_0^2 \gg 1$, the leading contribution comes only from the

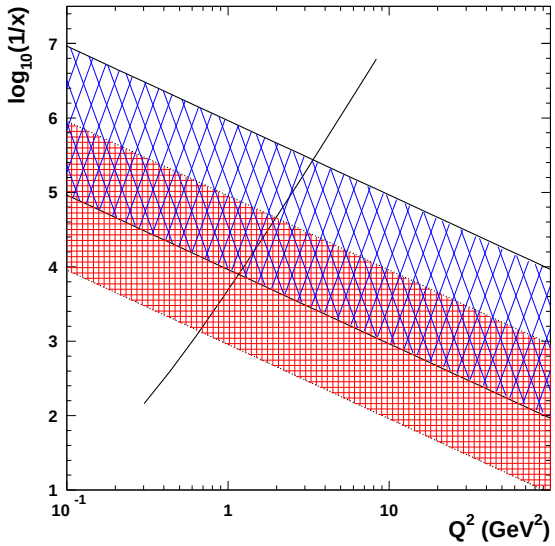


Figure 3.4: *The position of the critical line in the* $(x, Q^2)$*-plane. The acceptance regions of HERA (lower band) and the future TeV (upper band) colliders are shown. Scaling region,* $Q^2R_0^2 \gg 1$*, is to the right, and saturation region,* $Q^2R_0^2 \ll 1$*, to the left of the line.*

symmetric in $z$ and intermediate configuration $r < 2R_0$, see relation (3.16) for the comparison,

$$\sigma_L \sim \underbrace{\frac{\sigma_0}{Q^2R_0^2}}_{r<2/Q} + \underbrace{\frac{\sigma_0}{Q^2R_0^2}}_{2/Q<r<2R_0} + \underbrace{\frac{\sigma_0}{Q^4R_0^4}}_{r>2R_0} . \tag{3.29}$$

Aligned jet configuration for $r > 2R_0$ is higher twist, suppressed by an additional power of $Q^2$. The reason is the factor $z^2(1-z)^2$ in the longitudinal wave function (3.9) which suppresses the end point (aligned jet) configuration. Therefore, the longitudinal cross section is dominated by the perturbative contribution. Notice also a lack of a logarithmic enhancement of the leading twist contribution. Thus $\sigma_L$ will be significantly smaller than $\sigma_T$, see (3.23) for the comparison. In the region, $Q^2R_0^2 < 1$, close to the critical line, we have

$$\sigma_L \sim \sigma_0 . \tag{3.30}$$

The result of the comparison of the saturation model with data for $\sigma_{\gamma^* p} = \sigma_T + \sigma_L$ as a function of $Q^2$ for fixed energy $W$ of the $\gamma^* p$ system is shown in Fig. 3.5. The plot also illustrates the effect of a light quark mass on the results. It should be mentioned that at HERA the density of partons at the saturation scale $Q_s^2 \sim$ 1-2 $GeV^2$ is not particularly high. For this purpose the next generation TeV colliders would be better (see Fig. 3.4). For the saturation scale, however, the size of the virtual probe ($\sim 0.3$ fm) is large enough to see blackness of the proton, most probably due to the size of the constituent quark

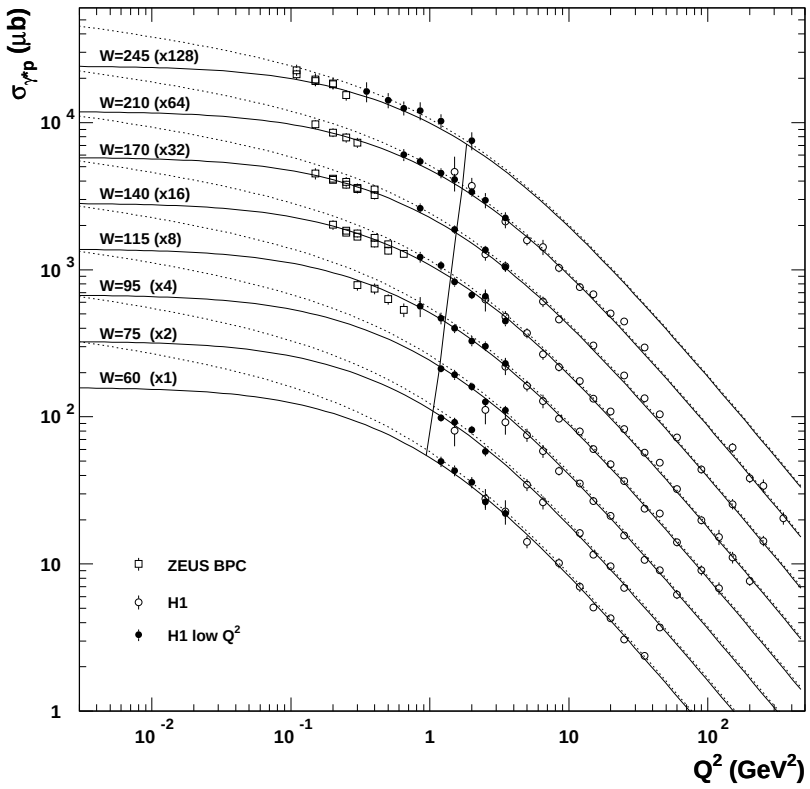


Figure 3.5: *The $\gamma^* p$ cross section for various energies. The solid lines show the fit results with a light quark mass $m_f = 140$ MeV. The dotted lines show the same cross sections with $m_f = 0$. The line across the curves indicates the position of the critical line.*

structure. In Fig. 3.6 we show the structure function $F_2$ plotted as a function of $x$ for different values of $Q^2$. Notice the change of the slope in $x$ with $Q^2$ and good agreement between the data and the results of the saturation model (solid lines).

In summary, the saturation model naturally explains the transition from scaling to saturation in the DIS cross section measured in the experiments at HERA. This description is related to the concepts of a dense partonic system and the critical line, which are closely related to unitarization of the DIS cross sections at small $x$.

### 3.2.2 Small $Q^2$ limit

It is interesting to consider a formal limit $Q^2 \to 0$ in the saturation model. The analyzed cross sections are divergent in this limit if $m_f = 0$. However, if a non-zero quark mass is assumed the formal limit can be found. Performing the analysis similar to that presented in the previous section, we obtain the

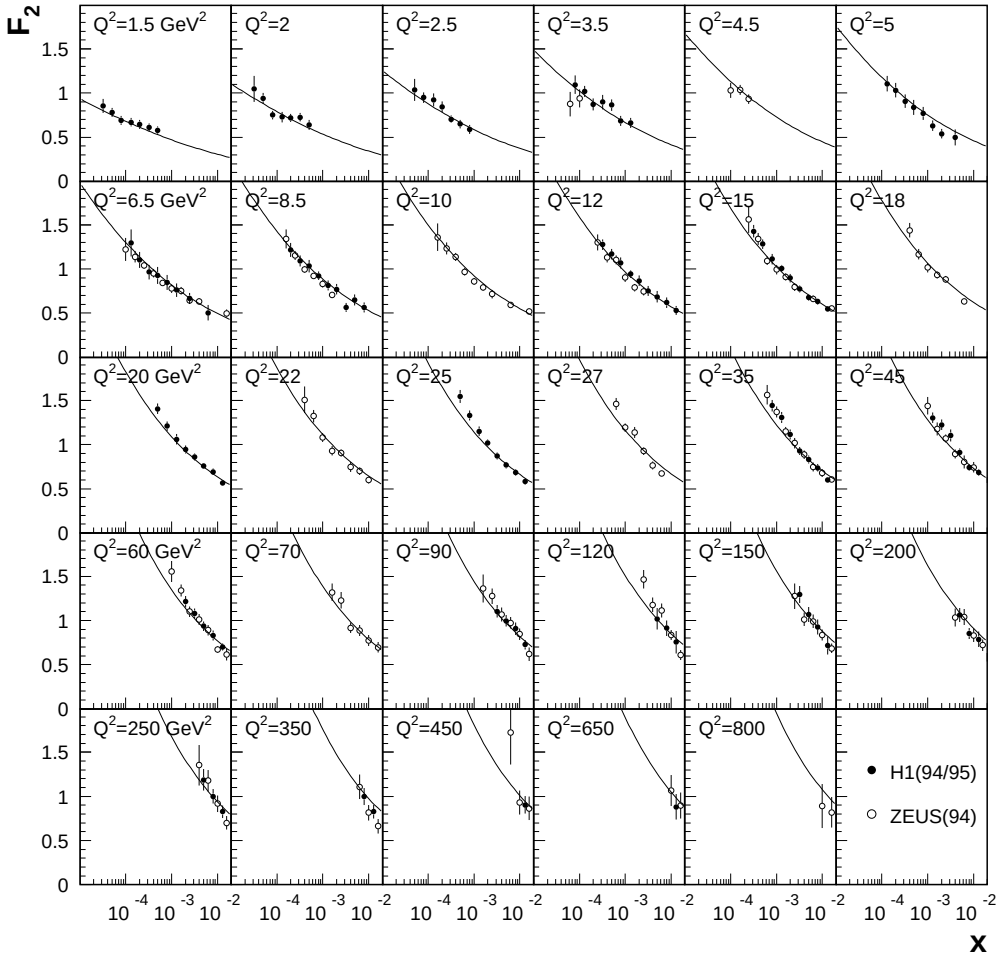


Figure 3.6: *$F_2$ as a function of $x$ for different $Q^2$ values. The solid lines are results of the saturation model. The data are from the H1 and ZEUS collaborations.*

following result, valid when $m_f^2 \gg Q^2 \to 0$,

$$\sigma_T \sim \sigma_0 \log\left(\frac{1}{m_f^2 R_0^2(x)}\right) \tag{3.31}$$

$$\sigma_L \sim \sigma_0 \frac{Q^2}{m_f^2}, \tag{3.32}$$

where we additionally modify the Bjorken-$x$ formula to allow for the photoproduction limit

$$x = \frac{Q^2 + 4m_f^2}{W^2}. \tag{3.33}$$

As expected, the longitudinal cross section vanishes when $Q^2 = 0$. We also see that $m_f$ plays a crucial role for the value of the transverse cross sections. In

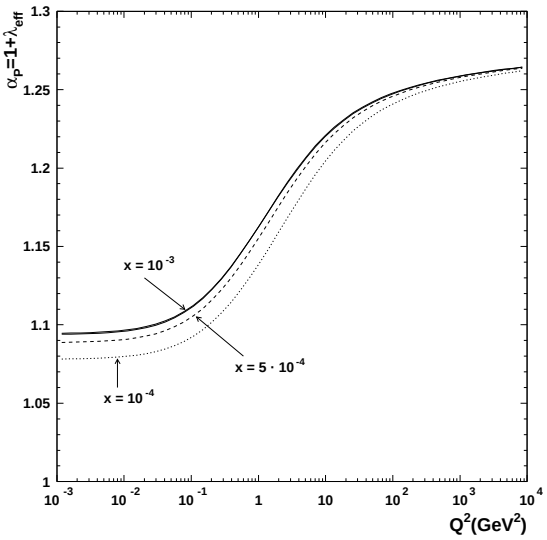


Figure 3.7: *The effective pomeron intercept $\alpha_P$ in $\sigma_{\gamma^* p} \sim (W^2)^{\alpha_P - 1}$ as a function of $Q^2$. The three curves illustrate different methods of calculation, see Ref. [94] for more details.*

our analysis we set $m_f = 140$ MeV to obtain good agreement with the HERA photoproduction data. For $Q^2 \gg m_f^2$, the quark mass does not play a significant role.

From eqs. (3.31)-(3.33) we see that for photoproduction the energy behaviour is given by

$$\sigma_{\gamma^* p} \sim \log(W^2)\,. \tag{3.34}$$

This should be contrasted to the energy behaviour found in the DIS with $Q^2 \gg 1/R_0^2(x)$, see eq. (3.24),

$$\sigma_{\gamma^* p} \sim (W^2)^{\lambda}\,. \tag{3.35}$$

These two extreme cases show a drastic change in the energy dependence with the change of $Q^2$. It appears that for each fixed value of $Q^2$, including photoproduction region, we can effectively parameterize the energy dependence through the power-like behaviour: $\sigma_{\gamma^* p} \sim (W^2)^{\alpha_P(Q^2)-1}$, see [94] for more details. The change with $Q^2$ of the power $\alpha_P(Q^2)$ is shown in Fig. 3.7. Interestingly, $\alpha_P$ interpolates between the soft and hard pomeron intercept values for small and large values of $Q^2$, respectively.

We should warn the reader that the results presented in this subsection should only be interpreted as an observation about the effective parameterization which can be extended down to photoproduction region. We do not claim that there is a perturbative way to access that region. As emphasized by many studies, at some low values of $Q^2$ the chiral symmetry breaking effects come into play. A similar effect appears in the presented parameterization as a dependence on quark mass, which is yet another parameter to be tuned. Having $Q^2$ even lower, confinement effects are dominant and we can no longer talk of quarks and gluons but rather about mesons and baryons.

### 3.2.3 Inclusive charm production

In formula (3.7) which we use for the description of inclusive DIS at small $x$ the summation is performed over quark flavours, including the charm quark contribution. Different flavours are distinguished by a quark mass and electric charge in the photon wave function. The dipole cross section has the same form for each flavour, with the modification (3.33) of the Bjorken-$x$. When the fit to DIS data on $F_2$ is done, the charm contribution will result as a prediction of the model for the inclusive charm production which can be compared with data.

In order to understand the charm production we perform the qualitative analysis similar to that in Section 3.2.1. Since we cannot neglect the charm mass, $m_c \approx 1.5$ GeV, our starting formula (3.14) now takes the following form

$$\sigma_T^{c\bar{c}} \sim \int_0^\infty dr^2 \int_0^1 dz \, [z^2 + (1-z)^2] \, \frac{\hat{\sigma}(x,r)}{r^2} \, \Theta\left[(z(1-z)\, Q^2 + m_c^2) r^2 < 1\right] , \tag{3.36}$$

plus the term proportional to $m_c^2$, coming from the transverse wave function (3.8), which leads to the same features as the leading term presented above.

As before, we want to perform first the integration over $z$. In this case we solve the quadratic relation in $z$ imposed by the theta function. If $r < 2/\sqrt{Q^2+4m_c^2}$ there is no restriction on the $z$-integration and we obtain symmetric configuration. For $2/\sqrt{Q^2+4m_c^2} \ll r < 1/m_c$ aligned jet configuration is enforced ($z \approx 0, 1$). In contrast to the massless analysis, the quark mass introduces a cut-off on the maximal size of the $c\bar{c}$ dipole: $r_{max} = 1/m_c$. Collecting these results, we find

$$\sigma_T^{c\bar{c}} \sim \underbrace{\int_0^{4/(Q^2+4m_c^2)} \frac{dr^2}{r^2} \, \hat{\sigma}(x,r)}_{symmetric} + \underbrace{\int_{4/(Q^2+4m_c^2)}^{1/m_c^2} \frac{dr^2}{r^2} \left(\frac{1}{Q^2 r^2}\right) \hat{\sigma}(x,r)}_{aligned\ jet} , \tag{3.37}$$

that should be compared to the massless relation (3.15).

In the saturation model, as a result of the fit to data, we have in the entire HERA kinematic domain

$$1/m_c < 2R_0(x) \tag{3.38}$$

Therefore, inclusive charm production probes mostly the colour transparency part of the dipole cross section: $\hat{\sigma} = \sigma_0 \, r^2/4R_0^2$. In other words, the charm quark mass restricts the $c\bar{c}$ dipole size to the perturbative values for which unitarization effects are not yet important.

The scale given by $4m_c^2$ leads to a different behaviour of $\sigma_T^{c\bar{c}}$ as a function of $Q^2$, similar to the already discussed behaviour of the inclusive cross section. If $Q^2 \gg 4m_c^2$, after substituting the colour transparency form of $\hat{\sigma}$ into (3.37), we obtain

$$\sigma_T^{c\bar{c}} \sim \frac{\sigma_0}{Q^2 R_0^2} + \frac{\sigma_0}{Q^2 R_0^2} \log(Q^2/4m_c^2) . \tag{3.39}$$

The logarithmic enhancement comes from the aligned jet integral. In the opposite case, when $Q^2 \ll 4m_c^2$, only the symmetric configuration contributes, and

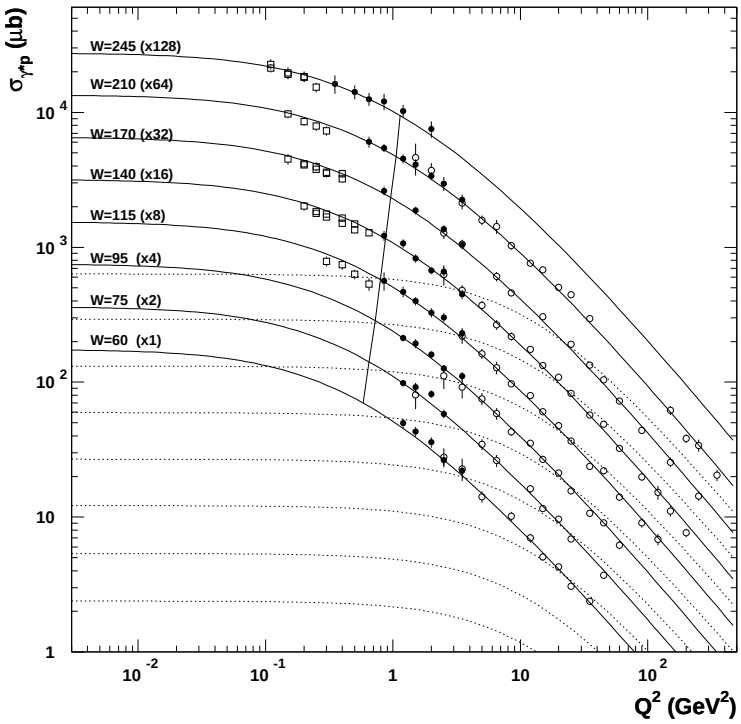


Figure 3.8: *The $\gamma^* p$ cross section (solid lines) from the fit with the charm quark contribution This contribution is shown separately by the dotted lines.*

we find

$$\sigma_T^{c\bar{c}} \;\sim\; \frac{\sigma_0}{4m_c^2 R_0^2}\,. \tag{3.40}$$

These results are illustrated by the dotted lines in Fig. 3.8, showing the charm contribution $\sigma^{c\bar{c}}$ which undergoes the transition around $4m_c^2 \approx 10$ GeV$^2$. Thus, the transition of $\sigma^{c\bar{c}}$ to the saturated form is unrelated with the saturation of the dipole cross section, but is dictated by the relation between the scales $Q^2$ and $4m_c^2$. This is due to the relation (3.38), valid at HERA.

### 3.2.4 Geometric scaling

Let us recall our basic formula

$$\sigma_{T,L}(x,Q^2) \;=\; \int d^2\mathbf{r} \int_0^1 dz \;\sum_f\; |\Psi_{T,L}^f(\mathbf{r},z,Q^2)|^2 \;\hat{\sigma}(r/R_0(x))\,. \tag{3.41}$$

where the photon wave functions are given by eqs. (3.8) and (3.9). We explicitly indicated the basic scaling property of our model, namely that $\hat{\sigma}$ depends on $x$ and $r$ through the dimensionless combination $\hat{r} = r/R_0(x)$. This has profound consequences for the measured cross section $\sigma_{\gamma^* p} = \sigma_T + \sigma_L$. If we neglect the quark mass $m_f$ in the photon wave functions we can rescale the dipole size $r \to \hat{r}$ in (3.41) such that the integration variables are dimensionless. Thus,

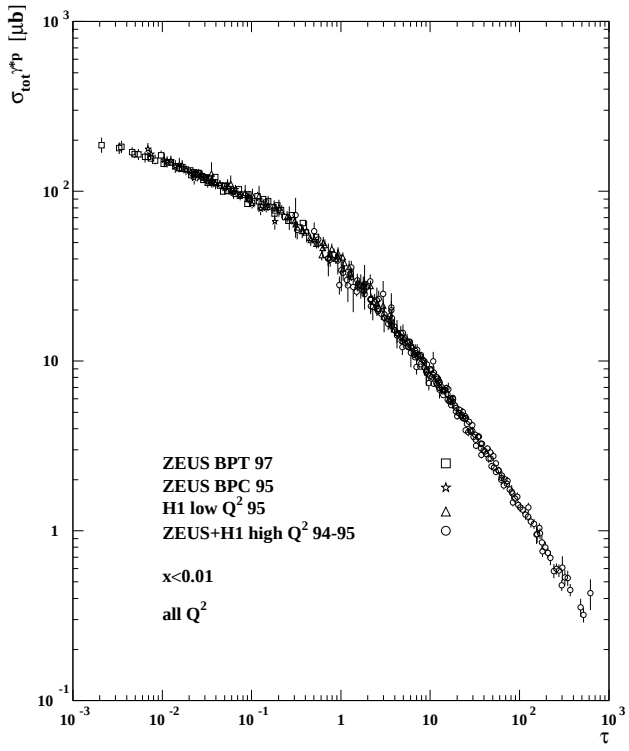


Figure 3.9: *Experimental data on* $\sigma_{\gamma^* p}$ *from the region* $x < 0.01$ *plotted versus the scaling variable* $\tau = Q^2 R_0^2(x)$. *The* $Q^2$ *values are in the range between* 0.045 *and* 450 GeV$^2$.

after the integration $\sigma_{\gamma^* p}$ becomes a function of only one dimensionless variable: $\tau = Q^2 R_0^2(x)$,

$$\sigma_{\gamma^* p}(x, Q^2) \; = \; \sigma_{\gamma^* p}(\tau)\,. \tag{3.42}$$

This fact is explicitly shown in the Mellin representation (3.43) of $\sigma_{\gamma^* p}$, presented in the next section. Since our model describes data well, the new scaling is predicted for real data in a broad range of $Q^2$ [98]. The nonzero light quark mass, introduced to extrapolate the model down to photoproduction, does not lead to a significant breaking of the scaling. So does the charm contribution. In Fig. 3.9, reproduced from [98], we illustrate the scaling (3.42) by showing $\sigma_{\gamma^* p}$ as a function of $\tau$, for the small-$x$ data with $x < 0.01$.

In its essence, the new scaling is a manifestation of the presence of the internal saturation scale characterizing dense partonic systems, $Q_s(x) \sim 1/R_0(x)$. This scale emerges from a pioneering work of [39], which was subsequently analyzed and generalized in [56]- [67]. In the analysis [45], and more recently in [66], the scaling properties similar to those postulated in (3.18) were found. An independent formulation [63] of the small $x$ processes, gives the same overall picture with the saturation scale. At a deeper level, the geometric scaling for small-$x$ processes may reflect self similarity or conformal symmetry of the underlying dynamics. More detailed studies are under way, see [61]-[67].

### 3.2.5 Twist expansion

Following the approach in [94] we express the $\gamma^* p$ cross section in the saturation model in the Mellin representation which is particularly suitable for the analysis of the twist expansion. In the massless limit we find [94]

$$\sigma_{T,L} \;=\; \sigma_0 \int_{-\infty}^{\infty} \frac{d\nu}{2\pi} \left(\frac{1}{Q^2 R_0^2(x)}\right)^{1/2+i\nu} \tilde{H}_{T,L}(\nu)\,, \tag{3.43}$$

where

$$\tilde{H}_T(\nu) \;=\; \frac{3\alpha_{em}}{16}\,\overline{e^2}\left(\frac{9/4+\nu^2}{1+\nu^2}\right)\left(\frac{\pi}{\mathrm{ch}\pi\nu}\right)^2\left(\frac{\mathrm{sh}\pi\nu}{\pi\nu}\right)\,\Gamma(3/2+i\nu), \tag{3.44}$$

$$\tilde{H}_L(\nu) \;=\; \frac{3\alpha_{em}}{8}\,\overline{e^2}\left(\frac{1/4+\nu^2}{1+\nu^2}\right)\left(\frac{\pi}{\mathrm{ch}\pi\nu}\right)^2\left(\frac{\mathrm{sh}\pi\nu}{\pi\nu}\right)\,\Gamma(3/2+i\nu) \tag{3.45}$$

and we denote $\overline{e^2} = \sum_f e_f^2$.

Using this representation, we construct the expansion in powers of $1/Q^2$ (twist expansion) or $Q^2$. The qualitative results of Section 3.2.1 are confirmed in such an analysis.

The cross section (3.43) is given by the Mellin-Barnes type integral which exists for any value of the parameter $1/Q^2R_0^2$, except for 0 and $\infty$. In practice, the integration can be performed numerically or computed in terms of the sum over residues. A closer look at eq. (3.44) reveals that we deal with multiple poles in the complex $\nu$-plane at

$$\nu = \pm i(2n+1)/2\,, \qquad\qquad n = 0,1,2... \tag{3.46}$$

If the integration contour in (3.43) is closed in the upper half-plane and the residues of the poles at $\nu = i(2n+1)/2$ are computed, we obtain a representation in terms of positive powers of $Q^2R_0^2$, with an infinite radius of convergence. For $Q^2R_0^2 < 1$ the first pole $\nu = i/2$ gives a reasonable approximation

$$\sigma_T^{(0)} \;=\; \frac{\alpha_{em}}{\pi}\,\overline{e^2}\,\sigma_0\left(\log(1/Q^2R_0^2) - \gamma_E + 7/6\right)\,, \tag{3.47}$$

$$\sigma_L^{(0)} \;=\; \frac{\alpha_{em}}{\pi}\,\overline{e^2}\,\sigma_0\,. \tag{3.48}$$

For $Q^2R_0^2 > 1$ it is more practical to construct an expansion in powers of $1/(Q^2R_0^2)$, by computing the residues at $\nu = -i(2n+1)/2$. It can be proven that the obtained expansion is only asymptotic. The integration contour cannot be closed in the lower half-plane because the integral over the lower semi-circle is divergent for the infinite radius. The scaling contribution is given by the first pole at $\nu = -i/2$

$$\sigma_T^{(2)} \;=\; \frac{\alpha_{em}}{\pi}\,\overline{e^2}\,\frac{\sigma_0}{Q^2R_0^2}\,\left(\log(Q^2R_0^2) + \gamma_E + 1/6\right)\,, \tag{3.49}$$

$$\sigma_L^{(2)} \;=\; \frac{\alpha_{em}}{\pi}\,\overline{e^2}\,\frac{\sigma_0}{Q^2R_0^2}\,, \tag{3.50}$$

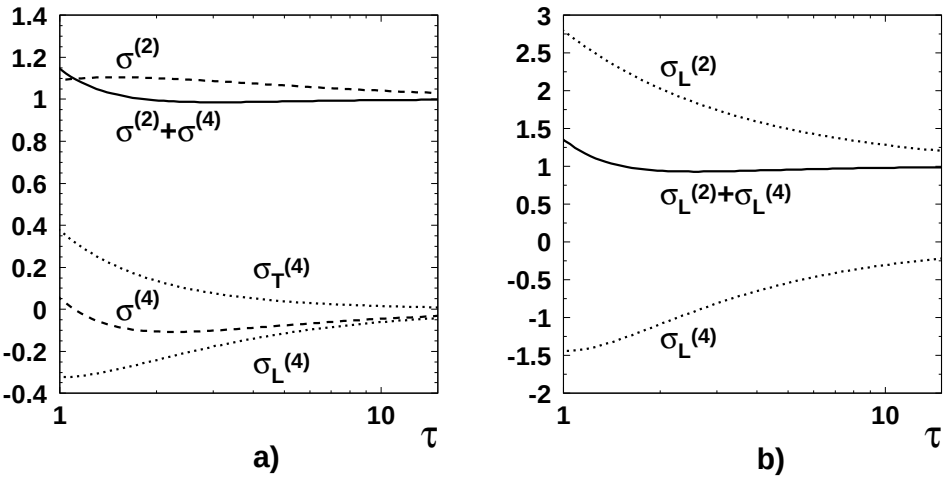


Figure 3.10: *a): The contribution of different twists to the total cross section. b): The contribution to the longitudinal cross section. The curves are normalized to the exact results which corresponds to 1 on the perpendicular axes. The variable* $\tau = Q^2 R_0^2$.

where $\gamma_E \approx 0.5772$ is Euler's constant. The next pole at $\nu = -3i/2$ gives the twist-4 contribution

$$\sigma_T^{(4)} = \frac{3}{5} \frac{\alpha_{em}}{\pi} \overline{e^2} \frac{\sigma_0}{Q^4 R_0^4} , \tag{3.51}$$

$$\sigma_L^{(4)} = -\frac{4}{5} \frac{\alpha_{em}}{\pi} \overline{e^2} \frac{\sigma_0}{Q^4 R_0^4} \left( \log(Q^2 R_0^2) + \gamma_E + 1/15 \right) . \tag{3.52}$$

The logarithms which appear in the above formulas are due to multi-pole singularity structure, e.g. $\nu = -3i/2$ is a double pole for $\sigma_L$.

Notice that the transverse and longitudinal twist-4 contributions have opposite signs and their absolute values are of the same order. Separately, they are not small in comparison to the twist-2 components. However, the detailed numerical analysis performed in [99] shows that in the sum $\sigma^{(4)} = \sigma_T^{(4)} + \sigma_L^{(4)}$ they cancel each other in such a way that only a small (negative) addition to the leading twist-2 result is produced, see Fig. 3.10a. Thus, higher twist contributions to $F_2$ are not large in DIS at small $x$ down to $Q^2 \geq 1$ GeV$^2$ (close to the critical line). A similar effect was found in the QCD analysis of DIS data at low $x$, based on the leading twist DGLAP evolution equations [100].

In contrast, $\sigma_L^{(4)}$ alone gives a significant negative correction to the leading twist contribution $\sigma_L^{(2)}$, especially for $Q^2 R_0^2 \approx 1$, see Fig. 3.10b. This result should be taken into account in an analysis of future experimental results on the longitudinal structure function.

The critical line plays a very important role in the analysis of twist contributions in DIS at small $x$. It gives an estimate on the region of validity of the twist expansion. Comparing (3.49) with (3.47), we see that moving across

the critical line $Q^2 R_0^2(x) = 1$ we change the behaviour from $\sigma_{T,L} \sim 1/Q^2$ to $\sigma_{T,L} \sim \sigma_0$. For $Q^2 R_0^2(x) < 1$ the approximation based on the twist expansion quickly deteriorates.

### 3.2.6 Relation to the gluon distribution

We derive the relation between the ordinary gluon distribution $g(x, Q^2)$ which appears in the leading twist description of DIS based on collinear factorization, and the unintegrated gluon distribution $f(x, Q^2)$ introduced by the $k_T$-factorization formula (2.92).

In the double logarithmic approximation, when the summation of the leading powers of $\alpha_s \log(1/x) \log Q^2 \sim 1$ is performed, the following twist-2 result is obtained from the DGLAP evolution equations in the small-$x$ limit

$$\frac{\partial F_2(x, Q^2)}{\partial \ln Q^2} = \frac{\alpha_s}{3\pi} \overline{e^2}\, x g(x, Q^2) \,. \tag{3.53}$$

We will find a similar result for the twist-2 component of the structure function $F_2$, computed using the $k_T$-factorization formula. By the comparison with (3.53), the relation between the two gluon distributions can be found.

The Mellin representation of $F_2$, computed in the $k_T$-factorization scheme is the basis for our considerations. The computations are similar to those leading to eq. (3.43), but now we need the result for a general form of the dipole cross section or the unintegrated gluon distribution, see eq. (3.10). Applying the method described in [94], we find

$$\begin{aligned} F_2(x, Q^2) &= \frac{\overline{e^2}}{16} \int_{-\infty}^{\infty} \frac{d\nu}{2\pi} \left(\frac{11/4 + 3\nu^2}{1+\nu^2}\right) \left(\frac{\pi}{\mathrm{ch}\pi\nu}\right)^2 \left(\frac{\mathrm{sh}\pi\nu}{\pi\nu}\right) \\ &\times \int_0^{\infty} \frac{dl^2}{l^2} \alpha_s f(x, l^2) \left(\frac{l^2}{Q^2}\right)^{-1/2+i\nu} \,. \end{aligned} \tag{3.54}$$

The logarithmic derivative of $F_2$ has the additional factor $(1/2 - i\nu)$ under the integral

$$\begin{aligned} \frac{\partial F_2(x, Q^2)}{\partial \ln Q^2} &= \frac{\overline{e^2}}{16} \int_{-\infty}^{\infty} \frac{d\nu}{2\pi} \left(\frac{11/4 + 3\nu^2}{1+\nu^2}\right) \left(\frac{\pi}{\mathrm{ch}\pi\nu}\right)^2 \left(\frac{\mathrm{sh}\pi\nu}{\pi\nu}\right) (1/2 - i\nu) \\ &\times \left\{ \int_0^{Q^2} \frac{dl^2}{l^2} \alpha_s f(x, l^2) \left(\frac{l^2}{Q^2}\right)^{-1/2+i\nu} + \int_{Q^2}^{\infty} \frac{dl^2}{l^2} \alpha_s f(x, l^2) \left(\frac{l^2}{Q^2}\right)^{-1/2+i\nu} \right\} \,, \end{aligned}$$

where we split the integration over the gluon transverse momentum into the $l^2 < Q^2$ and $l^2 > Q^2$ parts. Twist-2 contribution is found after closing the integration contour in the lower half-plane for $l^2 \leq Q^2$, and computing the residue at $\nu = -i/2$. Thus, we find

$$\frac{\partial F_2^{(2)}(x, Q^2)}{\partial \ln Q^2} = \frac{\alpha_s}{3\pi} \overline{e^2} \int_0^{Q^2} \frac{dl^2}{l^2} f(x, l^2) \,. \tag{3.55}$$

A direct comparison with the DLLA formula (3.53) gives the result we are looking for

$$xg(x,Q^2) \;=\; \int_0^{Q^2} \frac{dl^2}{l^2} f(x,l^2)\,. \tag{3.56}$$

Relation (3.56 )is valid in the limit of small $x$ and large $Q^2$. Additionally, it has to be taken with care since the integration over $l^2$ is performed in the nonperturbative region of small $l^2$. Unless we have some model for this region, the found relation should be interpreted as

$$xg(x,Q^2) \;=\; xg(x,Q_0^2) \;+\; \int_{Q_0}^{Q^2} \frac{dl^2}{l^2} f(x,l^2)\,, \tag{3.57}$$

where the both scales are perturbative and large, and $xg(x,Q_0^2)$ is known, e.g. from a fit to data.

The renormalization group approach, presented in Section 2.3.1, tells us that $\alpha_s$ in the DLLA formula (3.53) should be evaluated at the scale given by $Q^2$. On the other hand, the scale for $\alpha_s$ in eq. (3.55) is not determined since the radiative corrections leading to running $\alpha_s$ are beyond the leading $\log(1/x)$ approximation in which this result was derived. Thus, the same scale $Q^2$ as for the DLLA result can only be postulated for $\alpha_s$ in eq. (3.55).

We finish our considerations by calculating the twist-2 part of the logarithmic slope of $F_2$ in the saturation model. From (3.49), we have

$$\frac{\partial F_2^{(2)}(x,Q^2)}{\partial \log Q^2} \;=\; \frac{\overline{e^2}}{4\pi^3}\,\frac{\sigma_0}{R_0^2(x)}\,, \tag{3.58}$$

and by the comparison with eq. (3.53) we find the following gluon distribution for large $Q^2$

$$xg(x,Q^2) \;=\; \frac{3}{4\pi^2\alpha_s(Q^2)}\,\frac{\sigma_0}{R_0^2(x)}\,. \tag{3.59}$$

The found gluon distribution depends on $Q^2$ only through the coupling constant $\alpha_s$. Thus, the proper DGLAP evolution in the large $Q^2$ limit is not included in the constructed model. This may be improved by modifying the behaviour of the dipole cross section at $r \ll 2R_0(x)$. Indeed, approximating in eq. (3.10) $(1 - J_0(lr)) \approx (lr)^2/4$, which is valid for $l^2 < 1/r^2$ up to a few percent, and using eq. (3.56), we find that for small enough $r$ (for an alternative derivation see [101] and references therein)

$$\hat{\sigma}(x,r) \;\simeq\; \frac{\pi^2}{3}\,\alpha_s(1/r^2)\,r^2\,xg(x,1/r^2)\,, \tag{3.60}$$

where $xg(x,\mu^2)$ is the gluon distribution which evolves in $\mu^2 = 1/r^2$ according to the DGLAP evolution equations. The physics of saturation, however, is not affected by such a modification at small transverse sizes. Additionally, a better agreement with the data is obtained for large values of $Q^2$ [102].

## 3.3 Transition to low $Q^2$ in other approaches

We briefly describe other approaches to the description of the transition to low $Q^2$ of the proton structure function $F_2$ which use conceptually different ideas from ours.

### A. Donnachie-Landshoff approach

In this approach [103] $F_2$ is postulated in the form dictated by Regge theory, assuming three contributions given by different Regge trajectories.

$$F_2(x,Q^2) \;=\; f_0(Q^2)\,x^{-\epsilon_0} \;+\; f_1(Q^2)\,x^{-\epsilon_1} \;+\; f_2(Q^2)\,x^{-\epsilon_2}\,, \tag{3.61}$$

where the powers $\epsilon_i$ are related to intercepts of the Regge trajectories:

$$\epsilon_i = \alpha_i(0) - 1\,. \tag{3.62}$$

The values $\epsilon_1 = 0.08$ and $\epsilon_2 = -0.45$, which correspond to the soft pomeron and $(\rho,\omega,f,a)$ trajectories, respectively, were fixed. The value $\epsilon_0 \approx 0.4$ was found from a fit to the small-$x$ data. The form factors $f_i(Q^2)$ were parameterized in the following way

$$f_0(Q^2) \;=\; A_0\left(\frac{Q^2}{Q^2+Q_0^2}\right)^{1+\epsilon_0}\left(1+\frac{Q^2}{Q_0^2}\right)^{\epsilon_0/2}, \tag{3.63}$$

$$f_1(Q^2) \;=\; A_1\left(\frac{Q^2}{Q^2+Q_1^2}\right)^{1+\epsilon_1}\left(1+\sqrt{\frac{Q^2}{Q_S^2}}\right)^{-1}, \tag{3.64}$$

$$f_2(Q^2) \;=\; A_2\left(\frac{Q^2}{Q^2+Q_2^2}\right)^{1+\epsilon_2}. \tag{3.65}$$

The small $Q^2$ behaviour was constrained by the requirement that $F_2 \sim Q^2$ when $Q^2 \to 0$ for fixed $W^2$. The parameters: $A_{0-2}$, $Q^2_{0-2}$, $Q_S^2$ were found from a fit to the data in the range of $x < 0.07$ and $Q^2 = 0$ to 2000 GeV$^2$.

The soft pomeron form factor $f_1(Q^2)$ dominates at low $Q^2$, whereas at large $Q^2 > 10$ GeV$^2$ it falls off as $1/Q$. The hard pomeron form factor $f_0(Q^2)$ slowly departs from zero at small $Q^2$ to rise rapidly as $Q^2 \sim Q^{\epsilon_0}$ for $Q^2 > 10$ GeV$^2$. In this way the soft–hard pomeron transition is enforced by the data. Let us recall that a similar effect is realized in the saturation model without introducing the two pomeron concept.

It should be mentioned that in the DL model the strong rise in $x$ is not tamed, leading to violation of unitarity when $x \to 0$.

### B. Badelek-Kwieciński model

In this model [104] $F_2$ is a sum of two contributions which interpolate between the region of low $Q^2$ where $F_2$ is well described by the Vector Dominance Model (VDM) [105], and the region of large values of $Q^2$ where the leading twist formula obtained from the DGLAP fit to the data dominates, see e.g. [100],

$$F_2(x,Q^2) \;=\; F_2^{VDM}(x,Q^2) \;+\; F_2^{QCD}(x,Q^2) \tag{3.66}$$

and

$$F_2^{VDM}(x,Q^2) = \frac{Q^2}{4\pi}\sum_{V=\rho,\omega,\phi}\frac{M_V^4\,\sigma_V(W^2)}{\gamma_V^2\,(Q^2+M_V^2)^2}\,, \tag{3.67}$$

$$F_2^{QCD}(x,Q^2) = \frac{Q^2}{Q^2+Q_0^2}\,F_2^{AS}(\bar{x},Q^2+Q_0^2)\,, \tag{3.68}$$

where the sum over vector meson contributions is performed in which $M_V$ is mass of the vector meson $V$. The vector meson–proton cross section $\sigma_V(W^2)$ is determined from the $\pi p$ and $Kp$ total cross sections using the additive quark model and $\gamma_V^2$ is found from the leptonic width of the vector meson $V$. The variable $\bar{x}$ in $F_2^{AS}$ is given by

$$\bar{x} = \frac{Q^2+Q_0^2}{W^2+Q^2-M_p^2+Q_0^2}\,, \tag{3.69}$$

where the parameter $Q_0^2 = 1.2 - 1.5\ GeV^2$. This is the only parameter in the model, except those fixed independently in the VDM and DGLAP analyses. A different realization of the same idea can be found in [106]. Similarly to the DL approach, the unitarity condition (2.97) is violated in this model.

There exist several other effective parameterizations of $F_2$ which interpolate between the small and large $Q^2$ behaviour of the proton structure function. An extensive discussion of them is given in [107]. More recent parameterizations can be found in [108]. The most comprehensive overview of the nucleon structure functions, both from the theoretical and experimental side, is given in [109].

# Chapter 4

# Diffractive DIS

A significant fraction (around 10%) of deep inelastic scattering events observed at HERA at small $x$ are diffractive events [86, 87]. For these events the incoming proton stays intact despite inelasticity of the reaction, losing only a small fraction $x_{I\!P}$ of its initial momentum. The final state proton is well separated in rapidity from the rest of the system which looks like a typical DIS event. Thus the large rapidity gap is a characteristic feature of diffractive DIS. In partonic language, a colour neutral cluster of partons fragments independently of the scattered proton. The ratio of the diffractive to all DIS events is to a good approximation constant as a function of Bjorken-$x$ and $Q^2$. The latter condition suggests the leading twist nature of DIS diffraction. For recent reviews on diffraction see [110, 111, 112].

Historically, the first description of diffractive DIS was provided in terms of the Ingelman–Schlein (IS) model [113]. The model is based on Regge theory in which diffractive processes are due to the exchange of a soft pomeron, see Section 2.4.1. In other words, the proton stays intact due to the exchange with vacuum numbers. The novelty of the IS model lies in the assumption that the pomeron has a partonic structure as do real hadrons. The diffractive structure function factorizes into a "pomeron flux" and a pomeron structure function. The latter function is written in terms of the pomeron parton distributions, determined from a fit to data with the help of the standard DGLAP evolution equations [86, 87, 114, 115, 116]. In the alternative method, the phenomenology of soft hadronic reactions has been used [117, 118, 119]. Despite conceptual difficulties (the pomeron is not a particle) this idea turned out to be very useful in the description of the DIS diffractive data, provided a harder value of the intercept of the pomeron trajectory is assumed. The IS approach was generalized by considering the exchange of subleading reggeons (and also pions) [120, 121, 122, 86] to explain the diffractive data collected by the H1 collaboration at HERA. We describe the IS based approach in detail in Section 4.2, following [117, 114, 115, 120, 121, 122].

An alternative approach to diffractive processes in DIS is represented by a detailed modelling of the diffractive state as well as of the mechanism leading to diffraction, starting from perturbative QCD. In such an approach the diffractive state is formed by the Fock components of the light-cone virtual photon wave

function:

$$|\gamma> = |q\bar{q}> + |q\bar{q}\,g> + \ldots . \tag{4.1}$$

The $q\bar{q}$ component was considered in [123, 124, 125, 126]. A higher order contribution represented by the $q\bar{q}$ pair with an additional gluon $g$ emitted was studied in [127, 128, 129, 130, 95]. The $q\bar{q}$ and $q\bar{q}g$ components subsequently interact with the proton through the net colourless exchange. The way in which this exchange is realized distinguishes between the models. In the simplest case, the colourless exchange responsible for the rapidity gap is modelled by two perturbative gluons coupled to the proton with some form factor [131, 132, 88, 89] or to a heavy onium which serves as a model of the proton [133]. Higher order corrections are included by the BFKL summation of gluon ladders [134] or using the colour dipole approach [135]. The diffractive processes have also been described with the help of the interaction with a semiclassical colour field of the proton [126, 130].

The immediate problem faced in the above modelling is the strong sensitivity to nonperturbative effects due to the dominance of aligned jet configuration (to be discussed in Section 4.3.2). Thus, we need a description of the interactions in the soft regime. The model of the dipole cross section based on the ideas of partonic saturation, presented in the previous chapter, provides such a description. The parameters of this model were determined from the analysis of inclusive DIS [94]. Now, it can be directly applied to diffractive DIS without tuning additional parameters [95]. The main result which we present in Section 4.3, based on the analysis [95], is a very good description of the data. In particular, the constant ratio $\sigma_{diff}/\sigma_{tot}$ is naturally explained. Also harder than the soft pomeron value of an effective pomeron intercept is predicted in perfect agreement with the data.

The leading twist nature of DIS diffraction brings the issue of collinear factorization and diffractive parton distributions. By this we mean the consistent factorization of the diffractive cross sections into a convolution of hard cross sections and the diffractive parton distributions, see Section 2.3 for the discussion in the inclusive case. The Ingelman–Schlein approach assumes collinear factorization, imposing an additional assumption, called Regge factorization, on the $x_{I\!P}$-dependence of the diffractive parton distributions. The form in $\beta$ is usually fitted to the data. On the other hand, in the perturbative QCD approach the diffractive parton distributions can be directly computed. In particular, if the saturation model is used, the Regge factorization results from this model. Another important aspect, which cannot be addressed in the IS approach, is the role of higher twist contributions. It appears that diffractive DIS is an example of the process for which twist-4 (given by the $q\bar{q}$ component from longitudinal photons) dominates over leading twist in the kinematic range of small diffractive mass [127, 128]. In Section 4.4 we discuss these issues, based on the results from [155].

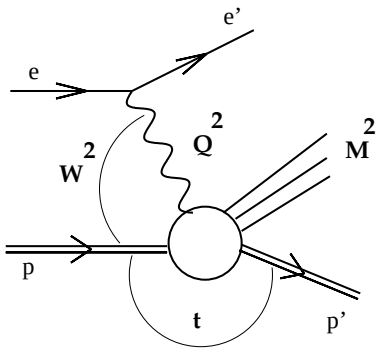


Figure 4.1: *Kinematic invariants in DIS diffraction.*

## 4.1 Diffractive structure functions

We have several dimensional scales in diffractive DIS scattering

$$e + p \;\rightarrow\; e' + p' + X\,, \tag{4.2}$$

where $X$ is a diffractive system. In addition to these known from inclusive DIS: $Q^2$ and $W^2$, the mass of the diffractive system $M^2$, and the invariant four-momentum transfer from the proton into the diffractive system, $t = (p - p')^2$, come into the game, see Fig. 4.1. The following dimensionless variables are built out of them.

The lost fraction of the incident proton momentum

$$x_{I\!P} \;=\; \frac{Q^2 + M^2 - t}{Q^2 + W^2}\,. \tag{4.3}$$

In the pomeron model interpretation it is a fraction of the proton momentum carried by the pomeron. The variable

$$\beta \;=\; \frac{Q^2}{Q^2 + M^2 - t} \tag{4.4}$$

is the Bjorken variable related to the diffractive system $M^2$. In the pomeron model of diffraction $\beta$ is a fraction of the *pomeron* momentum carried by the struck quark. The ordinary Bjorken variable

$$x \;=\; x_{I\!P}\,\beta\,. \tag{4.5}$$

In the following we neglect $t$ in the definition of the variables $x_{I\!P}$ and $\beta$ since usually $|t| \ll Q^2, M^2$.

The diffractive structure functions are defined analogous to the inclusive case. They depend on the four invariant variables $(x, Q^2, x_{I\!P}, t)$ and are defined through the diffractive DIS cross section

$$\frac{d^4\sigma^D}{dx\,dQ^2\,dx_{I\!P}\,dt} \;=\; \frac{2\pi\alpha_{em}^2}{x\,Q^4}\left\{\left[1 + (1-y)^2\right]\,\frac{d\,F_2^D}{dx_{I\!P}\,dt} \;-\; y^2\,\frac{d\,F_L^D}{dx_{I\!P}\,dt}\right\}. \tag{4.6}$$

For simplicity of notation, we introduce the following

$$F_2^{D(4)}(x, Q^2, x_{I\!P}, t) \equiv \frac{d\,F_2^D}{dx_{I\!P}\,dt}(x, Q^2, x_{I\!P}, t)\,, \tag{4.7}$$

$$F_L^{D(4)}(x, Q^2, x_{I\!P}, t) \equiv \frac{d\,F_L^D}{dx_{I\!P}\,dt}(x, Q^2, x_{I\!P}, t)\,, \tag{4.8}$$

where we explicitly indicate that the diffractive structure functions depend on four variables. As usual

$$F_2^{D(4)} = F_T^{D(4)} + F_L^{D(4)}. \tag{4.9}$$

Notice that the introduced diffractive structure functions have dimension $\mathrm{GeV}^{-2}$ because of the differential $dt$ in the definition of the cross section (4.6).

We also define the structure functions integrated over $t$ since they are measured when the final state proton momentum is not detected. In this case

$$F_{T,L}^{D(3)}(x, Q^2, x_{I\!P}) = \int_{-\infty}^{0} dt\; F_{T,L}^{D(4)}(x, Q^2; x_{I\!P}, t) \tag{4.10}$$

is dimensionless. The diffractive structure functions are related to the diffractive photon-proton cross sections

$$F_{T,L}^{D(4)} = \frac{Q^2}{4\pi^2\alpha_{em}}\,\frac{d\sigma_{T,L}(\gamma^* p \to p' X)}{dx_{I\!P}\,dt}\,, \tag{4.11}$$

where $T, L$ denote the virtual photon polarization.

## 4.2 The Ingelman–Schlein model

In the Ingelman–Schlein model [113] the diffractive structure function $F_2^{(4)}$ is given by the following factorized form

$$F_2^{(4)}(x, Q^2, x_{I\!P}, t) = f_{I\!P}(x_{I\!P}, t)\; F_2^{I\!P}(\beta, Q^2)\,, \tag{4.12}$$

where we remind that $\beta = x/x_{I\!P}$ is the analogue of the Bjorken variable. The physical interpretation of the above factorization, which we call the Regge factorization, is as follows. The diffractive scattering occurs through the exchange of the pomeron with the momentum $p_{I\!P} = x_{I\!P} \cdot p$, described by the flux $f(x_{I\!P}, t)$, and a subsequent hard scattering of the virtual photon on the partonic constituent of the pomeron which carries a fraction $\beta$ of the *pomeron* momentum. The latter interaction is characterized by the pomeron structure function $F_2^{I\!P}(\beta, Q^2)$. The structure function (4.12) is schematically shown in Fig. 4.2.

The pomeron exchange is described by the flux factor

$$f_{I\!P}(x_{I\!P}, t) = \frac{N}{16\,\pi}\, x_{I\!P}^{1-2\,\alpha_{I\!P}(t)}\; B_{I\!P}^2(t)\,, \tag{4.13}$$

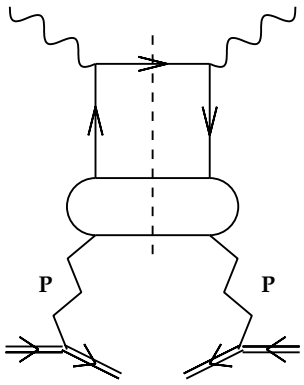


Figure 4.2: *Diffractive structure function in the Ingelman–Schlein model. The spring-like lines represent the pomeron.*

where the pomeron trajectory is assumed to have the "soft" values of the parameters found in the analysis of hadronic reactions

$$\alpha_{I\!P}(t) \;=\; 1.08 \;+\; 0.25\,\mathrm{GeV}^{-2}\cdot t\,. \tag{4.14}$$

It appears that for DIS diffraction the value of the intercept $\alpha_{I\!P}(0)$ has to be increased to $\alpha_{I\!P}(0) \approx 1.13 - 1.20$.

$B_{I\!P}(t)$ describes the pomeron coupling to the proton. Phenomenologically, it has been established that the pomeron trajectory couples to the proton through the Dirac elastic form factor [21]

$$B_{I\!P}(t) \;=\; \frac{4\,m^2 - 2.79\,t}{4\,m^2 - t}\left(\frac{1}{1 - t/0.71}\right)^2 . \tag{4.15}$$

The normalization $N = 2/\pi$ in eq. (4.13) follows the Donnachie–Landshoff convention [136].

The pomeron structure function is expressed through the quark distributions in the pomeron $q^{I\!P}(\beta, Q^2)$ in a full analogy to the proton case

$$F_2^{I\!P}(\beta, Q^2) \;=\; 2\,\sum_f e_f^2\;\beta\, q_f^{I\!P}(\beta, Q^2)\,, \tag{4.16}$$

where $f$ distinguishes different flavours. The factor 2 results from the assumption that the distribution of quarks and antiquarks in the pomeron are identical,

$$q_f^{I\!P}(\beta, Q^2) = \bar{q}_f^{I\!P}(\beta, Q^2)\,, \tag{4.17}$$

for each flavour $f$, since the pomeron is the vacuum quantum number exchange.

The $Q^2$-dependence of the pomeron parton distributions is governed by the DGLAP evolution equations, which lead to the logarithmic scaling violation of the diffractive structure function. We have to allow for the pomeron gluon distribution $g^{I\!P}(\beta, Q^2)$ which is automatically generated by the the evolution equations from the quark distributions. The initial form in $\beta$ of the pomeron parton distributions can be obtained in two different ways. In the first method,

used in the analysis of DIS data, the initial form is given with the help of several parameters. Then the parameters are determined from the fit to available data. This procedure was successfully applied to DIS diffractive data [86, 87, 114, 115, 116]. In the case of the pomeron a different method exists. The initial pomeron parton distributions can be estimated from soft pomeron phenomenology of hadronic reactions [117, 118, 119].

In the next section we present an example of such an estimation, following the analysis [117].

### 4.2.1 Pomeron parton distributions

At first we shall specify the details of the parton distributions in the pomeron at the reference scale $Q_0^2 = 4$ GeV$^2$. At small $\beta$ both the quark and gluon distributions are assumed to be dominated by the pomeron exchange,

$$\beta\, q_f^{I\!P}(\beta, Q_0^2, t) = a_f^{I\!P}(t)\ \beta^{1-\alpha_{I\!P}(0)}\,, \tag{4.18}$$

$$\beta\, g^{I\!P}(\beta, Q_0^2, t) = a_g^{I\!P}(t)\ \beta^{1-\alpha_{I\!P}(0)}\,. \tag{4.19}$$

The functions $a_f^{I\!P}(t)$ and $a_g^{I\!P}(t)$ can be estimated from the factorization of pomeron couplings [137, 138, 139] :

$$a_f^{I\!P}(t) = r(t)\ a_f\,, \qquad\qquad a_g^{I\!P}(t) = r(t)\ a_g\,, \tag{4.20}$$

where the parameters $a_f$ and $a_g$ are the pomeron couplings controlling the normalization of the small $x$ behaviour of the sea quark and gluon distributions in the *proton* i.e.

$$\begin{aligned} xq_f(x, Q_0^2) + x\bar{q}_f(x, Q_0^2) &= 2\ a_f\ x^{1-\alpha_{I\!P}(0)}\,, \\ xg(x, Q_0^2) &= a_g\ x^{1-\alpha_{I\!P}(0)}\,, \end{aligned} \tag{4.21}$$

and the function $r(t)$ is

$$r(t) = \frac{\pi}{2}\frac{G_{I\!P I\!P I\!P}(t)}{B(0)}\,. \tag{4.22}$$

The coupling $G_{I\!P I\!P I\!P}(t)$ is the triple pomeron coupling (see Fig. 4.3 a) and its magnitude can be estimated from the cross section of the diffractive production $p + \bar{p} \to p + X$ in the limit of large mass $M_X$ of the diffractively produced system $X$. We neglected the (weak) $t$ dependence of the function $r(t)$ and have estimated its magnitude from the Tevatron data [140] as $r(t) \approx r(0) = 0.089$. The parameters $a_f$ were estimated assuming that the sea quark distributions in the *proton* can be parameterized as:

$$xq_f(x, Q_0^2) + x\bar{q}_f(x, Q_0^2)\ =\ 2\ a_f\ x^{1-\alpha_{I\!P}(0)}\ (1-x)^7\,, \tag{4.23}$$

and fixing the constants $a_f$ from the requirement that the average momentum fraction which corresponds to those distributions is the same as that which follows from the parameterization of parton distributions in the proton [141].

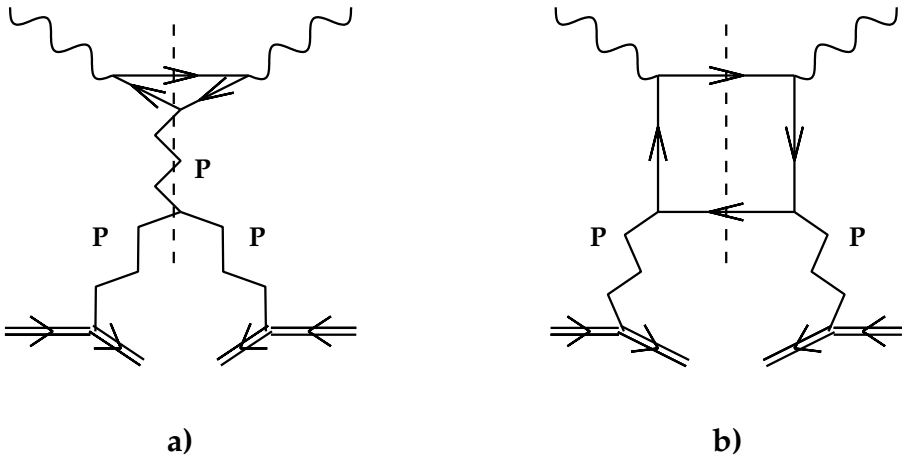


Figure 4.3: *Contribution to diffractive structure function for small $\beta$ (a) and large $\beta$ (b). The spring-like lines represent the pomeron.*

The momentum sum rule has also been used to fix the parameter $a_g$ i.e. we assumed

$$xg(x, Q_0^2) \;=\; a_g \; x^{1-\alpha_{I\!P}(0)} \; (1-x)^5 \,, \tag{4.24}$$

and imposed the condition that the gluons carry 1/2 momentum of the proton. We extrapolated the pomeron dominated quark and gluon distributions in the pomeron (see (4.19)) to the region of arbitrary values of $\beta$ by multiplying the factor $\beta^{1-\alpha_{I\!P}(0)}$ by $(1-\beta)$ [138].

We have also included the term proportional to $\beta(1-\beta)$ in both the quark and gluon distributions [138]. The normalization of this term in the quark distributions has been estimated in [136] assuming that it is dominated by the quark-box diagram with the non-perturbative couplings of pomeron to quarks, shown in Fig. 4.3 b. In this model one gets:

$$\beta \; q^{I\!P}(\beta, Q_0^2) \;=\; \frac{C\pi}{3} \; \beta \; (1-\beta) \,, \tag{4.25}$$

where $C \approx 0.17$ [136]. We found that the fairly reasonable description of data can be achieved provided that the constant $C$ is enhanced by a factor equal to 1.5. We have also assumed that the relative normalization of the quark distributions in the pomeron corresponding to different flavours is the same as that of the sea quark distributions in the proton [141]. Finally the normalization of the term proportional to $\beta(1-\beta)$ in the gluon distribution in the pomeron has been obtained by imposing the momentum sum rule. Following the approximations discussed above we have neglected the $t$ dependence in those parton distributions.

As the result of the estimates and extrapolations discussed above, the parameterization of parton distributions in the pomeron at the reference scale $Q_0^2 = 4$ GeV$^2$ looks as follows:

$$\beta \; g^{I\!P}(\beta, Q_0^2) \;\;=\;\; (0.218 \; \beta^{-0.08} + 3.30 \; \beta) \; (1-\beta) \tag{4.26}$$

for the gluon distribution, and

$$\begin{aligned} \beta\, d^{I\!P}(\beta, Q_0^2) = \beta\, u^{I\!P}(\beta, Q_0^2) &= 0.4\,(1-\delta)\; S^{I\!P}(\beta) \\ \beta\, s^{I\!P}(\beta, Q_0^2) &= 0.2\,(1-\delta)\; S^{I\!P}(\beta) \\ \beta\, c^{I\!P}(\beta, Q_0^2) &= \delta\; S^{I\!P}(\beta)\,, \end{aligned} \tag{4.27}$$

for the quark distributions. The function $S^{I\!P}(\beta)$ is parameterized as below

$$S^{I\!P}(\beta) = (0.0528\;\beta^{-0.08} \;+\; 0.801\;\beta)\;(1-\beta) \tag{4.28}$$

and $\delta$=0.02 [141]. The analysis of the pomeron structure functions based on different parameterizations of parton distributions in the pomeron has also been presented in Refs. [139, 118].

The parton distributions defined above were next evolved up to the values of $Q^2$ for which the data exist using the LO DGLAP evolution equations with $\Lambda = 0.255$ GeV. The results of the comparison with the H1 data is shown in Fig. 4.5 (solid curves).

From the presented pomeron parton distributions the pomeron structure function $F_2^{I\!P}$ follows. For example, at small $\beta$

$$F_2^{I\!P}(\beta, Q^2) \;=\; A_{I\!P}(Q^2)\;\beta^{-0.08}\,, \tag{4.29}$$

where the coefficient $A_{I\!P}(Q^2)$ , as shown above, is a product of the $I\!P I\!P I\!P$ coupling and the $Q^2$ dependent coupling of the pomeron to the virtual photons, see Fig. 4.3 a. From the presented parameterization $A_{I\!P} = 0.03$ for $Q^2 = 4\,\mathrm{GeV}^2$.

### 4.2.2 Subleading reggeons

The subleading reggeons can describe the nonpomeron part of the diffractive scattering which leads to breaking of the Regge factorized form of the diffractive structure function (4.12). Strictly speaking we cannot call such processes diffractive since diffraction is usually associated with the leading pomeron exchange. However, for simplicity we use the same terminology for the nonpomeron reggeon exchanges, including processes with fast forward neutron in the final state which correspond to isospin $I = 1$ exchange.

Thus we postulate the following extension of the Ingelman–Schlein model [120]

$$F_2^{(4)}(x, Q^2, x_{I\!P}, t) \;=\; f_{I\!P}(x_{I\!P}, t)\, F_2^{I\!P}(\beta, Q^2) \;+\; \sum_R f_R(x_{I\!P}, t)\, F_2^R(\beta, Q^2)\,, \tag{4.30}$$

where the additional terms describe reggeon exchanges. Note, that in such an approach the Regge factorization is broken – $F_2^{(4)}$ is no longer a product of two factors with a particular dependence on kinematical variables like in (4.12). As a consequence, there is no a simple and universal $x_{I\!P}$-dependence: $F_2^{(4)} \sim x_{I\!P}^{-n}$. The last result is suggested by the H1 Collaboration data in which a different value of $n$ seems to be predominant for larger values $x_{I\!P}$ ($> 0.01$) [86].

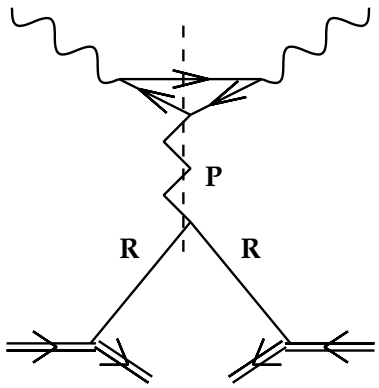


Figure 4.4: *The reggeon-reggeon-pomeron contribution to diffractive structure function.*

The Regge factorization breaking can be explained by the exchange of subleading reggeons, isoscalar $(f_2, \omega)$ and isovector $(a_2, \rho)$. The reggeon flux factors in (4.30) are parameterized in analogy to the pomeron flux

$$f_R(x_{I\!P}, t) \;=\; \frac{N}{16\,\pi}\, x_{I\!P}^{1-2\,\alpha_R(t)}\; B_R^2(t)\; |\eta_R(t)|^2\,, \tag{4.31}$$

where the function $\eta_R(t)$ is a signature factor:

$$|\eta_R(t)|^2 \;=\; \begin{cases} 4\,\cos^2[\pi\alpha_R(t)/2] & \text{for even signature reggeons } (f_2, a_2) \\ \\ 4\,\sin^2[\pi\alpha_R(t)/2] & \text{for odd signature reggeons } (\rho, \omega)\,, \end{cases} \tag{4.32}$$

and $\alpha_R(t)$ is the reggeon trajectory. $B_R(t)$ describes the coupling of the reggeon to the proton.

We assume that $B_R(t) = B_R(0)\,\exp(t/2\Lambda_R^2)$ with $\Lambda_R = 0.65\,\mathrm{GeV}$, as known from the reggeon phenomenology of hadronic reactions. From the same analysis we obtain the parameters of the reggeon trajectory

$$\alpha_R(t) \;=\; 0.5475 \;+\; 1\,\mathrm{GeV}^{-2}\cdot t\,. \tag{4.33}$$

Moreover, the following relations between the reggeon-proton couplings are found [120, 121]

$$B_{f_2}^2(0) > B_\omega^2(0) \gg B_{a_2}^2(0) \sim B_\rho^2(0)\,. \tag{4.34}$$

This result shows that the isovector reggeons $(a_2, \rho)$ can safely be neglected in the presented analysis. These reggeons are crucial, however, for the diffractive process with fast forward neutron in the final state, see [121] for detailed discussion.

The reggeon structure function $F_2^R$ at small $\beta$, which is relevant for the $H1$ data analysis, can be found in a similar way as for the pomeron

$$F_2^R(\beta, Q^2) \;=\; A_R\;\beta^{-0.08}\,, \tag{4.35}$$

where now $A_R$ is determined by the triple Regge vertex $RR\mathbb{P}$ (see Fig. 4.4). In our analysis we introduce the ratio

$$C_{enh} = \frac{A_R}{A_{\mathbb{P}}}, \tag{4.36}$$

which is related to the ratio of the "triple-Regge" $RR\mathbb{P}$ and $\mathbb{P}\mathbb{P}\mathbb{P}$ couplings. It should be much bigger than one, as suggested by the analysis [142] of soft hadronic interactions. The data from the H1 collaboration [86], presented in terms of the structure function $F_2^{D(3)}$, prefer $C_{enh} \approx 10$ in which case reasonable agreement of our description with the data is obtained for $\beta \leq 0.4$. This is illustrated in Fig. 4.5, reproduced from [122], where the pure pomeron contribution from the analysis [117] (solid lines) and the effect of the reggeon terms (dashed lines) is shown.

We have also checked how the QCD evolution of the reggeon structure function (4.35) influences the results. We found that it was not important, especially in view of the triple-Regge coupling uncertainties. More details on the subleading reggeon contribution, as well as on the pion contribution which is relevant for $x_{\mathbb{P}} > 0.1$, can be found in [120, 121].

The fact that the presented description deteriorates for large values of $\beta$, i.e. in the region of small diffractive mass, is not accidental. To be more precise, the description falls significantly below data for $\beta > 0.4$, which is shown in the two rightmost columns in Fig. 4.5. A closer inspection reveals that the only way to cure this problem, within the description based on the Ingelman–Schlein model, is to assume that the gluon distribution in the pomeron is largely concentrated at $\beta \approx 1$ [86, 114, 115]. Our gluon distribution (4.26) is modeled keeping in mind the situation in the proton, where the gluon distribution is strongly suppressed for large $\beta$. Thus a suitable modification of the pomeron gluon distribution would be necessary.

We will not pursue, however, the analysis in this direction since we think that it does not lead to better understanding of DIS diffraction. Instead, we change to a description based directly on QCD, in which the diffractive state is formed by the components of the photon wave function (4.1). In this description, supplemented by the dipole cross section described in the previous chapter, all essential features of the Ingelman–Schlein model are present and naturally explained. In addition, the problem with the description of the region of large $\beta$ is cured by careful analysis of the longitudinal virtual photon contribution. This contribution, found to be concentrated at $\beta \approx 1$, is formally higher twist and of course cannot be treated by the leading twist pomeron parton distribution analysis in the Ingelman–Schlein model.

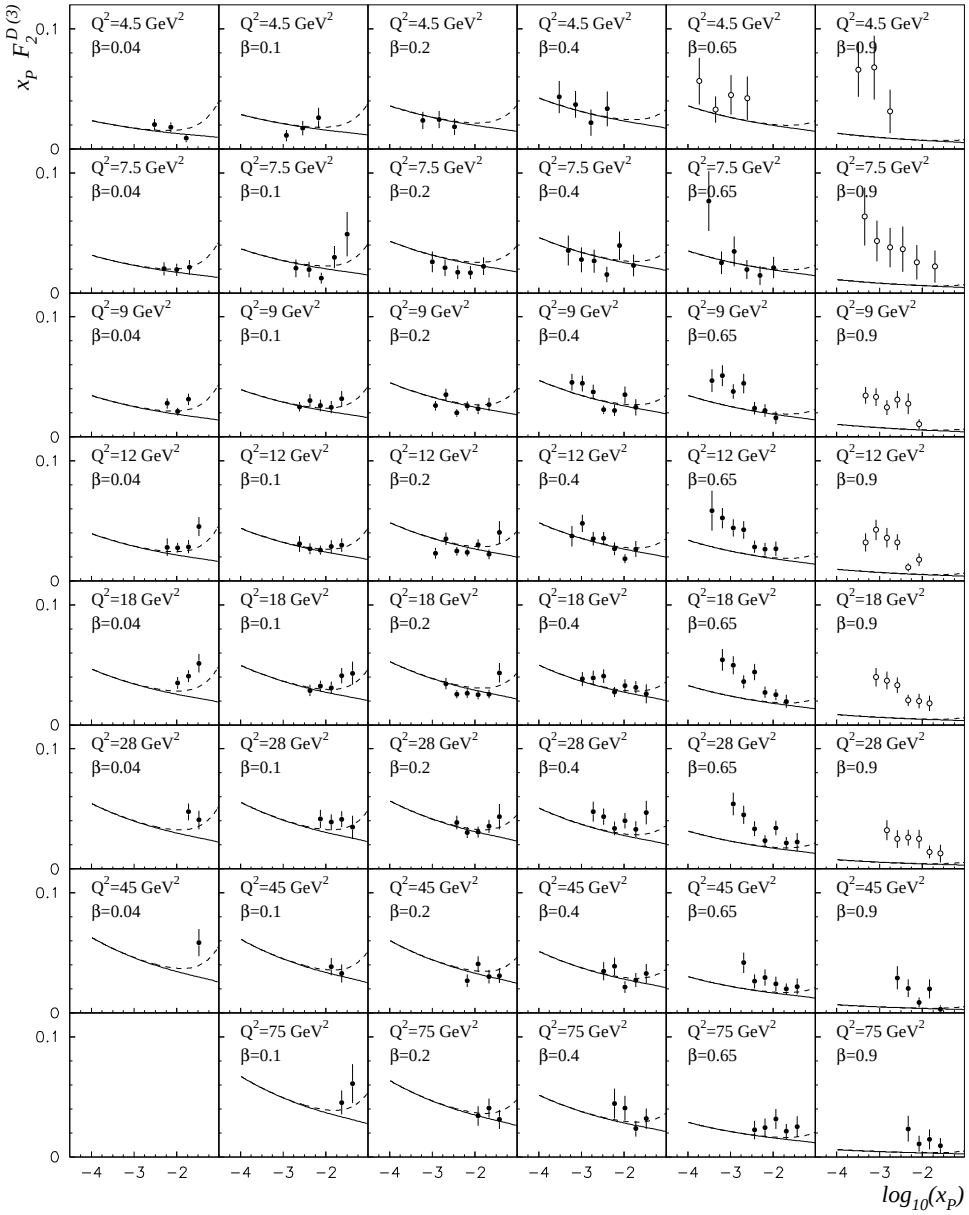


Figure 4.5: *Diffractive structure function $F_2^{D(3)}$ from the pomeron+reggeon analysis versus the H1 collaboration data. The solid lines correspond to the pomeron contribution and the dashed lines show the reggeon contribution with $C_{enh} = 10$.*

## 4.3 QCD based description

Let us consider the diffractive system formed by the first Fock component of the virtual photon wave function–the $q\bar{q}$ pair (see eq. (4.1)). The elastic scattering on the proton occurs through the coupling of two gluons in singlet state with the transverse momenta $\pm\mathbf{l}$, and the longitudinal momentum fractions $x_1$ and $x_2$ which obey

$$x_{I\!P} = x_1 - x_2 \,. \tag{4.37}$$

We consider the zero momentum transfer $t = 0$. There are four amplitudes for this process in which the two gluons couple to the quarks in all possible ways, one of them is shown in Fig. 4.6.

The final state quark momenta are decomposed in the base which consists of two light-like vectors $q' = q + x\,p$ and $p$, and two space-like transverse vectors orthogonal to the previous ones. Thus we have

$$k_1 \;=\; z\,q' \;+\; \frac{\mathbf{k}^2 + m_f^2}{s\,z}\,p \;+\; k_T \tag{4.38}$$

$$k_2 \;=\; (1-z)\,q' \;+\; \frac{\mathbf{k}^2 + m_f^2}{s\,(1-z)}\,p \;-\; k_T \,, \tag{4.39}$$

where $s = 2q' \cdot p$ and $m_f$ is the quark mass. In the frame in which the virtual photon and the proton are collinear along the $z$-axis, the transverse momentum $k_T = (0, \mathbf{k}, 0)$. The diffractive mass of the $q\bar{q}$ system is given by

$$M^2 \;=\; (k_1 + k_2)^2 \;=\; \frac{\mathbf{k}^2 + m_f^2}{z\,(1-z)} \,. \tag{4.40}$$

In the $\gamma^* I\!P$ center-of-mass frame ($p_{I\!P} = x_{I\!P} \cdot p$) $z$ is related to the quark scattering angle

$$\cos\theta \;=\; 1 - 2\,z \,. \tag{4.41}$$

For the symmetric configuration with $z = 1/2$ the quarks scatter at $\theta = \pi/2$. Aligned jet configuration with $z \approx 0$ corresponds to $\theta \approx 0$.

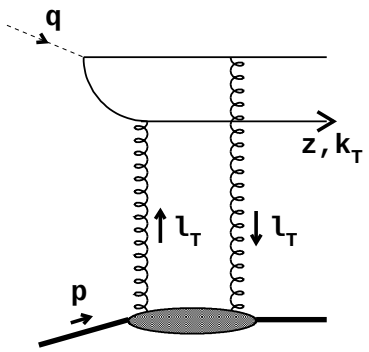


Figure 4.6: *Diffractive production of the $q\bar{q}$ pair.*

### 4.3.1 Basic cross sections

The cross sections for diffractive scattering from transverse and longitudinal photons

$$\gamma^* + p \to q\,\bar{q} + p' \tag{4.42}$$

are computed analogously to the inclusive case. Assuming the two-gluon exchange mechanism, the amplitude is the sum of two subamplitudes, with crossed and uncrossed exchanged gluons. In the high energy limit, the real parts of the two subamplitudes cancel, and we are left only with the imaginary part of the uncrossed amplitude which dominates the process. After squaring that amplitude we obtain for the transverse cross section [90]

$$\frac{d\,\sigma_T^D}{d^2\mathbf{k}\,dz\,dt\,|\,t=0} = \frac{\alpha_{em}}{6\,\pi}\,\sum_f e_f^2\,\int\frac{d^2\mathbf{l}}{l^4}\,\int\frac{d^2\mathbf{l}'}{l'^4}\,\alpha_s f(x_{I\!P},l^2)\,\alpha_s f(x_{I\!P},l'^2)$$

$$\times\left\{[z^2+(1-z)^2]\,\left\{\frac{\mathbf{k}}{D(\mathbf{k})}-\frac{\mathbf{k}+\mathbf{l}}{D(\mathbf{k}+\mathbf{l})}\right\}\cdot\left\{\frac{\mathbf{k}}{D(\mathbf{k})}-\frac{\mathbf{k}+\mathbf{l}'}{D(\mathbf{k}+\mathbf{l}')}\right\}\right.$$

$$\left.+\,m_f^2\,\left\{\frac{1}{D(\mathbf{k})}-\frac{1}{D(\mathbf{k}+\mathbf{l})}\right\}\left\{\frac{1}{D(\mathbf{k})}-\frac{1}{D(\mathbf{k}+\mathbf{l}')}\right\}\right\} \tag{4.43}$$

and for the longitudinal cross section

$$\frac{d\,\sigma_L^D}{d^2\mathbf{k}\,dz\,dt\,|\,t=0} = \frac{\alpha_{em}}{6\,\pi}\,\sum_f e_f^2\,\int\frac{d^2\mathbf{l}}{l^4}\,\int\frac{d^2\mathbf{l}'}{l'^4}\,\alpha_s f(x_{I\!P},l^2)\,\alpha_s f(x_{I\!P},l'^2) \tag{4.44}$$

$$\times\,4\,Q^2\,z^2(1-z)^2\,\left\{\frac{1}{D(\mathbf{k})}-\frac{1}{D(\mathbf{k}+\mathbf{l})}\right\}\left\{\frac{1}{D(\mathbf{k})}-\frac{1}{D(\mathbf{k}+\mathbf{l}')}\right\},$$

where $D(\mathbf{k}) = k^2 + z(1-z)Q^2 + m_f^2$. The four terms which arise after computing the products under the integral correspond to four possible ways in which the two gluons couple to the $q\bar{q}$ pair. Such couplings are necessary for gauge invariance and finiteness of the cross sections integrated over $\mathbf{k}$.

Notice that we use the same unintegrated gluon distribution function $f(x_{I\!P})$ as in the inclusive case, now taken at $x_{I\!P}$ instead of at Bjorken-$x$. In general this function should depend on the gluon longitudinal momentum fractions $f(x_1, x_2, l^2)$ where $x_{I\!P} = x_1 - x_2$. In the high energy limit, however, when the leading powers of $\log(1/x)$ are taken into account, the asymmetry $x_1 \neq x_2$ can be neglected and the indicated approximation is legitimate. The role of this asymmetry for high-$p_\perp$ jet photoproduction was analyzed in [143] with the help of the off diagonal parton distributions [144, 145, 146].

Eqs. (4.43) and (4.44) can be easily rewritten in the dipole representation, using relations (B.1) and (B.3) from Appendix B. After some rearrangements

we obtain

$$\frac{d\,\sigma_T^D}{d^2\mathbf{k}\,dz\,dt\,|\,t=0} = \frac{3\alpha_{em}}{32\,\pi^3}\,\sum_f e_f^2 \int \frac{d^2\mathbf{r}_1}{2\pi}\,\frac{d^2\mathbf{r}_2}{2\pi}\,\hat{\sigma}(x_{I\!P},\mathbf{r}_1)\,\hat{\sigma}(x_{I\!P},\mathbf{r}_2)\,e^{\mathbf{k}\cdot(\mathbf{r}_1-\mathbf{r}_2)}$$

$$\times\left\{[z^2+(1-z)^2]\,\frac{\mathbf{r}_1\cdot\mathbf{r}_2}{r_1\;r_2}\,\overline{Q}^2\;K_1(\overline{Q}r_1)\,K_1(\overline{Q}r_2)\;+\;m_f^2\;K_0(\overline{Q}r_1)\,K_0(\overline{Q}r_2)\right\} \tag{4.45}$$

and

$$\frac{d\,\sigma_L^D}{d^2\mathbf{k}\,dz\,dt\,|\,t=0} = \frac{3\alpha_{em}}{32\,\pi^3}\,\sum_f e_f^2\;\int \frac{d^2\mathbf{r}_1}{2\pi}\,\frac{d^2\mathbf{r}_2}{2\pi}\,\hat{\sigma}(x_{I\!P},\mathbf{r}_1)\,\hat{\sigma}(x_{I\!P},\mathbf{r}_2)\,e^{\mathbf{k}\cdot(\mathbf{r}_1-\mathbf{r}_2)}$$

$$\times\,4\,Q^2\,z^2\,(1-z)^2\;K_0(\overline{Q}r_1)\,K_0(\overline{Q}r_2)\,, \tag{4.46}$$

where $\overline{Q}^2 = z(1-z)Q^2 + m_f^2$. The inclusive diffractive cross section (at $t=0$) is obtained after the integration over momenta of the final state quarks

$$\frac{d\,\sigma_{T,L}^D}{dt}_{|\,t=0} = \int d^2\mathbf{k}\;dz\;\frac{d\,\sigma_{T,L}^D}{d^2\mathbf{k}\,dz\,dt\,|\,t=0}\,. \tag{4.47}$$

It has a remarkably simple form in the dipole representation. When the integration over $\mathbf{k}$ in (4.46) is done, we obtain the delta function $\delta(\mathbf{r}_1-\mathbf{r}_2)$ which allows to perform one of the two integrations over $\mathbf{r}$. Thus we find the following result

$$\frac{d\,\sigma_{T,L}^D}{dt}_{|\,t=0} = \frac{1}{16\,\pi}\int d^2\mathbf{r}\,dz\;\sum_f\;|\Psi_{T,L}^f(\mathbf{r},z)|^2\;\hat{\sigma}^2(x,\mathbf{r})\,, \tag{4.48}$$

where $\Psi_{T,L}^f$ is the photon wave function which appears in the inclusive DIS cross section (3.7). Notice that the dipole cross section appears squared in the diffractive cross section. In order to obtain (4.48) we changed the argument in $\hat{\sigma}$ from $x_{I\!P}$ to $x$ during the $\mathbf{k}$-integration. It is legitimate in the high energy approach as long as the dominant contribution is not concentrated at small $\beta = x/x_{I\!P}$. As we will see, this is the case for the diffractive $q\bar{q}$ production.

The formula (4.48) is a realization of the old idea of Good and Walker [147] (see also [148]) that diffraction occurs due to different absorption of the interaction matrix eigenstates. In the small-$x$ DIS case these are the $q\bar{q}$ dipoles with definite $\mathbf{r}$ and $z$. The projectile, the virtual photon in our case, is a superposition of these states each of which is elastically scattered with different probability.

The total diffractive cross sections are obtained after an additional integration over $t$. Assuming a factorizable exponential dependence on $t$ with the diffractive slope $B_D$, we have

$$\sigma_{T,L}^D \;=\; \int_{-\infty}^{0} dt\;e^{B_D t}\;\frac{d\,\sigma_{T,L}^D}{dt}_{|\,t=0} \;=\; \frac{1}{B_D}\,\frac{d\,\sigma_{T,L}^D}{dt}_{|\,t=0}\,. \tag{4.49}$$

### 4.3.2 Saturation and DIS diffraction

DIS diffraction is a good test of the saturation model. The three parameters of this model were obtained from the fit to inclusive small $x$ data. Determined in this way the dipole cross section has been applied to eqs. (4.45) and (4.46) in the region of moderate values of $\beta$ where the $q\bar{q}$ component of the diffractive final state dominates. For small values of $\beta$ the $q\bar{q}g$ state should additionally be considered. The result is a very good description of diffractive data form HERA, see [95].

The idea that the dipole cross section saturates with the $x$-dependant radius is particularly important for diffraction. It allows to explain in a natural way the constant ratio $\sigma^D/\sigma^{inc}$ as a function of $x$ and $Q^2$ which is observed at HERA. As a consequence, the diffractive cross section has the same leading twist behaviour and energy dependence as the inclusive DIS cross section. To prove these results, let us perform the qualitative analysis of the transverse cross section (4.48), using the approximate formula (3.15) with the squared dipole cross section (3.21).

In the scaling region, $Q^2 \gg 1/R_0^2$, we find for transverse photons

$$\sigma_T^D \sim \underbrace{\int_0^{4/Q^2} \frac{dr^2}{r^2}\left(\frac{\sigma_0\, r^2}{4R_0^2}\right)^2}_{symmetric} + \underbrace{\int_{4/Q^2}^{4R_0^2} \frac{dr^2}{r^2}\left(\frac{1}{Q^2r^2}\right)\left(\frac{\sigma_0\, r^2}{4R_0^2}\right)^2}_{aligned\ jet} + \underbrace{\int_{4R_0^2}^{\infty} \frac{dr^2}{r^2}\left(\frac{1}{Q^2r^2}\right)\sigma_0^2}_{aligned\ jet}$$

which after the integration gives the following leading contributions

$$\sigma_T^D \sim \underbrace{\frac{\sigma_0^2}{Q^4R_0^4}}_{r<2/Q} + \underbrace{\frac{\sigma_0^2}{Q^2R_0^2}}_{2/Q<r<2R_0} + \underbrace{\frac{\sigma_0^2}{Q^2R_0^2}}_{r>2R_0}. \tag{4.50}$$

Notice that in contrast to inclusive DIS cross section (3.23), the leading twist-2 result comes only from aligned jet configuration. The symmetric contribution is higher twist. Therefore, the *perturbative contribution is largely suppressed in diffractive* DIS. This situation is illustrated in Fig. 4.7 where we show the distribution $d\sigma_T/dr$ for inclusive (3.7) and diffractive (4.48) cross sections. The suppression of the contribution with $r < 2/Q$ for diffractive dissociation (DD) is clearly visible.

In DIS diffraction the proton structure is probed with a large $q\bar{q}$ probe, and the corresponding sizes $r$ are in the saturation region of the dipole cross section (3.18). The fact that diffraction has a significant soft component ($r \gg 2R_0$) is to be expected. Here we find that the semi-hard region $2/Q < r < 2R_0$ significantly contributes (detailed analysis gives around 50%). This shows that DIS diffraction is ideally suited to study the transition from 'soft' to 'hard' physics.

The analysis performed for the longitudinal cross section gives a higher twist

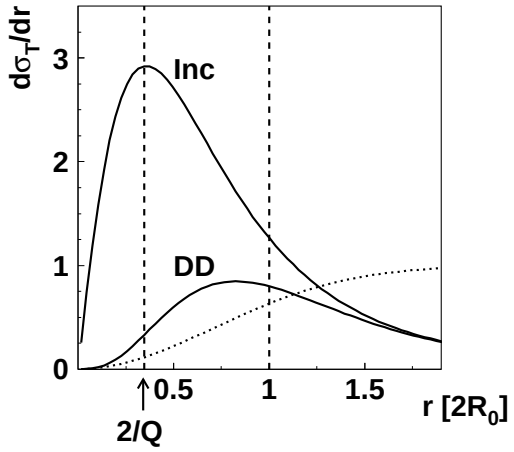


Figure 4.7: *The distribution $d\sigma_T/dr$ (solid lines) for inclusive (Inc) and diffractive (DD) cross sections at $Q^2 = 10$ GeV$^2$ and $x = 10^{-4}$. The dipole cross section is shown by the dotted line. The $r$-axis is in units of $2R_0(x) = 0.37$ fm.*

contribution for all sizes $r$

$$\sigma_L^D \sim \underbrace{\frac{\sigma_0^2}{Q^4 R_0^4}}_{r<2/Q} + \underbrace{\frac{\sigma_0^2}{Q^4 R_0^4}\log(Q^2 R_0^2)}_{2/Q<r<2R_0} + \underbrace{\frac{\sigma_0^2}{Q^4 R_0^4}}_{r>2r_0} . \tag{4.51}$$

The intermediate (semi-hard) region, however, is logarithmically enhanced.

From the comparison of the leading behaviour of (4.50) and the inclusive cross section (3.23), we obtain for the ratio

$$\frac{\sigma^D}{\sigma^{inc}} \sim \frac{1}{\log(Q^2 R_0^2(x))} , \tag{4.52}$$

which is a slowly varying function of $x$ and $Q^2$. A more detailed analysis based on the Mellin representation gives the following result [94]

$$\frac{\sigma^D}{\sigma^{inc}} = \frac{\sigma_0}{8\pi B_D}\,\frac{\log(2)}{\log(Q^2 R_0^2) + \gamma_E + 1/6} . \tag{4.53}$$

Substituting the fitted values of the parameters we obtain the result of the order of 10% which agrees quite well with the measured value. A more refined comparison is presented in Fig. 4.8, reproduced from [95], where the flat ratio for different values of diffractive mass $M_X$ is found as a function of $\gamma^* p$ center-of-mass energy $W$.

The role of the $x$-dependant saturation can be better understood if we assume that the dipole cross section (3.21) takes the form

$$\hat{\sigma}(x,r) = \begin{cases} \sigma_0\, r^2/4R_0^2(x) & \text{for} \quad r \le 2R_{cut} \\ \sigma_0\, R_{cut}^2/R_0^2(x) & \text{for} \quad r > 2R_{cut} , \end{cases} \tag{4.54}$$

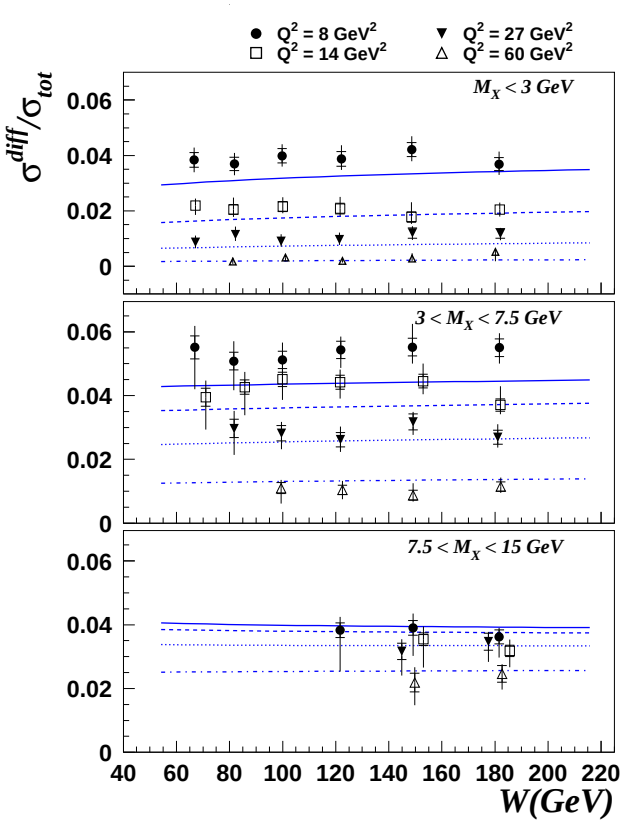


Figure 4.8: *The ratio of the diffractive and inclusive cross sections as a function of $W$ for different values of $Q^2$ and diffractive mass $M_X$. The data are from ZEUS [87].*

where $R_{cut} \sim 1/\Lambda_{QCD} \gg 1/Q$ is *$x$-independent* infrared scale which replaces the saturation scale $R_0(x)$ as the separator between perturbative and nonperturbative domains. Notice that (4.54) violates unitarity when $x \to 0$. Computing the leading contribution for both inclusive and diffractive cross sections from relation (3.15), we find

$$\sigma^{inc} \sim \frac{\sigma_0}{Q^2 R_0^2(x)} \log(Q^2 R_{cut}^2) \tag{4.55}$$

$$\sigma^{D} \sim \frac{\sigma_0^2}{Q^2 R_0^2(x)} \frac{R_{cut}^2}{R_0^2(x)} . \tag{4.56}$$

Thus the ratio $\sigma^D/\sigma^{inc}$ would be proportional to $1/R_0^2(x) \sim x^{-\lambda}$, which contradicts the results from HERA. Therefore, the $x$-dependant saturation radius $R_0(x)$ may be viewed as an effective cutoff leading to the constant ratio of the two cross sections as a function of $x$.

The comparison of the predictions based on the form (3.18) of the dipole cross sections with DIS diffraction data is shown in Fig. 4.9. No further parameters were introduced in addition to those fixed in the inclusive DIS analysis.

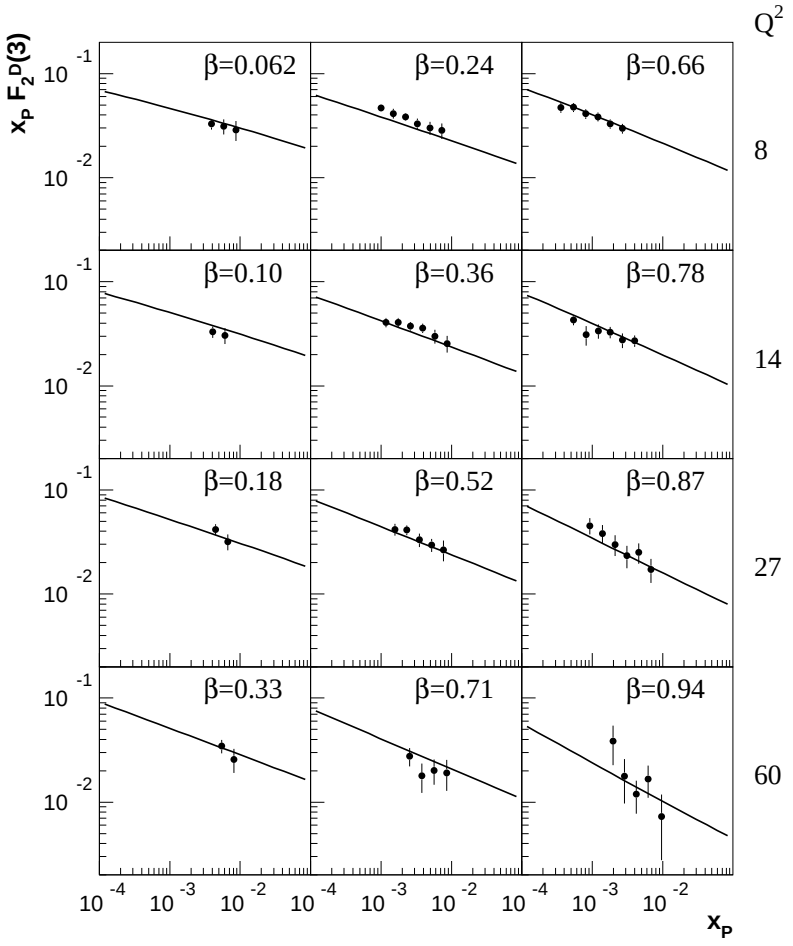


Figure 4.9: *The diffractive structure functions $x_{I\!P} F_2^{D(3)}(\beta, Q^2, x_{I\!P})$ as a function of $x_{I\!P}$ for different values of $\beta$ and $Q^2$ (in units of $GeV^2$). The data are from ZEUS [87].*

Notice the agreement with both the normalization and the $x_{I\!P}$-dependence of the measured structure functions. For this comparison, the $q\bar{q}$ and $q\bar{q}g$ diffractive final states were considered[1]. The analytical formulae used in the presented analysis are given in the next sections where we also explain the significance of the $q\bar{q}$ and $q\bar{q}g$ contributions for the total diffractive cross section.

### 4.3.3 Diffractive mass spectrum

So far we have been interested in the inclusive description of diffractive DIS. Now, we want to look at these processes more exclusively. The most natural question is how the diffractive cross sections depend on mass $M$ of the diffractive system. In the case of the $q\bar{q}$ pair, which form the diffractive system, the answer is encoded in eqs. (4.45) and (4.46). We write them again assuming that the

[1] The $q\bar{q}g$ final state is discussed in detail in Section 4.3.5.

dipole cross section is spherically symmetric, $\hat{\sigma}(\mathbf{r}) = \hat{\sigma}(r)$.

In this case the angular integration with respect to the angles between $\mathbf{k}$ and $\mathbf{r}_1$, $\mathbf{r}_2$ can be performed with the help of the relation (B.5) from Appendix B. Thus we obtain

$$\frac{d\,\sigma_T^D}{d^2\mathbf{k}\,dz\,dt\,|\,t=0} = \frac{3\alpha_{em}}{32\pi^3}\sum_f e_f^2\,\left\{[z^2+(1-z)^2]\,\overline{Q}^2\,\phi_1^2(k,z) + m_f^2\,\phi_0^2(k,z)\,,\right\} \tag{4.57}$$

$$\frac{d\,\sigma_L^D}{d^2\mathbf{k}\,dz\,dt\,|\,t=0} = \frac{3\alpha_{em}}{32\,\pi^3}\sum_f e_f^2\,4\,Q^2\,z^2\,(1-z)^2\,\phi_0^2(k,z)\,, \tag{4.58}$$

where the "impact factors"

$$\phi_i(k,z) = \int_0^\infty dr\,r\,K_i(\overline{Q}r)\,J_i(kr)\,\hat{\sigma}(x_{I\!P},r) \tag{4.59}$$

for $i = 0, 1$. Let us recall that $\overline{Q}^2 = z(1-z)Q^2 + m_f^2$, and $K_i$ and $J_i$ are the Bessel functions.

The diffractive mass spectrum of the $q\bar{q}$ pair is found after integrating over the final state quark momenta corresponding to a diffractive mass $M$, eq. (4.40)), and over $t$ according to (4.49). Thus we have

$$\frac{d\sigma_{T,L}^D}{dM^2} = \int d^2\mathbf{k}\;dz\;\delta\left(M^2 - \frac{k^2+m_f^2}{z(1-z)}\right)\;\frac{1}{B_D}\;\frac{d\,\sigma_{T,L}^D}{d^2\mathbf{k}\,dz\,dt\,|\,t=0}\,. \tag{4.60}$$

It is easy to check that after the integration of the above relation over $M^2$, the total diffractive cross sections (4.49) are obtained.

The diffractive structure functions (4.10) are directly related to the diffractive cross sections. From relation (4.11) we easily find the general relation

$$x_{I\!P}F_{T,L}^{D(3)}(\beta,Q^2,x_{I\!P}) = \frac{1}{4\pi^2\alpha_{em}}\,\frac{Q^4}{\beta}\,\frac{d\sigma_{T,L}^D}{dM^2}\,, \tag{4.61}$$

where we switch to $\beta = Q^2/(Q^2+M^2)$ as an independent variable which is an analogue of the Bjorken-$x$ for DIS diffraction. The presented formulae can be used for numerical analysis with the dipole cross section given by the saturation model, see the comparison with the data in Fig. 4.9. It is instructive, however, to try to analyze them analytically.

### 4.3.4 Mass spectrum in certain limits

We can analyze the derived formulae analytically in certain limits of the diffractive mass $M$. For this purpose we perform the integration over $\mathbf{k}$ in (4.60) to find

$$\frac{d\sigma_{T,L}^D}{dM^2} = 2\pi\int_{z_{min}}^{1/2} dz\;z(1-z)\;\frac{1}{B_D}\;\frac{d\,\sigma_{T,L}^D}{d^2\mathbf{k}\,dz\,dt\,|\,t=0}\,, \tag{4.62}$$

where $z_{min} = (1 - \sqrt{1 - 4m_f^2/M^2})/2$ and $k^2 = z(1-z)M^2 - m_f^2$ on the r.h.s of (4.62). If, for simplicity, we set $m_f = 0$, we arrive at the final formulae which will serve as the starting point for the analysis presented in this section

$$\frac{d\sigma_T^D}{dM^2} = \frac{3\,\alpha_{em}}{32\,\pi^2 B_D} \sum_f e_f^2 \;\; Q^2 \int_0^1 dz\; z^2(1-z)^2\; [z^2 + (1-z)^2]\; \phi_1^2(z)\;, \quad (4.63)$$

$$\frac{d\sigma_L^D}{dM^2} = \frac{3\,\alpha_{em}}{32\,\pi^2 B_D} \sum_f e_f^2 \;\; Q^2 \int_0^1 dz\; z^3(1-z)^3\; \phi_0^2(z)\;, \quad (4.64)$$

where the impact factors (4.59) take the form

$$\phi_{0,1}(z) = \int_0^\infty dr\, r\, K_{0,1}\Big(\sqrt{z(1-z)}\, Qr\Big)\; J_{0,1}\Big(\sqrt{z(1-z)}\, Mr\Big)\; \hat{\sigma}(x_{I\!P}, r)\,. \quad (4.65)$$

In the following we will discuss our results mainly in terms of the structure functions (4.61) which are related to the above cross sections by a simple multiplicative factor.

In the limit $M = 0$, only $\phi_0$ in eq. (4.65) has a nonzero value since $J_i(0) = \delta_{i0}$. Thus we expect that at the low mass edge of the spectrum, $M^2 \ll Q^2$ or $\beta \to 1$, the longitudinal contribution (although higher twist) dominates over the transverse one. Indeed, the analysis done for the saturation model in the spirit of the estimations from the previous sections, gives the following dominant contributions for $\beta \to 1$,

$$\begin{aligned} x_{I\!P} F_{Tqq}^{D(3)} &\sim \frac{\sigma_0^2}{B_D R_0^2(x_{I\!P})}\,(1-\beta)\,, \quad (4.66)\\ x_{I\!P} F_{Lqq}^{D(3)} &\sim \frac{\sigma_0^2}{B_D R_0^2(x_{I\!P})}\left(\frac{1}{Q^2 R_0^2}\right)\,. \end{aligned}$$

As expected, the longitudinal structure function is suppressed by the additional power of $1/Q^2$ but it dominates over $F_T^D$ when $\beta \approx 1$. Let us notice that the vanishing of $F_T^D$ at $\beta = 1$ is independent of the form of the dipole cross section.

It is interesting to note that the leading behaviour of the transverse cross section is given by aligned jet configuration ($z < 1/R_0^2 Q^2$) which involves large distances, $r \gg R_0$. In the small mass limit this component, as well as the whole transverse cross section, are strongly suppressed. For the longitudinal polarization, the symmetric configuration ($z \approx 1/2$) gives the main contribution. In such a case the large sizes are strongly suppressed, and the perturbative region $r \ll R_0$ mainly contributes to the cross section. This observations lead to the expectation that the diffractive cross section is nearly saturated by the production of the longitudinally polarized vector mesons in the limit $M^2 \ll Q^2$.

The same analysis performed for the saturation model in the triple Regge

limit, $M^2 \gg Q^2$ or $\beta \to 0$, gives to the following result

$$x_{I\!P} F_{Tqq}^{D(3)} \sim \frac{\sigma_0^2}{B_D R_0^2(x_{I\!P})}\,\beta\,, \tag{4.67}$$

$$x_{I\!P} F_{Lqq}^{D(3)} \sim \frac{\sigma_0^2}{B_D R_0^2(x_{I\!P})}\left(\frac{1}{Q^2 R_0^2}\right)\beta^3\,,$$

where now $\beta \approx Q^2/M^2$. Both contributions are due to aligned jet configuration ($z < 1/R_0^2 M^2$). The higher twist nature of $F_L^D$ for fixed $\beta$ and $x_{I\!P}$ is evident. This structure function is also suppressed stronger than the transverse one.

The fact that the structure functions (4.67) vanish when $\beta \to 0$ is independent of the the form of the dipole cross section, but depends on the photon wave function. The saturation model, however, provides the normalization (together with the diffractive slope $B_D$) and the dependence on energy ($x_{I\!P}$) which are essential elements for the comparison with data.

In terms of the cross sections, relations (4.67) look as follows

$$\frac{d\sigma_T^D}{dM^2} \sim \frac{1}{M^4} \qquad \text{and} \qquad \frac{d\sigma_L^D}{dM^2} \sim \frac{1}{M^8}\,, \tag{4.68}$$

in the limit $M^2 \to \infty$, for fixed $x_{I\!P}$ and $Q^2$. The experimental results from HERA, however, do not confirm such strong diffractive mass suppression. For $M^2 \gg Q^2$ the measured $d\sigma^D/dM^2 \sim 1/M^2$ which is a strong indication that we have to consider the next Fock state from the virtual photon wave function (4.1), the $q\bar{q}g$ state. Indeed, after considering this contribution in the configuration when the gluon is strongly separated from the $q\bar{q}$ pair in the **r**-space, we obtain agreement with the data. In terms of the diffractive structure function, the measured and computed $F_2^{D(3)}$ rises when $\beta \to 0$. Effectively (in the large $N_c$ limit) the new configuration may be viewed as the $gg$ dipole.

### 4.3.5 The $q\bar{q}g$ contribution

The detailed discussion of the $q\bar{q}g$ contribution is given in [129] and [95]. Here we only quote the final result in the dipole representation (see also eq. (23) in [95] for the representation with the unintegrated gluon distribution),

$$x_{I\!P} F_{q\bar{q}g}^{D(3)}(\beta, Q^2, x_{I\!P}) = \frac{81\beta}{256\pi^4 B_D} \sum_f e_f^2 \; \frac{\alpha_s}{2\pi} \int_\beta^1 \frac{dz}{z}\left[\left(1-\frac{\beta}{z}\right)^2 + \left(\frac{\beta}{z}\right)^2\right]$$

$$\times \frac{z}{(1-z)^3} \int_0^{(1-z)Q^2} dk^2 \, \log\left(\frac{(1-z)Q^2}{k^2}\right) \phi_2^2(k,z)\,, \tag{4.69}$$

where the new impact factor is given by

$$\phi_2(k,z) = k^2 \int_0^\infty dr\, r\, K_2\left(\sqrt{\frac{z}{1-z}}kr\right) J_2(kr)\,\hat{\sigma}(x_{I\!P}, r)\,. \tag{4.70}$$

The diffractive production from transverse photons is only considered. Notice that an additional gluon radiation is a higher in $\alpha_s$ correction. The variable

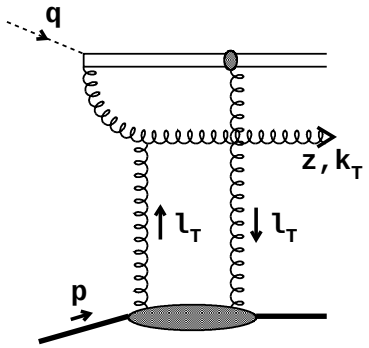


Figure 4.10: *Diffractive $q\bar{q}g$ production.*

$z$ describes the relative momentum fraction of the gluon with respect to the pomeron momentum $x_{I\!P}p$. The combination $k^2/(1-z)$ which enters the logarithm is its mean virtuality. The term in square brackets under the first integral is the Altarelli-Parisi splitting function $g \to qq$, which results from the approximation that the transverse momentum of the emitted gluon is smaller than the transverse momentum of the quark. In the impact parameter representation this corresponds to a large separation between the gluon and the $q\bar{q}$ pair.

In the triple Regge limit $\beta \to 0$, we obtain the following result

$$x_{I\!P}F_{q\bar{q}g}^{D(3)} \sim \frac{\sigma_0^2}{B_D R_0^2(x_{I\!P})}\,(1-\frac{3}{2}\beta)\,, \tag{4.71}$$

which gives the mass spectrum

$$\frac{d\sigma_T^D}{dM^2} \sim \frac{1}{M^2}\,. \tag{4.72}$$

Thus, although this is a higher in $\alpha_s$ correction, the process with a gluon radiated off in the $q\bar{q}g$ diffractive state dominates over the pure $q\bar{q}$ contribution in the large diffractive mass limit. For a small diffractive mass, $F_{qqg}^{D(3)}$ is strongly suppressed, and the $q\bar{q}$ contributions (4.66) is important. The presented results are supported by the exact numerical analysis, see [95] for details.

In summary, we have discussed the three contributions to the diffractive DIS, the $q\bar{q}$ pair from the transverse and longitudinal photon and the $q\bar{q}g$ system,

$$F_2^{D(3)} = F_{Tq\bar{q}}^{D(3)} + F_{Lq\bar{q}}^{D(3)} + F_{q\bar{q}g}^{D(3)}\,. \tag{4.73}$$

These contributions have distinct regions of $\beta$ in which they dominate. For $\beta \approx 1$ or $M^2 \ll Q^2$ the longitudinal $q\bar{q}$ component is the most important. In the intermediate range, $\beta \approx 1/2$ or $M^2 \approx Q^2$, the $q\bar{q}$ production from the transverse photon prevails. Finally, for $\beta \approx 0$ or $M^2 \gg Q^2$ the $q\bar{q}g$ production dominates. The three contributions are shown in Fig. 4.11, reproduced from [95]. Note very good agreement with data.

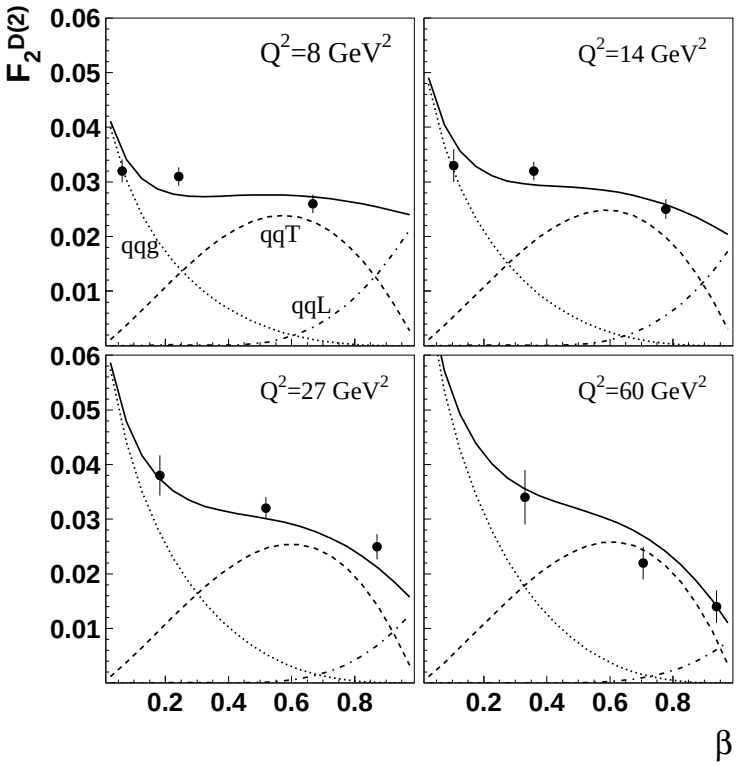


Figure 4.11: $F_2^{D(3)}(\beta, Q^2, x_{I\!P} = 0.0042)$ *as a function of* $\beta$ *(solid line). The dashed lines show* $F_{Tq\bar{q}}^{D(3)}$*, the dot-dashed lines correspond to* $F_{Lq\bar{q}}^{D(3)}$*, and the dotted lines illustrate* $F_{q\bar{q}g}^{D(3)}$*. The data are from the ZEUS collaboration [87].*

## 4.4 Diffractive parton distributions

The diffractive structure functions $F^{D(4)}$ were introduced in Section 4.1 in a full analogy to the inclusive DIS case. They characterize the hadronic tensor for diffractive DIS: $W_{\mu\nu} = W_{\mu\nu}(p, p', q)$

$$W_{\mu\nu} = \frac{1}{4\pi} \sum_X < p|J_\nu^{em}(0)|p'X >< p'X|J_\mu^{em}(0)|p > \ (2\pi)^4 \ \delta^4(p - p' - p_X)$$

$$= \left(-g_{\mu\nu} + \frac{q_\mu q_\nu}{q^2}\right) F_1^{D(4)} \ + \ \frac{1}{p\cdot q}\left(p_\mu - q_\mu \frac{p\cdot q}{q^2}\right)\left(p_\nu - q_\nu \frac{p\cdot q}{q^2}\right) F_2^{D(4)} \, .$$

Notice the difference to the inclusive hadronic tensor (2.6). In the summation over the final states only those with loosely scattered incident proton are retained. Thus, the final states in the diffractive hadronic tensor consist of the scattered proton $p'$ and the diffractive system $X$ over which the summation is performed. This introduces two variables $(x_{I\!P}, t)$, defined in Section 4.1, in addition to those known from the inclusive case $(x, Q^2)$.

The momentum $p'$ of the scattered proton can also be used to build the tensor structure of the hadronic tensor (4.74). It is not necessary, however, as long as the azimuthal angle of the scattered proton is not measured [124]. Thus only two structure functions are needed to characterize the hadronic tensor:

$$F_i^{D(4)} \;=\; F_i^{D(4)}(x, Q^2, x_{I\!P}, t)\;, \tag{4.74}$$

where $i = 1, 2$. In the following we will be interested in the structure functions integrated over $t$, $F_i^{D(3)}(\beta, Q^2, x_{I\!P})$, see eq. (4.61). The structure functions (4.74) are identical to those in Section 4.1.

As in inclusive DIS, the diffractive structure functions are decomposed into the leading and higher twist contributions

$$F_i^{D(3)}(\beta, Q^2, x_{I\!P}) \;=\; F_i^{D(3)LT}(\beta, Q^2, x_{I\!P}) + \frac{F_i^{D(3)HT}(\beta, Q^2, x_{I\!P})}{Q^2} + \ldots\,. \tag{4.75}$$

The leading twist part is related to *diffractive parton distributions* (DPD) [149, 150, 151, 152] in analogy to inclusive DIS

$$F_2^{D(3)LT}(\beta, Q^2, x_{I\!P}) \;=\; \sum_f e_f^2\;\beta\left\{q_f^D(\beta, Q^2, x_{I\!P}) \;+\; \bar{q}_f^D(\beta, Q^2, x_{I\!P})\right\}\;, \tag{4.76}$$

In addition to the diffractive quark distributions, $q_f^D$ and $\bar{q}_f^D$, the diffractive gluon distribution $g^D(\beta, Q^2, x_{I\!P})$ is defined. Usually, it is assumed that the quark and antiquark distributions are equal,

$$q_f^D(\beta, Q^2, x_{I\!P}) \;=\; \bar{q}_f^D(\beta, Q^2, x_{I\!P})\,, \tag{4.77}$$

to be in accord with the picture of the pomeron exchange with vacuum quantum numbers. All distributions obey the DGLAP evolution equations in which $x_{I\!P}$ is a parameter independent of the evolution.

The DPD have a probabilistic interpretation. They are conditional probabilities to find in a fast moving proton a parton with the momentum fraction $\beta$, under the condition that proton remains intact after the scattering losing a small fraction $x_{I\!P}$ of its momentum. The momentum fraction $\beta$ is defined with respect to the lost proton momentum $x_{I\!P}p$.

The possibility to define the diffractive parton distributions results from the proof that *collinear factorization* holds for diffractive DIS [153]. This allows to separate the leading twist contribution into short and long distance parts, and then absorb collinear singularities into the latter part. As a result the parton distributions acquire dependence on the scale, governed by the evolution equations.

In inclusive DIS parton distributions are universal, i.e. the same distributions can be used in the description of both lepton-hadron DIS and hadron-hadron hard reactions since collinear factorization is valid for the two processes. Collinear factorization, however, is violated in diffractive hadron-hadron scattering [154, 153]. Thus, unlike the inclusive scattering, the diffractive parton distributions are no universal quantities. They can safely be used, however, to

describe hard diffractive processes involving leptons. A systematic approach to diffractive parton distributions, based on quark and gluon operators, is given in [152, 133].

Discussing diffractive parton distributions, it is very important to distinguish between different types of factorization. Collinear factorization allows to define these distributions. The other factorization, called *Regge factorization*, is a hypothesis on a factorized form of DPD. Namely,

$$q_f^D(\beta, Q^2, x_{I\!P}) \;=\; f(x_{I\!P})\, q_f^{I\!P}(\beta, Q^2)\,. \tag{4.78}$$

The function $f(x_{I\!P})$ is common for both the quark and gluon DPD. If $f(x_{I\!P})$ is given by (4.13) (integrated over $t$) we arrive at the Ingelman–Schlein model. In this case $q_f^{I\!P}(\beta, Q^2)$ coincide with the pomeron parton distributions.

Let us emphasize that the issue of diffractive parton distributions is intimately related to the leading twist-2 contribution to diffractive structure functions. In particular, the assumption that the longitudinal structure function is leading twist, as in inclusive DIS, is not supported in the two-gluon exchange model. The leading twist vanishes and $F_L^D$ is twist-4 with the behaviour proportional to $1/Q^2$.

### 4.4.1 DPD in the saturation model

The diffractive parton distributions can be defined in the two-gluon exchange model. In order to find the quark distribution we have to extract the leading twist part from $F_T^{D(3)}$, eq. (4.61). The gluon distribution is extracted from $F_{q\bar{q}g}^{D(3)}$ given by (4.69). The longitudinal structure function $F_L^{D(3)}$, as higher twist, does not contribute to diffractive parton distributions.

In order to extract the quark DPD, we write $F_T^{D(3)}$, given by (4.61) with (4.62), in the form in which the $z$-integration is performed first. After that we find the following form of the transverse $q\bar{q}$ contribution in the limit $m_f = 0$,

$$x_{I\!P} F_{Tqq}^{D(3)} \;=\; \frac{3}{64\pi^4 B_D} \sum_f e_f^2\, \frac{\beta^2}{(1-\beta)^3} \int\limits_0^{Q^2(1-\beta)/4\beta} dk^2 \frac{1 - \dfrac{2\beta}{1-\beta}\dfrac{k^2}{Q^2}}{\sqrt{1 - \dfrac{4\beta}{1-\beta}\dfrac{k^2}{Q^2}}}\, \phi_1^2(k) \tag{4.79}$$

where now

$$\phi_1(k) \;=\; k^2 \int_0^\infty dr\, r\, K_1\!\left(\sqrt{\frac{\beta}{1-\beta}}kr\right) J_1(kr)\, \hat{\sigma}(x_{I\!P}, r)\,. \tag{4.80}$$

The leading twist part of (4.79) is obtained by neglecting the powers $k^2/Q^2$ under the integral and integrating over $k^2$ up to infinity. Strictly speaking, energy conservation is violated in such a case, but the corrections are of the higher twist nature. With the new limit the integral is finite and we can write

the leading twist part of (4.79) as

$$F_{Tqq}^{D(3)LT} \;=\; 2\sum_f e_f^2\;\beta\, q_f^D(\beta, x_{I\!P})\;, \tag{4.81}$$

where the diffractive quark distribution is given by

$$q_f^D(\beta, x_{I\!P}) \;=\; \frac{3}{128\pi^4 B_D\, x_{I\!P}}\;\frac{\beta}{(1-\beta)^3}\;\int_0^\infty dk^2\;\phi_1^2(k,\beta,x_{I\!P})\;, \tag{4.82}$$

for any flavour $f$. Notice a lack of the factorization scale $\mu^2 = Q^2$ on the right hand side of (4.81). This may be viewed as a consequence of not having included ultraviolet divergent corrections which would require a cutoff. With those corrections the parton distributions become $\mu^2$-dependent and evolution would relate the distributions at different $Q^2$ values. However, we may use $q_f^D(\beta)$ as input distributions for the Altarelli-Parisi evolution with an initial scale related to the physics involved, e.g. $\mu^2 = 1/R_0^2(x_{I\!P})$ for the saturation model. Of course, the choice of the initial scale introduces an uncertainty for the prediction. As we will see in the next subsection, the $x_{I\!P}$ dependence in (4.82) factorizes and does not influence the evolution.

The gluon distribution can be found from (4.69). In the calculation of this contribution it was assumed that the transverse momenta or virtualities of the quark and the gluon are strongly ordered. In this approximation the integration over the transverse momentum of the quark loop gives a logarithmic contribution which has a natural lower cutoff, the virtuality of the gluon. At the same time the virtuality of the gluon should not exceed $Q^2$. This is the origin of the logarithmic term in (4.69). Collinear factorization means that we can pull that logarithm out of the integral over the gluon transverse momenta, and add to it an arbitrary scale $Q_0^2$. Thus we can write (4.69) in the following form (we set $z = \tilde{\beta}$ there)

$$F_{g\bar{g}g}^{D(3)LT} = 2\sum_f e_f^2\,\beta\,\frac{\alpha_s}{2\pi}\,\log\frac{Q^2}{Q_0^2}\int_\beta^1 \frac{d\tilde{\beta}}{\tilde{\beta}}\,\frac{1}{2}\left[\left(1-\frac{\beta}{\tilde{\beta}}\right)^2+\left(\frac{\beta}{\tilde{\beta}}\right)^2\right]\,g^D(\tilde{\beta}, x_{I\!P}) \tag{4.83}$$

where the diffractive gluon distribution is given by

$$g^D(\beta, x_{I\!P}) \;=\; \frac{81}{256\pi^4 B_D\, x_{I\!P}}\;\frac{\beta}{(1-\beta)^3}\;\int_0^\infty dk^2\;\phi_2^2(k,\beta,x_{I\!P}) \tag{4.84}$$

and $\phi_2$ is given by eq. (4.70). As in the case of the quark distribution (4.82), the found gluon distribution does not depend on $Q^2$, and serves as the initial distributions at some fixed scale $Q_0^2$.

The motivation for the above identification of the diffractive gluon distributions is the structure in the curly brackets on the r.h.s of eq. (4.83). It is identical to the structure resulting from the DGLAP evolution with one splitting of the gluon into the $q\bar{q}$ pair.

The combined initial parton distributions (4.82) and (4.84), depicted in Fig.4.12, allow complete description of the leading twist part of diffractive

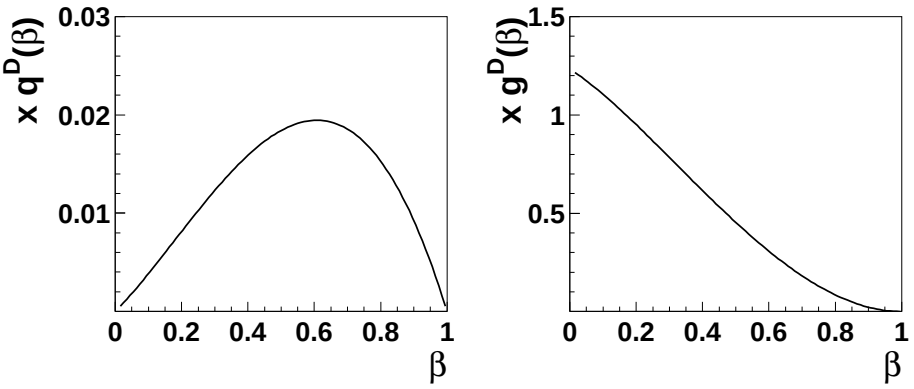


Figure 4.12: The diffractive quark distribution (4.82) and the gluon distribution (4.84) (multiplied by $x = x_{I\!P}\,\beta$) from the saturation model as a function of $\beta$ for $x_{I\!P} = 0.0042$ at the initial scale $Q_0^2$.

DIS. They serve as the initial conditions for the DGLAP evolution equations. DGLAP evolution in this case means that the diffractive system becomes more complicated due to additional parton emissions.

The longitudinal, higher twist contribution requires a separate treatment. It becomes important for large values of $\beta$, where the $q\bar{q}$ and the $q\bar{q}g$ production from transverse photons is negligible. Thus we add this contribution to the evolved leading twist part. The complete expression of the structure function reads

$$F_2^{D(3)} \;=\; F_2^{D(3)(LT)} \;+\; F_{q\bar{q}}^{L}\,. \tag{4.85}$$

where $F_2^{D(3)LT}$ is given by

$$F_2^{D(3)(LT)} \;=\; 2\sum_f e_f^2\;\beta\,q^D(\beta,Q^2,x_{I\!P})\,, \tag{4.86}$$

with the full DGLAP evolution. The longitudinal structure function $F_{q\bar{q}}^{L}$ is found using relations (4.61) and (4.62) in which the integration over $z$ is done

$$F_{q\bar{q}}^{L} \;=\; \frac{3}{16\pi^4 B_D\,x_{I\!P}}\sum_f e_f^2\,\frac{\beta^3}{(1-\beta)^4}\int_0^{\frac{Q^2(1-\beta)}{4\beta}} dk^2\,\frac{k^2/Q^2}{\sqrt{1-\dfrac{4\beta}{1-\beta}\dfrac{k^2}{Q^2}}}\;\phi_0^2(k)\,, \tag{4.87}$$

with $\phi_0$ defined as in eq. (4.80) with the Bessel functions $K_1, J_1$ replaced by $K_0, J_0$. From the above expression we see that $F_{q\bar{q}}^{L}$ is one power down in $Q^2$ with respect to the transverse counterpart $F_{q\bar{q}}^{T}$, see eq. (4.79), being higher twist contribution.

In summary, Eqs. (4.82) and (4.84) may serve as initial conditions for the evolution equations in the analysis of diffractive DIS with the diffractive structure function given by (4.85). For the comparison with the data see [155].

### 4.4.2 Regge factorization

The scaling property of the dipole cross section, i.e. that $\hat{\sigma}$ is a function of the dimensionless ratio $r/R_0(x)$, has the remarkable consequence for the $x_{I\!P}$-dependent of the found diffractive parton distributions.

Introducing the dimensionless variables $\hat{k} = kR_0(x)$ and $\hat{r} = r/R_0(x)$ in (4.82) and (4.84), and assuming $Q_0^2$ to be a fixed scale, we find the following factorization

$$q_f^D(\beta, x_{I\!P}) = \frac{1}{x_{I\!P} R_0^2(x_{I\!P})}\, q_f^{I\!P}(\beta)\,, \tag{4.88}$$

$$g^D(\beta, x_{I\!P}) = \frac{1}{x_{I\!P} R_0^2(x_{I\!P})}\, g^{I\!P}(\beta)\,. \tag{4.89}$$

We have introduced a notation similar to that in (4.16) for the $\beta$-dependent factors. This type of factorization is similar to Regge factorization but in fact has no connection with Regge theory. It merely results from the scaling properties of the saturating cross section $\hat{\sigma}$. Since the evolution does not affect the $x_{I\!P}$-dependence of the DPD, the factorized form will be valid for any scale $Q^2$.

Now, we can rewrite eq. (4.86) as

$$F_2^{D(3)(LT)} = \frac{1}{x_{I\!P} R_0^2(x_{I\!P})}\, 2 \sum_f e_f^2\ \beta\, q_f^{I\!P}(\beta, Q^2) \tag{4.90}$$

in which the $x_{I\!P}$-dependence is factored out. The $Q^2$-dependence of the distributions $q_f^{I\!P}$ is introduced by the evolution equations.

In the saturation model the parameter $\lambda = 0.29$ in the relation $R_0(x) \sim x^{\lambda/2}$ was determined from a fit to inclusive DIS data only [94]. The same value holds for diffractive interactions, thus we find a definite prediction for the $x_{I\!P}$-dependence of the leading twist diffractive structure function

$$F_2^{D(3)(LT)} \sim x_{I\!P}^{-1-\lambda}\,. \tag{4.91}$$

At present, the bulk of diffractive data in DIS support the factorized form (4.91). They are usually interpreted [86, 87] in terms of the $t$-averaged pomeron intercept $\overline{\alpha_{I\!P}}$, i.e.

$$F_2^{D(3)} \sim x_{I\!P}^{1-2\,\overline{\alpha_{I\!P}}}\,. \tag{4.92}$$

Such a dependence has been introduced in the spirit of the Ingelman–Schlein model, with the $t$-integration performed, $F_2^{D(3)} \sim \int dt\, f(x_{I\!P}, t) \sim x_{I\!P}^{1-2\,\overline{\alpha_{I\!P}}}$. Thus, according to (4.91) and (4.92) we find

$$\overline{\alpha_{I\!P}} = \frac{\lambda}{2} + 1 \approx 1.15\,, \tag{4.93}$$

which is in remarkable agreement with the values found at HERA, $\overline{\alpha_{I\!P}} = \alpha_{I\!P}(0) - 0.03 = 1.17$ by H1 [86] and $\overline{\alpha_{I\!P}} = 1.13$ by ZEUS [87]. More detailed analysis, see [95], allows to predict $\overline{\alpha_{I\!P}} \equiv \alpha_{I\!P(eff)}$ as shown in Fig. 4.13 for the two values of the diffractive mass.

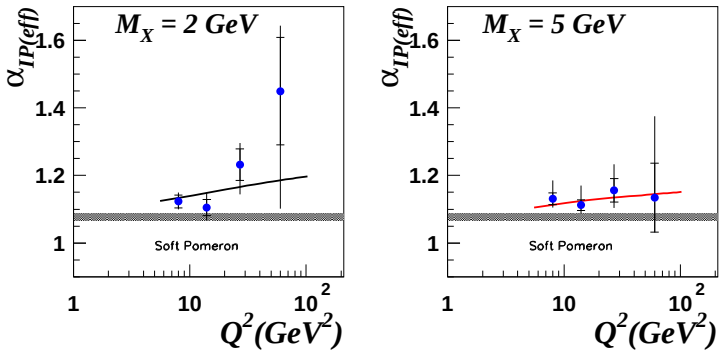


Figure 4.13: *The effective pomeron slope as predicted in the saturation model as a function of $Q^2$ for two values of the diffractive mass $M_X$. The data are from the ZEUS collaboration.*

$F_2^{D(3)}$ in the saturation model contains more than leading twist. This means that the dependence (4.91) is not generally valid. It is especially important for $\beta \to 1$, i.e. in the small diffractive mass region. From the analysis of Section 4.3.3 we know that the twist-4 longitudinal structure function dominates there. Thus the expected dependence on $x_{I\!P}$ for $\beta \approx 1$ is stronger than in the intermediate range of the diffractive mass $M^2 \sim Q^2$,

$$F_2^{D(3)} \approx F_L^{D(3)} \sim \frac{1}{x_{I\!P} R_0^4(x_{I\!P})} = x_{I\!P}^{-1-2\lambda} , \tag{4.94}$$

which clearly violates the universality of the effective pomeron intercept in different regions of diffractive mass. The first indication of that effect was indeed observed at HERA [87], and the saturation model gives a satisfactory explanation, see Fig. 4.13 and [95] for more details.

At this point we do not agree with the Ingelman–Schlein model in which a universal pomeron intercept behaviour resulting from Regge factorization is assumed. The lack of universal Regge factorization should be distinguished from the possible violation of the $x_{I\!P}$-factorization due to subleading reggeon exchanges [86], discussed in Section 4.2.2. This effect is not described by the saturation model, and is important for higher values of $x_{I\!P}$ than those considered in the high energy limit in which the analyzed formulae were derived.

The large twist-4 component also offers an alternative to the strongly concentrated at $\beta \approx 1$ gluon distribution, found in the purely leading twist DGLAP analysis of DIS diffraction [86].

Fig. 4.14 summarizes our studies of DIS diffraction based on the relation (4.73) with the saturation model for the dipole cross section. This figure should be compared to Fig. 4.5 in which the results from the model with the soft pomeron and reggeon exchanges were shown. We see that a good description of data is obtained with the saturation model, including the region of large $\beta$ (the two rightmost columns in Fig. 4.14).These results were obtained without tuning additional parameters to those found in the inclusive data analysis. Of course, the reggeon contribution cannot be described by the saturation model.

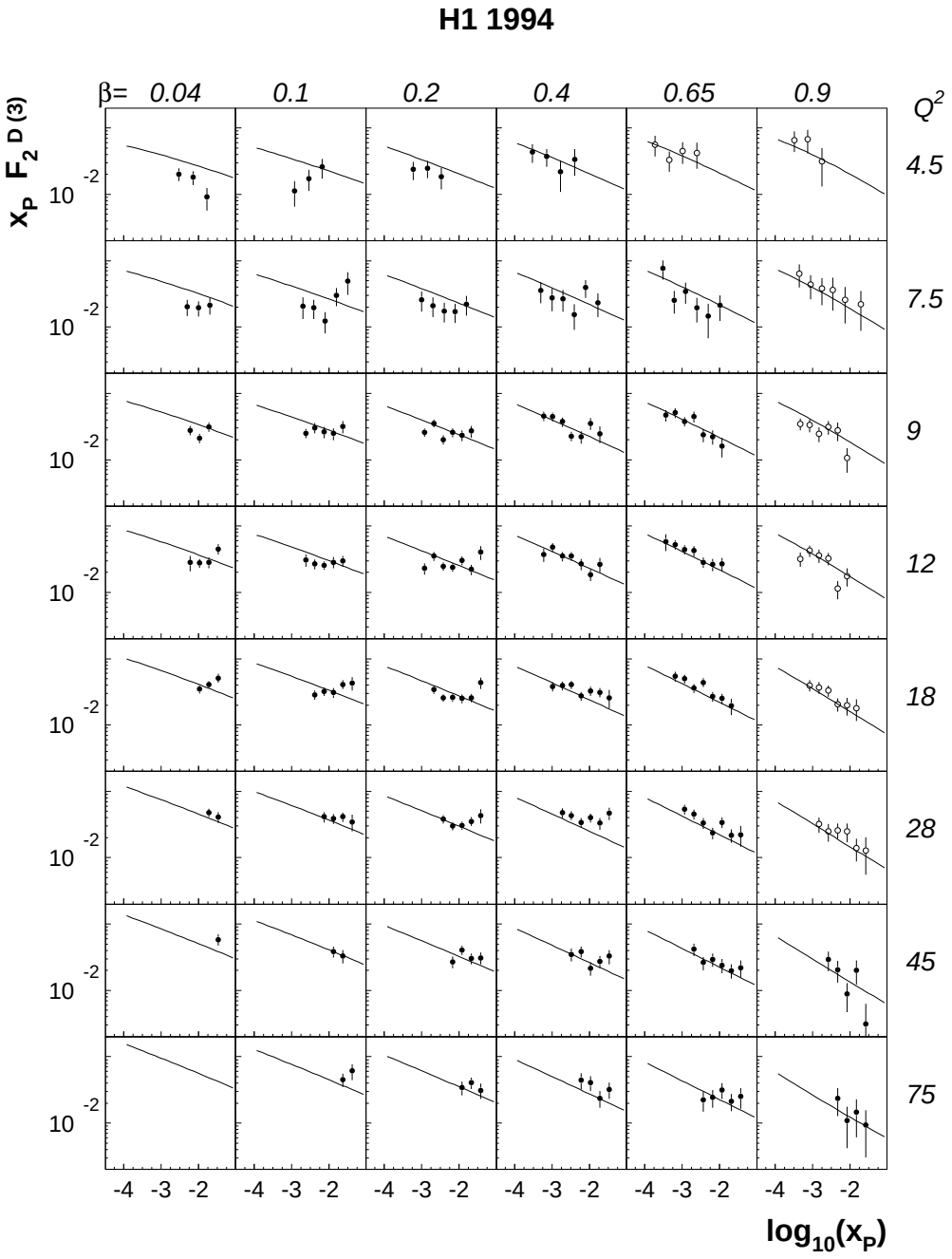


Figure 4.14: *The comparison, as in Fig. 4.5, of the results from the analysis based on the saturation model with the H1 collaboration data.* $Q^2$ *values are in units of* $GeV^2$.

# Chapter 5

# Summary and outlook

In this dissertation we have presented a description of DIS at small $x$ which uses the ideas of parton saturation. The presentation is based on the ten published articles listed in Introduction.

Before the main results are discussed, the background material on deep inelastic scattering is provided in Chapter 2. This includes the standard description with the help of the QCD parton model with the DGLAP evolution equations [12, 13, 14] as well as the discussion of the small-$x$ limit of DIS. In this limit, the notion of a hard pomeron is introduced based on considerations leading to the BFKL equation [25]. This equation replaces the DGLAP evolution equations. Also a different factorization formula [25, 33] for the calculation of the nucleon structure functions exists at small $x$, which uses the unintegrated gluon structure function describing the hard (BFKL) pomeron. The structure functions in such a description strongly rise with decreasing $x$, thus they ultimately violate unitarity. The unitarization corrections which tame the strong rise are realized by considering additional interactions between gluons in the nucleon. This mechanism leads to a picture of parton saturation in which the gluons form a strongly correlated system [39]. In this case the linear DGLAP or BFKL evolution equations are modified by nonlinear terms. The precise form of these corrections is still under the investigation.

The current experiments on small-$x$ DIS performed at HERA call for answering the question about the role of parton saturation (unitarization) effects for the measured processes. We have analyzed this problem in the dipole picture of inclusive DIS at small $x$ in Chapter 3. In this picture the unitarity conditions are naturally formulated. The main element of the description is the phenomenological parameterization of the dipole–proton cross section which incorporates the main features of parton saturation [94]. The three parameters of such a model are determined from a fit to all available data on lepton-proton scattering at small $x < 0.01$. In the discussed approach a good description of both the DIS data and the transition to low $Q^2$ region is obtained. By a careful analysis of the role of the light quark mass in the $q\bar{q}$ dipole, the photoproduction limit can formally be achieved with a good agreement with the data. The heavy flavour inclusive production in DIS is also analyzed. The saturation effects in the dipole-proton cross section parameterization are crucial for good

description of the data in a broad range of $Q^2$. They are also responsible for a new scaling law in inclusive $\sigma_{\gamma^* p}$ cross section at small $x$, which is predicted by the model and successfully confronted with the data [98]. The constructed description allows to study more formal aspect of the QCD based description of DIS such as the twist expansion of the structure function $F_2$ [99]. We provide an explanation for the observed in other analyses small size of the the higher twist corrections and estimate the region of validity of the twist expansion at small $x$.

A crucial test for the developed description is provided by diffractive processes in $ep$ DIS. In these processes the incoming proton stays intact after the scattering, losing a small fraction of its initial momentum. As we explained in detail in Chapter 4, the dipole picture with the saturation effects is very successful in providing explanation of DIS diffraction. In this case the process is viewed as elastic scattering of the $q\bar{q}$ or $gg$ dipole off the proton. The same dipole–proton cross section as in inclusive DIS can be used. Thus, we do not need to tune any further parameters. In this sense we obtain a unified formulation of inclusive and diffractive DIS with a very good agreement with the data [144]. The basic feature that diffractive DIS has the same dependence on $Q^2$ and $x$ as inclusive electroproduction is naturally explained in our approach due to the saturation features. This approach can be confronted to that which uses Regge theory with the concept of the soft pomeron and subleading reggeon exchanges [117, 114, 115, 120, 121]. The subleading reggeon exchanges cannot be described by the saturation model, but the soft pomeron aspect can be analyzed by looking at diffractive parton distributions [99]. We find Regge factorization property for them as the prediction of the saturation model with the correct energy dependence measured at HERA. In contrast, in the Regge approach these features are postulated. We also quantify the role of the twist-4 $q\bar{q}$ contribution from longitudinal photons for the description of the diffractive data at small values of the diffractive mass ($\beta \approx 1$). This contribution violates the universality of Regge factorization in the large $\beta$ region and also provides a natural alternative to the strongly concentrated at $\beta \approx 1$ diffractive gluon distribution found in the Regge based models.

The future work should be concentrated on the analysis of nonlinear unitarization corrections to the linear QCD evolution equations. The new equations are expected to provide the basis for the proposed parameterization of the dipole cross section. With respect to this program, the most promising is the analysis performed by Kovchegov [66, 67] after the saturation model was formulated. In this approach, the BFKL equation, formulated in the dipole representation, is generalized by taking into account multipomeron exchanges in the large $N_c$ limit. The resulting nonlinear equation has a solution which contains essential features of our parameterization of the dipole cross section. The future analysis will concentrate on the application of this formalism to description of the DIS data [156].

# Appendix A

# Solution to the BFKL equation

We are looking for the spherical symmetric solution of eq. (2.82) written for the dimensionless function

$$f(\omega, k_1, k_2) \equiv k_1^2 \, F(\omega, |\mathbf{k}_1|, |\mathbf{k}_2|, 0) \, . \tag{A.1}$$

After performing the angular integration in eq. (2.82) using

$$\int_0^{2\pi} \frac{d\phi}{(a - b\cos\phi)} = \frac{2\pi}{\sqrt{a^2 - b^2}} \tag{A.2}$$

for $a > b > 0$, the following spherically symmetric form of the BFKL equation is found

$$\begin{aligned} \omega f(\omega, k_1, k_2) &= k_1^2 \, \delta^2(\mathbf{k}_1 - \mathbf{k}_2) \qquad (A.3) \\ &+ \frac{N_c \alpha_s}{\pi} \int_0^\infty \frac{dk'^2}{k'^2} k_1^2 \left\{ \frac{f(\omega, k', k_2) - f(\omega, k_1, k_2)}{|k'^2 - k_1^2|} + \frac{f(\omega, k_1, k_2)}{\sqrt{4k'^4 + k_1^4}} \right\} . \end{aligned}$$

This equation can be diagonalized using the Mellin transform of $f$ with respect to $k_1$

$$\hat{f}(\omega, \gamma) = \int_0^\infty \frac{dk_1^2}{k_1^2} \left( \frac{k_1^2}{k_2^2} \right)^{-\gamma} f(\omega, k_1, k_2) \, , \tag{A.4}$$

where the inverse relation reads

$$f(\omega, k_1, k_2) = \frac{1}{2\pi i} \int_C d\gamma \left( \frac{k_1^2}{k_2^2} \right)^{\gamma} \hat{f}(\omega, \gamma) \tag{A.5}$$

and the integration contour $C$ is to be chosen to the right of all singularites of $\hat{f}(\omega, \gamma)$ in the $\gamma$-plane.

Integrating both sides of eq. (A.3) over $k_1^2$ with a factor as in (A.4), we find

$$\omega\hat{f}(\omega,\gamma) = \frac{1}{\pi} + \bar{\alpha}_s \int_0^\infty \frac{dk'^2}{k'^2} \int_0^\infty dk_1^2 \left(\frac{k_1^2}{k_2^2}\right)^{-\gamma} \left\{ \frac{f(\omega,k',k_2) - f(\omega,k_1,k_2)}{|k'^2 - k_1^2|} + \frac{f(\omega,k_1,k_2)}{\sqrt{4k'^4 + k_1^4}} \right\}, \tag{A.6}$$

where $\bar{\alpha}_s = N_c\alpha_s/\pi$. Now, we change the integration variable: $k'^2 \to v = k'^2/k_1^2$, and perform the integration over $k_1^2$ to obtain

$$\omega\hat{f}(\omega,\gamma) = \frac{1}{\pi} + \bar{\alpha}_s\mathcal{K}(\gamma)\ \hat{f}(\omega,\gamma)\,, \tag{A.7}$$

where $\mathcal{K}(\gamma)$ is the Lipatov kernel

$$\mathcal{K}(\gamma) = \int_0^\infty \frac{dv}{v}\left\{\frac{v^\gamma - 1}{|v-1|} + \frac{1}{\sqrt{4v^2+1}}\right\}$$

$$= 2\psi(1) - \psi(\gamma) - \psi(1-\gamma) \tag{A.8}$$

and $\psi(\gamma)$ is the digamma function. We use the following representation of $\psi(\gamma)$ to obtain the last equality, valid for $Re\ \gamma > 0$

$$\psi(\gamma) \equiv \frac{d}{d\gamma}\ln\Gamma(\gamma) = -\gamma_E - \int_0^1 dv\ \frac{v^{\gamma-1}-1}{1-v} \tag{A.9}$$

with $\gamma_E = -\psi(1) \approx 0.57721$ being Euler's constant. $K(\gamma)$ can be analytically continued onto the whole complex plane, except the points $\gamma = 0, \pm1, \pm2...$ where simple poles occur.
From (A.7) the solution in the $(\omega,\gamma)$-space can easily be found

$$\hat{f}(\omega,\gamma) = \frac{1/\pi}{\omega - \bar{\alpha}_s\mathcal{K}(\gamma)}\,. \tag{A.10}$$

The solution in the $(s,k)$-space,

$$\mathcal{F}(s,k_1,k_2,0) = \frac{1}{\pi k_1^2}\int_C \frac{d\gamma}{2\pi i}\left(\frac{k_1^2}{k_2^2}\right)^\gamma \int_{C'}\frac{d\omega}{2\pi i}\left(\frac{s}{s_0}\right)^\omega \frac{1}{\omega - \bar{\alpha}_s\mathcal{K}(\gamma)}\,, \tag{A.11}$$

is obtained using eq. (A.5) and the inverse Mellin transform,

$$\mathcal{F}(s,k_1,k_2,0) = \frac{1}{2\pi i}\int_{C'} d\omega\left(\frac{s}{s_0}\right)^\omega F(\omega,k_1,k_2,0)\,, \tag{A.12}$$

where the contour $C'$ is to the right of all $\omega$-plane singularities of $F(\omega,\cdot\,)$.

# Appendix B

# Dipole transformations

Here we prove two basic relations which are crucial for the dipole picture representation of inclusive and diffractive $\gamma^* p$ cross sections. We start from

$$\left\{\frac{\mathbf{k}}{D(\mathbf{k})}-\frac{\mathbf{k}+\mathbf{l}}{D(\mathbf{k}+\mathbf{l})}\right\}=\int\frac{d^2\mathbf{r}}{2\pi}\,e^{-i\mathbf{k}\cdot\mathbf{r}}\,\left(1-e^{-i\mathbf{r}\cdot\mathbf{l}}\right)\,i\,\frac{\mathbf{r}}{r}\,\overline{Q}\,K_1(\overline{Q}r), \tag{B.1}$$

where $K_1$ is the Bessel–Mc Donald function and $D(\mathbf{k})=\mathbf{k}^2+\overline{Q}^2$. In order to prove the above relation let us write the l.h.s of eq. (B.1) as

$$\int d^2\mathbf{k}_1\,\delta^2(\mathbf{k}_1-\mathbf{k})\left\{\frac{\mathbf{k}_1}{D(\mathbf{k}_1)}-\frac{\mathbf{k}_1+\mathbf{l}}{D(\mathbf{k}_1+\mathbf{l})}\right\}=$$

$$=\int d^2\mathbf{k}_1\int\frac{d^2\mathbf{r}_1}{(2\pi)^2}\,e^{i\mathbf{r}\cdot(\mathbf{k}_1-\mathbf{k})}\,\left\{\frac{\mathbf{k}_1}{D(\mathbf{k}_1)}-\frac{\mathbf{k}_1+\mathbf{l}}{D(\mathbf{k}_1+\mathbf{l})}\right\}=$$

$$=\int\frac{d^2\mathbf{r}}{2\pi}\,e^{-i\mathbf{r}\cdot\mathbf{k}}\int\frac{d^2\mathbf{k}_1}{2\pi}\,e^{i\mathbf{r}\cdot\mathbf{k}_1}\,\left\{\frac{\mathbf{k}_1}{D(\mathbf{k}_1)}-\frac{\mathbf{k}_1+\mathbf{l}}{D(\mathbf{k}_1+\mathbf{l})}\right\}.$$

The r.h.s of eq. (B.1) is found after integration over $\mathbf{k}_1$ with the help of the relation

$$\int\frac{d^2\mathbf{k}}{2\pi}\,\exp\{i\mathbf{k}\cdot\mathbf{r}\}\,\frac{\mathbf{k}}{D(\mathbf{k})}=i\,\overline{Q}\,\frac{\mathbf{r}}{r}\,K_1(\overline{Q}r). \tag{B.2}$$

In the same way we can prove the second basic formula

$$\left\{\frac{1}{D(\mathbf{k})}-\frac{1}{D(\mathbf{k}+\mathbf{l})}\right\}=\int\frac{d^2\mathbf{r}}{2\pi}\,e^{-i\mathbf{k}\cdot\mathbf{r}}\,\left(1-e^{-i\mathbf{r}\cdot\mathbf{l}}\right)\,K_0(\overline{Q}r), \tag{B.3}$$

where the relation analogous to (B.2) looks as follows

$$\int\frac{d^2\mathbf{k}}{2\pi}\,\exp\{i\mathbf{k}\cdot\mathbf{r}\}\,\frac{1}{D(\mathbf{k})}=K_0(\overline{Q}r)\,. \tag{B.4}$$

with $K_0$ being the Bessel–Mc Donald function.

Eq. (B.2) can be obtained from eq. (B.4) as a result of differentiation with respect to $\mathbf{r}$ and the relation $K_0'(x) = -K_1(x)$. Therefore, we only need to prove relation (B.4).

This can easily be done by performing the angular integration on the l.h.s of eq. (B.4) with the help of the well known relation

$$\exp\{ikr\cos\phi\} \;=\; J_0(kr) + 2\sum_{n=1}^{\infty} i^n J_n(kr)\cos n\phi \;, \tag{B.5}$$

where $J_n$ are the Bessel functions. Thus, we find

$$\int \frac{d^2\mathbf{k}}{2\pi}\, e^{i\mathbf{k}\cdot\mathbf{r}}\, \frac{1}{D(\mathbf{k})} \;=\; \int_0^{\infty} \frac{k\; dk}{k^2+\overline{Q}^2} \int_0^{2\pi} \frac{d\phi}{2\pi}\; \exp\{ikr\cos\phi\} \;=$$

$$= \int_0^{\infty} \frac{k\; dk}{k^2+\overline{Q}^2} \int_0^{2\pi} \frac{d\phi}{2\pi}\; \left\{ J_0(kr) + 2\sum_{n=1}^{\infty} i^n J_n(kr)\cos n\phi \right\} \;=$$

$$= \int_0^{\infty} dk\; \frac{k\; J_0(kr)}{k^2+\overline{Q}^2} \;\equiv K_0(\overline{Q}r)\,.$$

# Bibliography


[1] J. D. Bjorken, *Phys. Rev.* **179** (1969) 1547.

[2] R. P. Feynman, *Phys. Rev. Lett.* **23** (1969) 1415.

[3] R. P. Feynman, *Photon Hadron Interactions*, W. A. Benjamin, New York, 1972.

[4] J. D. Bjorken and E. A. Paschos, *Phys. Rev.* **185** (1969) 1975.

[5] H. Fritsch, M. Gell-Mann and H. Leutwyler, *Phys. Lett.* **47B** (1973) 365.

[6] D. J. Gross and F. Wilczek, *Phys. Rev. Lett.* **30** (1973) 1343.
H. D. Politzer, *Phys. Rev. Lett.* **30** (1973) 1346.

[7] H. Georgi and H. D. Politzer, *Phys. Rev.* **D9** (1974) 416;
D. J. Gross and F. Wilczek, *Phys. Rev.* **D9** (1974) 980.

[8] T. Muta, *Foundation of Quantum Chromodynamics*, World Scientific, Singapore,1987.

[9] K. Wilson, *Phys. Rev.* **179** (1969) 1499; *ibidem.* **D3** (1971) 1818.

[10] N. Christ, B. Hasslacher and A. H. Mueller, *Phys. Rev.* **D6** (1972) 3543.

[11] R. K. Ellis, W. Furmanski and R. Petronzio, *Nucl. Phys.* **B212** (1983) 29;
A. B. Bukhvostov, G. V. Frolov, L. N. Lipatov and E. A. Kuraev, *Nucl. Phys.* **B258** (1985) 601;
J. Bartels and C. Bontus, *Phys. Rev.* **D61** (2000) 034009.

[12] G. Altarelli and G. Parisi, *Nucl. Phys.* **B126** (1977) 298;
G. Altarelli, *Phys. Rep.* **81** (1982) 1.

[13] V. N. Gribov and L. N. Lipatov, *Sov. J. Nucl. Phys.* **15** (1972) 438.

[14] Yu. L. Dokshitzer, *Sov. Phys. JETP* **46** (1977) 641.

[15] Yu. L. Dokshitzer, D. I. Dyakonov and S. I. Troyan, *Phys. Rep.* **58** (1980) 270.

[16] G. Curci, W. Furmański and R. Petronzio, *Nucl. Phys.* **B175** (1980) 27;
W. Furmański and R. Petronzio, *Phys. Lett.* **B97** (1980) 437; *Z. Phys.* **C11** (1982) 293.

[17] *Perturbative Quantum Chromodynamics*, ed. A. H. Mueller, World Scientific, Singapore, 1989.

[18] A. H. Mueller, *Phys. Lett.* **B396** (1997) 251.

[19] P. D. B. Collins, An Introduction to Reggge Theory and High Energy Physics, Cambridge University Press, Cambridge, 1977.

[20] J. R. Forshaw and D. A. Ross, *Quantum Chromodynamics and the Pomeron*, Cambridge University Press, Cambridge, England, 1996.

[21] A. Donnachie and P. V. Landshoff, *Nucl. Phys.* **B 231** (1984) 189.

[22] A. Donnachie and P. V. Landshoff, *Phys. Lett.* **B 296** (1992) 227.

[23] F. Close, *Acta Phys. Polon.* **B31** (2000) 2557.

[24] M. Froissart, *Phys. Rev.* **123** (1961) 1053;
A. Martin, *Phys. Rev.* **129** (1963) 1432.

[25] L. N. Lipatov, *Sov. J. Nucl. Phys.* **23** (1976) 338;
E. A. Kuraev, L. N. Lipatov and V. S. Fadin, *Sov. Phys. JETP* **44** (1976) 443;
E. A. Kuraev, L. N. Lipatov and V. S. Fadin, *Sov. Phys. JETP* **45** (1977) 199;
Ya. Ya. Balitsky and L. N. Lipatov, *Sov. J. Nucl. Phys.* **28** (1978) 338.

[26] Ya. Ya. Balitsky, L. N. Lipatov and V. S. Fadin, in *Proc. of Leningrad Winter School, Physics of Elementary Particles*, Leningrad 1979, 109-149.

[27] V. Del Duca, *preprint* DESY-95-023, DFTT-13-95, Feb 1995, `hep-ph/9503226`.

[28] K. Golec-Biernat, L. Motyka and A. Staśto, *in preparation.*

[29] V. Fadin, *BFKL news*, Talk given at LISHEP 98, Rio de Janeiro, Brazil, 16-20 Feb 1998, *e*-print `hep-ph/9807528`.

[30] V. Fadin and L. N. Lipatov, *Phys. Lett.* **429** (1998) 127.

[31] G. P. Salam, *Acta Phys. Polon.* **30** (1999) 3679.

[32] J. Bartels, S. Gieseke and C.-F. Qiao, *Phys. Rev.* **D63** (2001) 056014.

[33] S. Catani, M. Ciafaloni and F. Hautmann, *Phys. Lett.* **B242** (1990) 97;
*Nucl. Phys.* **B366** (1991) 657;
J. C. Collins and R. K. Ellis, *Nucl. Phys.* **B360** (1991) 3;
E. M. Levin, M. G. Ryskin, Yu. M. Shabel'sky and A. Shuvaev, *Sov. J. Nucl. Phys.* **53** (1991) 657.

[34] S. Catani and F. Hautmann, *Nucl. Phys.* **B427** (1994) 475;
M. Ciafaloni, *Phys. Lett.* **B356** (1995) 74.

[35] J. Kwieciński and A. D. Martin, *Phys. Lett.* **B353** (1995) 123.

[36] A. H. Mueller, *Nucl. Phys.* **B415** (1994) 373; *Nucl. Phys.* **B437** (1995) 107;
A. H. Mueller and B. Patel, *Nucl. Phys.* **B425** (1994) 471;
Z. Chen and A. H. Mueller, *Nucl. Phys.* **B451** (1995) 579.

[37] N. N. Nikolaev and B. G. Zakharov, *Z. Phys.* **C 64** (1994) 651; *JETP* **78** (1994) 598;
N. N. Nikolaev, B. G. Zakharov and V. R. Zoller, *JETP Lett.* **60** (1994) 694; *Phys. Lett.* **B328** (1994) 486.

[38] A. Białas and R. Peschanski, *Phys. Lett.* **B355** (1995) 301.

[39] L. V. Gribov, E. M. Levin and M. G. Ryskin, *Nucl. Phys.* **B188** (1981) 555; *Phys. Rep.* **100** (1983) 1.

[40] A. H. Mueller and Jian-wei Qiu, *Nucl. Phys.* **B268** (1986) 427.

[41] J. Kwieciński, *Z. Phys.* **29** (1985) 147.

[42] J. C. Collins and J. Kwieciński, *Nucl. Phys.* **B335** (1990) 89.

[43] J. Kwieciński, A. D. Martin and R. G. Roberts, W. J. Stirling, *Phys. Rev.* **D42** (1990) 3645;
J. Kwieciński, A. D. Martin and P. J. Sutton, *Phys. Rev.* **D44** (1991) 2640.

[44] J. Bartels, G. A. Schuler and J. Blümlein, *Z. Phys.* **C50** (1991) 91; *Nucl. Phys. Proc. Suppl.* **18 C** (1991) 147.

[45] J. Bartels and E. M. Levin, *Nucl. Phys.* **B387** (1992) 617.

[46] E. M. Levin, M. G. Ryskin and A. G. Shuvaev, *Nucl.Phys.* **B387** (1992) 589.

[47] M. Altmann, M.Glück and E. Reya, *Phys. Lett.* **B285** (1992) 359.

[48] J. Bartels and M. G. Ryskin, *Z. Phys.* **C62** (1994) 425.

[49] K. Golec-Biernat, M. W. Krasny and S. Riess, *Phys. Lett.* **B337** (1994) 367.

[50] J. Bartels, *Nucl. Phys* **B151** (1979) 293; *Nucl. Phys* **B175** (1980) 365; preprint DESY 91-074 (unpublished).

[51] J. Kwieciński and M. Praszałowicz, *Phys. Lett* (1980) **B94** (1980) 413.

[52] J. Bartels, *Phys. Lett.* **B298** (1993) 204; *Z. Phys.* **C60** (1993) 471; *Z. Phys.* **C62** (1994) 425;
J. Bartels and M. Wüsthoff, *Z. Phys.* **C66** (1995) 157.

[53] J. Bartels and C. Ewerz, *JHEP* **9909** (1999) 026.

[54] L. N. Lipatov,*Nucl. Phys.* **B365** (1991) 614; *Nucl. Phys.* **B452** (1995) 369, *Phys. Rep.* **286** (1997) 131;
R. Kirschner, L. N. Lipatov and L. Szymanowski, *Nucl. Phys.* **B425** (1994) 579, *Nucl. Phys. D51* (1995) 838.

[55] A. H. Mueller, *Nucl. Phys.* **B335** (1990) 115.

[56] A. H. Mueller and B. Patel, *Nucl. Phys.* **B425** (1994) 471;
Yu. A. Kovchegov, A. H. Mueller and S. Wallon, *Nucl. Phys.* **B507** (1997) 367;
A. H. Mueller, *Eur. Phys. J.* **A1** (1998) 19; *Nucl.Phys.* **A654** (1999) 37c; *Nucl.Phys.* **B558** (1999) 285.

[57] G. P. Salam, *Nucl. Phys.* **B449** (1995) 589; *Nucl. Phys.* **B461** (1996) 512; *Comput. Phys. Commun.* **105** (1997) 62;
A. H. Mueller and G. P. Salam, *Nucl. Phys.* **B475** (1996) 293.

[58] R. Peschanski, *Phys. Lett.* **B409** (1997) 492;
H. Navelet and R. Peschanski, *Phys. Rev. Lett.* **82** (1999) 1370;
A. Białas, H. Navelet and R. Peschanski, *Phys. Lett.* **B427** (1998) 147; *Phys. Rev.* **D57** (1998) 6585;
R. Janik and R. Peschanski, *Nucl. Phys.* **B549** 280.

[59] E. Gotsman, E. M. Levin and U. Maor, *Nucl. Phys.* **B464** (1996) 251; *Nucl. Phys.* **B493** (1997) 354; *Phys. Lett.* **B245** (1998) 369; *Eur. Phys. J.* **C5** (1998) 303;
E. Gotsman, E. M. Levin, U. Maor and E. Naftali, *Nucl. Phys.* **B539** (1999) 535;
A. L. Ayala Filho, M. B. Gay Ducati and E. M. Levin, *Eur. Phys. J.* **C8** (1999) 115;
E. M. Levin and U. Maor, `hep-ph/0009217`.

[60] J. Jalilian-Marian, A. Kovner, L. McLerran and H. Weigert, *Phys. Rev.* **D55** (1997) 5414;
J. Jalilian-Marian, A. Kovner and H. Weigert, *Phys. Rev.* **D59** (1999) 014015;
J. Jalilian-Marian, A. Kovner, A. Leonidov and H. Weigert, *Nucl.Phys.* **B504** (1997) 415; *Phys. Rev.* **D59** (1999) 014014; *Phys. Rev.* **D59** (1999) 034007; Erratum *ibid.* **D59** (1999) 099903.

[61] Ya.Ya. Balitsky, *Nucl.Phys.* **B463** (1996) 99; *Phys. Rev. Lett.* **81** (1998) 2024; *Phys. Rev.* **D60** (1999) 014020; `hep-ph/0101042`.

[62] A. Kovner, J.Guilherme Milhano and H. Weigert, *Phys. Rev.* **D62** (2000) 114005;
H. Weigert, NORDITA-2000-34-HE, `hep-ph/0004044`.

[63] L. McLerran and R. Venugopalan, *Phys. Rev.* **D49** (1994) 2233, *Phys. Rev.* **D49** (1994) 3352, *Phys. Rev.* **D50** (1994) 2225;
A. Kovner, L. McLerran and H. Weigert, *Phys.Rev.* **D52** (1995) 6231,

*Phys. Rev.* **D52** (1995) 3809;
R. Venugopalan, *Acta. Phys. Polon.* **B30** (1999) 3731;
E. Iancu, A. Leonidov and L. McLerran, `hep-ph/0011241`.

[64] E. Iancu and L. McLerran, `hep-ph/0103032`.

[65] A. De Rujula, S. L. Glashow, H. D. Politzer, S. B. Treiman, F. Wilczek and A. Zee, *Phys. Rev.* **D10** (1974) 1649.

[66] Yu. V. Kovchegov, *Phys. Rev.* **D60** (1999) 034008; *Phys. Rev.* **D61** (2000) 074018.

[67] Yu. V. Kovchegov and L. McLerran, *Phys. Rev.* **D60** (1999) 054025; Erratum-ibid. **D62** (2000) 019901;
Yu. V. Kovchegov and E. M. Levin, *Nucl. Phys.* **B577** (2000) 221;

[68] E. M. Levin and K. Tuchin, *Nucl. Phys.* **B537** (2000) 833;
M. A. Braun, *Eur. Phys. J.* **C16** (2000) 337.

[69] H. Abramowicz and A. Caldwell, *Rev. Mod. Phys.* **71** (1999) 1275, `hep-ex/9903037`.

[70] H1 Collab., C. Adloff et al., *Eur. Phys. J.* **C21** (2001) 33;
ZEUS Collab., Chekanov S. et al., *Eur. Phys. J.* C (2001) DOI 10.1007/s100520100749.

[71] J. Kwieciński, A. D. Martin and P. J. Sutton, *Phys. Lett.* **B287** (1992) 254; *Phys.Rev.* **D53** (1996) 6094.
A. J. Askew, J. Kwieciński, A. D. Martin and P. J. Sutton, *Phys. Rev.* **D47** (1993) 3775; *Phys. Rev.* **D49** (1994) 4402;
A. J. Askew, K. Golec-Biernat, J. Kwieciński, A. D. Martin and P. J. Sutton, *Phys. Lett.* **B325** (1994) 212.

[72] J. Kwieciński, A. D. Martin and A. M. Staśto, *Phys. Rev.* **D56** (1997) 3991.

[73] M. Ciafaloni, *Nucl. Phys.* **B296** (1988) 49;
S. Catani, F. Fiorani and G. Marchesini, *Phys. Lett.* **B234** (1990) 339; *Nucl. Phys.*.**B336** (1990) 18;
G. Marchesini, *Nucl. Phys.* **B445** (1995) 49.

[74] G. Marchesini and B. R. Webber, *Nucl. Phys.* **B386** (1992) 215;
J. Kwieciński, A. D. Martin, P. J. Sutton, *Phys. Rev.* **D52** (1995) 1445; *Phys. Rev.* **D53** (1996) 6094; *Z. Phys.* **D71** (1996) 585;
B. Andersson, G. Gustafson and J. Samuelsson, *Nucl. Phys.* **B463** (1996) 217 (1996);
B. Andersson, G. Gustafson, H. Kharraziha and J. Samuelsson, *Z. Phys.* **C71**(1996) 613;
K. Golec-Biernat, L. Goerlich, J. Turnau, *Nucl.Phys.* **B527** (1998) 289;
H. Kharraziha and L. Lonnblad; *JHEP* **9803** (1998) 006;
G. Bottazzi, G. Marchesini, G. P. Salam and M. Scorletti, *Nucl. Phys.*

**B505** (1997) 366;
G. P. Salam, *JHEP* **9903**(1999) 009;
H. Jung, *Nucl.Phys.Proc.Suppl.* **79** (1999) 429; `hep-ph/9908497`;
H. Jung and G. P. Salam, `hep-ph/0012143`;
M. A. Kimber, J. Kwieciński, A. D. Martin and A. M. Staśto, *Phys. Rev.* **D62** (2000) 094006.

[75] R. D. Ball and S. Forte, *Phys. Lett.* **B335** (1994) 77; *ibidem.* **B335** (1994) 77.

[76] S. Catani and F. Hautmann, *Nucl. Phys.* **B427** (1994) 475;
R. K. Ellis, Z. Kunst and E. M. Levin, *Nucl. Phys.* **B420** (1994) 517; *erratum-ibidem.* bf B433 (1995) 498
R. K. Ellis, F. Hautmann and B. R. Webber, *Phys. Lett.* **B348** (1995) 582;
R. D. Ball and S. Forte, *Phys. Lett.* **B348** (1995) 313;
J. Kwieciński and A. D. Martin, *Phys. Lett.* **B353** (1995) 123;
J. R. Forshaw, R. G. Roberts and R. S. Thorn, *Phys. Lett.* **B356** (1995) 79.

[77] A. H. Mueller, *Nucl. Phys.* **B18C** (1991) 125; *J. Phys.* **G17** (1991) 1443;
W. K. Tang, *Phys. Lett* **B278** (1992) 363.
J. Bartels, A. de Roeck and M. Loewe, *Z. Phys.* **C54** (1992) 635;
J. Kwieciński, A. D. Martin and P. J. Sutton, *Phys. Rev.* bf D46 (1992) 921; *Phys. Lett.* **B287** (1992) 254;
J. Bartels and H. Lotter, *Phys.Lett.* **B309** (1993) 400;
J. Kwieciński, C. A .M. Lewis and A. D. Martin, *Phys. Rev.* **D54** (1996) 6664;
J. Bartels *et al.*, *Phys. Lett.* **B384** (1996) 300;
J. Bartels, V. Del Duca and M. Wusthoff, *Z. Phys.* **C76** (1997) 75;
P. Mirkes and D. Zeppenfeld, *Phys. Rev* **B78** (1997) 428;
J. Kwieciński, S. C. Lang and A. D. Martin, *Eur. Phys. J.* **C6** (1999) 671;
J. Kwieciński, A. D. Martin and J. J. Outhwaite, *Eur. Phys. J.* **C9** (1999) 611.

[78] H1 Collab., S. Aid et al., *Phys. Lett.* **B356** (1995) 118.

[79] H1 Collab., C. Adloff et al., *Nucl. Phys.* **B538** (1999) 3; *Phys. Lett.* **B462** (1999) 440;
ZEUS Collab., J.Breitweg et al., *Euro. Phys. J. C6* (1999) 239.; *Phys. Lett.* **B474** (2000) 223.

[80] A. H. Mueller and H. Navalet, *Nucl. Phys.* **B282** (1987) 727.

[81] V. Del Duca and C. R. Schmidt, *Phys. Rev.* **D49** (1994) 4510; *ibidem.* **D51** (1995) 2150;
W. J. Stirling, *Nucl. Phys.* **B423** (1994) 4510;
L. H. Orr and W. J. Stirling, **D56** (1997) 5875;
J. R. Andersen et al. `hep-ph/0101180`;
J. Kwieciński, A. D. Martin, L. Motyka and J. J. Outhwaite, `hep-ph/0105039`.

[82] A. J. Askew, D. Graudenz, J. Kwieciński and A. D. Martin, **Phys. Lett. B338**, (1994) 92;
J. R. Forshaw and R. G. Roberts, *Phys. Lett.* **B335** (1994) 494;
J. Kwieciński, A. D. Martin and A. M. Staśto, *Phys. Lett.* **B459** (1999) 644.

[83] ZEUS Collab., J. Breitweg et al. *Phys. Lett.* **B481** (2000) 199.

[84] K. Golec-Biernat, J. Kwieciński, A. D. Martin and P. J. Sutton, *Phys. Lett.* **B335** (1994) 220; *Phys. Rev.* **D50** (1994) 217-225.

[85] H1 Collab., C. Adloff et al., *Nucl. Phys.* **B485** (1997) 3; *Eur.Phys.J.* **C12** (2000) 595.

[86] H1 Collaboration, C. Adloff *et al.*, *Z. Phys.* **C76** (1997) 613.

[87] ZEUS Collaboration, M. Derrick *et al.*, *Eur. Phys. J.* **C6** (1999) 43.

[88] J. Bartels, H. Lotter, M. Vogt, *Phys. Lett.* **B373** (1996) 215.

[89] J. R. Forshaw and M. G. Ryskin, *Z. Phys.* **C68** (1995) 137;
J. Bartels, J. R. Forshaw, H. Lotter and M. Wüsthoff, *Phys. Lett.* **B375** (1996) 301.

[90] N. N. Nikolaev and B. G. Zakharov, *Z. Phys.* **C49** (1991) 607; *Z. Phys* **C 53** (1992) 331.

[91] W. Buchmüler, A. Hebecker and T. Gehrmann, *Nucl. Phys.* **B537** (1999) 477.

[92] J. D. Bjorken, J. B. Kogut and D. E. Soper, *Phys. Rev.* **D3** (1970) 1382.

[93] B. L. Ioffe, *Phys. Lett.* **B30** (1969) 123.

[94] K. Golec–Biernat and M. Wüsthoff, *Phys. Rev.* **D59** (1999) 014017.

[95] K. Golec–Biernat and M. Wüsthoff, *Phys. Rev.* **D60** (1999) 114023.

[96] W. Buchmüller, T. Gehrmann and A. Hebecker *Nucl. Phys.* **B537** (1999) 477;
J. R. Forshaw, G. Kerley and G. Shaw, *Phys. Rev* **D60** (1999) 074012, *Nucl. Phys.* **A675** (2000) 80;
E. Gotsman, E. M. Levin, U. Maor and E. Naftali, *Eur. Phys. J.* **C10** (1999) 689;
M. McDermott, L. Frankfurt, V. Guzey and M. Strikman, *Eur. Phys. J.* **C16** (2000) 641;
T. G. Cvetic, D. Schildknecht and A. Shoshi, *Acta Phys. Polon.* **B 30** (1999) 3265;
A. Capella, E. G. Ferreiro, A. B. Kaidalov and C. A. Salgado, *Nucl. Phys.* **B593** (2001) 336; *Phys. Rev.* **D63** (2001) 054010

[97] J. D. Bjorken and J. B. Kogut, *Phys. Rev.* **D8** (1973) 1341.

[98] A. M. Staśto, K. Golec-Biernat and J. Kwieciński, *Phys. Rev. Lett.*, **86** (2001) 596.

[99] J. Bartels, K. Golec–Biernat and K. Peters, *Eur. Phys. J.* **C17** (2000) 121.

[100] A. D. Martin, R. G. Roberts, W. J. Stirling and R. S. Thorne, *Phys. Lett.* **B443** (1998) 301.

[101] L. Frankfurt, A. Radyushkin and M. Strikman, *Phys. Rev.* **D55** (1997) 98.

[102] J. Bartels, K. Golec–Biernat and H. Kowalski, *in preparation.*

[103] A. Donnachie and P. V. Landshoff, *Phys. Lett.* **B437** (1998) 408, *ibidem.* **B470** (1999) 243.

[104] B. Badełek and J. Kwieciński, *Phys. Lett.* **B295** (1992) 263.

[105] J. J. Sakurai, *Ann. Phys. (NY)* **11** (1960) 1;
T. H. Bauer, R. D. Spital, D. R. Yennie and F. M. Pipkin, *Rev. Mod. Phys.* **50** (1978) 261.

[106] A. D. Martin, M. G. Ryskin and A. M. Staśto *Eur. Phys. J.* **C7** (1999) 643.

[107] B. Badełek and J. Kwieciński, *Rev. Mod. Phys.* **68** (1996) 445.

[108] W. Buchmüller and D. Heidt, `hep-ph/9605428`
D. Schildknecht and H. Spiesberger, `hep-ph/9707447`
M. Reuter, *Eur. Phys. J.* **C7** (1999) 233.

[109] A. M. Cooper-Sarkar, R. C. E. Devenish and A. De Roeck, *Int. J. Mod. Phys.* **A13** (1998) 3385.

[110] M. Wüsthoff and A. D. Martin, *J. Phys.* **G25** (1999) R309.

[111] A. Hebecker, *Phys. Rep.* **331** (2000) 1; *Acta Phys. Polon.* **B30** (1999) 3777.

[112] H. Abramowicz, in *Proc. of the 19th Intl. Symp. on Photon and Lepton Interactions at High Energy LP99* ed. J.A. Jaros and M.E. Peskin, eConf**C990809**, 495 (2000), `hep-ph/0001054`.

[113] G. Ingelman and P. Schlein, *Phys. Lett.* **B152** (1985) 256.

[114] K. Golec–Biernat, J. P. Phillips, *J. Phys.* **G22** (1996) 921.

[115] K. Golec–Biernat, *Acta Phys. Polon.* **B27** (1996) 134.

[116] C. Royon *et al.*, `hep-ph/0010015`.

[117] K. Golec–Biernat and J. Kwieciński, *Phys. Lett.* **B353** (1995) 329.

[118] T. Gehrmann and W. J. Stirling, *Z. Phys.* C70 (1996) 89.

[119] A. Capella *et al.*, *Phys. Rev.* **D53** (1996) 2309.

[120] K. Golec–Biernat and J. Kwieciński, *Phys. Rev.* **D55** (1997) 3209.

[121] K. Golec–Biernat, J. Kwieciński and A. Szczurek, *Phys. Rev.* **D56** (1997) 3955.

[122] K. Golec–Biernat, J. Kwieciński and A. Szczurek, Proceedings of Madrid Workshop on Low x Physics, Madrid, Spain, 18-21 June 1997, ed. by F. Bareiro, L. Labarga, and J. del Peso, World Scientific (1998) 284.

[123] N. N. Nikolaev and B. G. Zakharov, *Z. Phys.* **C53** (1992) 331.

[124] J. Bartels, C. Ewerz, H. Lotter and M. Wüsthoff, *Phys. Lett.* **B386** (1996) 389.

[125] J. Bartels, H. Lotter and M. Wüsthoff, *Phys. Lett.* **B379** (1996) 239, Erratum-*ibid.* **B382** (1996)449.

[126] W. Buchmüller and A. Hebecker, *Nucl. Phys.* **B476** (1996) 203.

[127] E. M. Levin and M. Wüsthoff, *Phys. Rev.* **D50** (1994) 4306;
M. Wüsthoff, *Phys. Rev.* **D56** (1997) 4311.

[128] J. Bartels, J. Ellis, H. Kowalski and M. Wüsthoff, *Eur. Phys. J.* **C7** (1999) 443.

[129] J. Bartels, H. Jung and M. Wüsthoff, *Eur. Phys. J.* **C11** (1999) 111.

[130] W. Buchmüller, M. McDermott and A. Hebecker, *Nucl. Phys.* **B487** (1997) 283, Erratum-*ibid.* **B500** (1997) 621;
A. Hebecker, *Nucl. Phys.* **B505** (1997) 349;
W. Buchmuller, T. Gehrmann and A. Hebecker, *Nucl. Phys.* **B537** (1999) 477.

[131] M. G. Ryskin, *Sov. J. Nucl. Phys.* **52** (1990) 529.

[132] J. Bartels and M. Wüsthoff, *J. Phys.* **G22** (1996) 929.

[133] F. Hautmann, Z. Kunszt and D. E. Soper, *Phys. Rev. Lett.* **81** (1998) 3333; *Nucl. Phys. Proc. Suppl.* **79** (1999) 260.

[134] J. Bartels and M. Wüsthoff, *Z. Phys.* **C66** (1995) 157.

[135] M. Genovese, N. N Nikolaev and B. G.Zakharov, JETP **81** (1995) 625;
A. Białas and R. Peschanski, *Phys. Lett.* **B378** (1996) 302; *ibid.* **B387** (1996) 405;
A. Białas *Acta Phys. Polon.* **B28** (1997) 1239;
A. Białas and W. Czyż, *Acta Phys.Polon.* **B29** (1998) 2095;
S. Munier, R. Peschanski and C. Royon, *Nucl. Phys.* **B534** (1998) 297.

[136] A. Donnachie and P. V. Landshoff, *Phys. Lett.* **B191** (1987) 309; **B198** (1987) 590 (Erratum).

[137] A. Donnachie and P. V. Landshoff, *Nucl. Phys.* **B244** (1984) 322; **B267** (1986) 690.

[138] E. L. Berger *et al.*, *Nucl. Phys.* **B286** (1987) 704.

[139] A. Capella *et al.*, *Phys. Lett.* **B343** (1995) 403.

[140] F. Abe *et al.*, *Phys. Rev.* **D50** (1994) 5535.

[141] A. D. Martin, R. G. Roberts and W. J. Stirling, *Phys. Lett.* **B356** (1995) 89.

[142] R. D. Field and G. C. Fox, *Nucl. Phys.* **80** (1974) 367.

[143] K. Golec–Biernat, J. Kwieciński and A. D. Martin, *Phys. Rev.* **D58** (1998) 094001.

[144] K. Golec–Biernat and A. D. Martin, *Phys. Rev.* **D59** (1999) 014029.

[145] A. G. Shuvaev, K. Golec–Biernat, A. D. Martin and M.G. Ryskin, *Phys. Rev.* **D60** (1999) 014015.

[146] K. Golec–Biernat, A. D. Martin and M. G. Ryskin, *Phys. Lett.* **B456** (1999) 232-239.

[147] M. L. Good and W. D. Walker, *Phys. Rev.* **160** (1960) 1857.

[148] H. Miettinen and J. Pumplin, *Phys. Rev.* **D18** (1978) 1696.

[149] A. Berera and D. E. Soper, *Phys. Rev.* **D50** (1994) 4328.

[150] L. Trentadue and G. Veneziano, *Phys. Lett.* **323** (1994) 201.

[151] J. C. Collins, *et al.*, *Phys. Rev.* **D51** (1995) 3182.

[152] Z. Kunszt and W. J. Stirling, `hep-ph/9609245`;
A. Berera and D. E. Sopper, *Phys. Rev.* **D53** (1996) 6162.

[153] J. C. Collins, *Phys. Rev.* **D57** (1998) 3051.

[154] J. C. Collins, L. Frankfurt and M. Strikman *Phys. Lett.* **B307** (1993) 161.

[155] K. Golec–Biernat and M. Wüsthoff, *Eur. Phys. J.* **C20** (2001) 313.

[156] K. Golec–Biernat, J. Kwieciński and A. M. Staśto, *in preparation.*

## Acknowledgments

I would like to thank Professor Jan Kwieciński who introduced me into the subject of the small-$x$ physics and who enthusiastically supported me at every moment of my scientific career. His guidance and expertise made this thesis possible.

I owe much to my collaborators. I am particularly grateful to Mark Wüsthoff for smooth and enjoyable collaboration. My understanding of the subject has been greatly developed through joint work with Adrian Askew, Jochen Bartels, Lidia Goerlich, Henri Kowalski, Witek Krasny, Jan Kwieciński, Alan Martin, Stefan Riess, Misha Ryskin, Krisztian Peters, Julian Phillips, Andriej Shuvaev, Anna Staśto, Peter Sutton, Antoni Szczurek and Jacek Turnau.

I am very grateful to Professors Alan Martin and Jochen Bartels for their help during my stay at the universities in Durham and Hamburg.

Many warm thanks to the members of the Kraków H1 Collaboration group for their hospitality during the years of my contacts with H1 Collaboration as a guest and as a member. Special thanks to Ewelina Łobodzińska for her wise support.

I thank my colleagues from the Department of Theoretical Physics of the Institute of Nuclear Physics in Kraków for stimulating and friendly atmosphere. I also thank my colleagues from Physics Departments of the University of Durham and the University of Hamburg for enjoyable atmosphere.

I warmly thank my brother Janusz for careful reading of the manuscript, and Jochen Bartels and Jan Kwieciński for useful comments.

I am especially grateful to my parents, my wife Alina and children Łukasz and Artur for their love.

This research has been supported by the Polish State Committee for Scientific Research (KBN) under Grant No. 5 P03B 144 20, and by the EU Fourth Framework Program "Training and Mobility of Researches" Network "Quantum Chromodynamics and the Deep Structure of Elementary Particles" contract FMRX-CT98-0194 (DG 12-MIHT). The Royal Society and Deutsche Forschungsgemeinschaft fellowships are gratefully acknowledged.